AD NUMBER

ADB184875

NEW LIMITATION CHANGE

TO

Approved for public release, distribution unlimited

FROM

Distribution authorized to U.S. Gov't. agencies and their contractors; Administrative/Operational Use; 07 MAR 1951. Other requests shall be referred to National Aeronautics and Space Administration, Washington, DC 20546.

AUTHORITY

NASA TR Server Website

AD-B184 875

N-5761

NATI●NAL ADVIS●RY C●MMITTEE FOR AER●NAUTICS

NACA C●NFERENCE ●N AIRCRAFT STRUCTURES

A C●MPILATI●N ●F THE PAPERS PRESENTE●

Langley Aeronautical Laboratory

Langley Field, Va. CLASSIFICATION CHANGED

March 7, 1951 To _Unclassified_

By authority of *TPA #* Date

45

NACA

94-14778

92

UNCLASSIFIED

NACA CONFERENCE ON AIRCRAFT

STRUCTURES

A Compilation of the Papers Presented
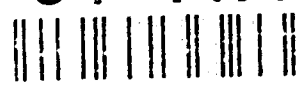
Langley Aeronautical Laboratory
Langley Field, Va.

March 7, 1951

CONFIDENTIAL

TABLE OF CONTENTS

DTIC QUALITY INSPECTED 3

CONFIDENTIAL

INTRODUCTION

This document contains reproductions of technical papers on some
of the most recent research results on aircraft structures from the
NACA Laboratories. These papers were presented by members of the
staff of the NACA Laboratories at the NACA conference held at the
Langley Aeronautical Laboratory March 7, 1951. The purpose of this
conference was to convey to those involved in the study of aircraft
structures these recent research results and to provide those attending
an opportunity for discussion of the results.

The papers in this document are in the same form in which they
were presented at the conference so that distribution of them might
be prompt. The original presentation and this record are considered
as complementary to, rather than as substitutes for, the Committee's
system of complete and formal reports.

A list of the conferees is included.

v

LIST OF CONFEREES

The following were registered at the NACA Conference on Aircraft Structures, Langley Aeronautical Laboratory, Langley Field, Va., March 7, 1951:

Abzug, Malcolm J.	Sperry Gyroscope Company, Great Neck, Long Island, N. Y.
Achterkirchen, K. H.	Lockheed Aircraft Corporation, Burbank, Calif.
Allen, Frederick C.	Douglas Aircraft Company, Inc., El Segundo, Calif.
Allison, John M.	Naval Ordnance Experimental Unit, Bureau of Standards, Washington, D. C.
Anderson, J. Edward	NACA - Langley Laboratory
Anderson, Roger A.	NACA - Langley Laboratory
Assicurato, Thomas	East Coast Aeronautics, Inc., Mt. Vernon, N. Y.
Bailey, F. J., Jr.	NACA - Langley Laboratory
Barrett, Paul F.	NACA - Langley Laboratory
Batdorf, S. B.	NACA - Langley Laboratory
Becht, J. H.	Naval Air Material Center, Philadelphia, Pa.
Beckett, Major Walter R.	Air Materiel Command Engineering Field Officer, Langley Air Force Base, Va.
Berdahl, Edgar O.	Headquarters, Strategic Air Command, Offutt Air Force Base, Omaha, Nebr.
Boden, O. W.	Aerophysics Laboratory, North American Aviation, Inc., Los Angeles, Calif.
Boshar, John	Civil Aeronautics Administration, Washington, D. C.
Bouton, I.	McDonnell Aircraft Corporation, St Louis, Mo.
Brown, Harvey H.	NACA Headquarters
Bryan, G. L.	Department of Aeronautics, Johns Hopkins University, Baltimore, Md.
Budiansky, Bernard	NACA - Langley Laboratory
Burr, Captain Paul J.	Office of Naval Research, Washington, D. C.
Buterbaugh, Floyd F.	U. S. Naval Air Development Center, Johnsville, Pa.

Carlson, R. M.	Headquarters, Air Materiel Command, Wright-Patterson Air Force Base, Dayton, Ohio
Cathaway, Russ G.	Lockheed Aircraft Corporation, Burbank, Calif.
Church, A. S.	Douglas Aircraft Company, Inc., Long Beach, Calif.
Clauser, Milton U.	Purdue University, Lafayette, Ind.
Daughaday, H.	Cornell Aeronautical Laboratory, Inc., Buffalo, N. Y.
Daum, Fred L.	Headquarters, Air Materiel Command, Wright-Patterson Air Force Base, Dayton, Ohio
Devine, Robert L., Jr.	Project Meteor, Massachusetts Institute of Technology, Cambridge, Mass.
Diehl, Captain Walter S.	Bureau of Aeronautics, Navy Department, Washington, D. C.
Dix, E. H., Jr.	Aluminum Company of America, New Kensington, Pa.
Donely, Philip	NACA - Langley Laboratory
Donlan, C. J.	NACA - Langley Laboratory
Dow, Norris F.	NACA - Langley Laboratory
Draley, E. C.	NACA - Langley Laboratory
Duberg, John E.	NACA - Langley Laboratory
Epstein, Albert	Republic Aviation Corporation, Farmingdale, Long Island, N. Y.
Farrell, John W.	Aircraft Laboratory, Engineering Division, Air Materiel Command, Wright-Patterson Air Force Base, Dayton, Ohio
Fearnow, Dwight O.	NACA - Langley Laboratory
Fedziuk, Henry A.	NACA - Langley Laboratory
Fennema, Frederick F.	Headquarters, Strategic Air Command, Offutt Air Force Base, Omaha, Nebr.
Fettis, Henry E.	Headquarters, Air Materiel Command, Wright-Patterson Air Force Base, Dayton, Ohio
Frankland, J. M.	Chance Vought Aircraft, Dallas, Tex.

Garrick, I. E.	NACA - Langley Laboratory
Gatewood, Buford E.	Headquarters, Air Materiel Command, Wright-Patterson Air Force Base, Dayton, Ohio
Gilson, Robert D.	Fairchild Aircraft, Hagerstown, Md.
Goranson, R. F.	NACA Headquarters
Gossard, Myron L.	NACA - Langley Laboratory
Green, G. G.	Consolidated Vultee Aircraft Corporation, San Diego, Calif.
Griffith, George E.	NACA - Langley Laboratory
Grover, Horace J.	Battelle Memorial Institute, Columbus, Ohio
Gunsolus, Ann E.	Sperry Gyroscope Company, Great Neck, Long Island, N. Y.
Hardrath, Herbert F.	NACA - Langley Laboratory
Harrington, J. H.	Headquarters, Air Materiel Command, Wright-Patterson Air Force Base, Dayton, Ohio
Harris, T. A.	NACA - Langley Laboratory
Hedrick, Ira G.	Grumman Aircraft Engineering Corporation, Bethpage, Long Island, N. Y.
Heimerl, George J.	NACA - Langley Laboratory
Heldenfels, Richard R.	NACA - Langley Laboratory
Hoffman, Lt. Col. Robert W.	Headquarters, Air Materiel Command, Wright-Patterson Air Force Base, Dayton, Ohio
Hoge, H. J.	North American Aviation, Inc., Los Angeles, Calif.
Honts, A. B.	General Electric Company, Aviation Division, Schenectady, N. Y.
Hood, Manley J.	NACA - Ames Laboratory
Hoover, C. S.	Naval Air Material Center, Philadelphia, Pa.
Houbolt, John C.	NACA - Langley Laboratory
Hubbard, Harvey H.	NACA - Langley Laboratory
Hyler, W. S.	Battelle Memorial Institute, Columbus, Ohio
Jagiello, L. T.	U. S. Naval Ordnance Test Station, Inyokern, China Lake, Calif.
James, H. D.	Northrop Aircraft, Inc., Hawthorne, Calif.

ix

Jewett, F. D.	The Glenn L. Martin Company, Baltimore, Md.
Johnson, Aldie E., Jr.	NACA - Langley Laboratory
Johnson, John E.	Consolidated Vultee Aircraft Corporation, Ft. Worth, Tex.
Kahn, Robert F.	United Aircraft Corporation, East Hartford, Conn.
Kartveli, A.	Republic Aviation Corporation, Farmingdale, Long Island, N. Y.
Kearns, John P.	Applied Physics Laboratory, Johns Hopkins University, Silver Spring, Md.
Kleckner, Harold F.	Douglas Aircraft Company, Inc., Santa Monica, Calif.
Kordes, Eldon E.	NACA - Langley Laboratory
Kuhn, Paul	NACA - Langley Laboratory
Kupelian, V. A.	Naval Ordnance Experimental Unit, Bureau of Standards, Washington, D. C.
Lang, Arthur L., Jr.	Project Meteor, Massachusetts Institute of Technology, Cambridge, Mass.
Lassiter, Leslie W.	NACA - Langley Laboratory
Latham, Captain Donald R.	Air Materiel Command Engineering Field Officer, Moffett Field, Calif.
Levy, Samuel	National Bureau of Standards, Washington, D. C.
Libove, Charles	NACA - Langley Laboratory
Liebowitz, Harold	Office of Naval Research, Washington, D. C.
Loch, Joseph	Headquarters, Air Materiel Command, Wright-Patterson Air Force Base, Dayton, Ohio
Lueck, David W.	Headquarters, Air Materiel Command, Wright-Patterson Air Force Base, Dayton, Ohio
Lundquist, E. E.	NACA - Langley Laboratory
Lutz, R. J.	The RAND Corporation, Santa Monica, Calif.
Mangurian, George N.	Northrop Aircraft, Inc., Hawthorne, Calif.

x

McBrearty, J. F.	Lockheed Aircraft Corporation, Burbank, Calif.
Mearns, W. C.	International Nickel Company, New York, N. Y.
Mellquist, V. G.	Aircraft Industries Association, Washington, D. C.
McVay, Francis	Republic Aviation Corporation, Farmingdale, Long Island, N. Y.
Meyer, John H.	McDonnell Aircraft Corporation, St. Louis, Mo.
Miller, W. H.	Bureau of Aeronautics, Navy Department, Washington, D. C.
Molella, R. J.	Naval Air Material Center, Philadelphia, Pa.
Muse, T. C.	Research and Development Board, Washington, D. C.
Nelson, Thomas	Carswell Air Force Base, Ft. Worth, Tex.
Osborn, Earl P.	Grumman Aircraft Engineering Corporation, Bethpage, Long Island, N. Y.
O'Sullivan, William J., Jr.	NACA - Langley Laboratory
Ottmar, J.	General Plate Company, Attleboro, Mass.
Palmer, Carl B.	NACA Headquarters
Parker, Commander J. F.	Bureau of Aeronautics, Navy Department, Washington, D. C.
Pearson, Henry A.	NACA - Langley Laboratory
Pederson, Jerard M.	General Electric Company, Aircraft Gas Turbine Division, Lynn, Mass.
Phillips, F. W.	NACA Headquarters
Pian, T. H. H.	Massachusetts Institute of Technology, Cambridge, Mass.
Pride, Richard A.	NACA - Langley Laboratory
Propper, Edward M.	Consolidated Vultee Aircraft Corporation, Ft. Worth, Tex.
Pusin, H.	The Glenn L. Martin Company, Baltimore, Md.
Ray, George D.	Bell Aircraft Company, Buffalo, N. Y.
Reissner, Eric	Massachusetts Institute of Technology, Cambridge, Mass.

Rhode, Richard V.	NACA Headquarters
Roberts, William M.	NACA - Langley Laboratory
Roche, J. A.	Air Materiel Command Engineering Field Office, Langley Air Force Base, Va.
Rosche, Melvin G.	NACA Headquarters
Rosenbaum, Robert	Civil Aeronautics Administration, Washington, D. C.
Ruhnke, D. H.	Republic Steel Corporation, Massilon, Ohio
Schleicher, Richard L.	North American Aviation, Inc., Los Angeles, Calif.
Schnitt, Arthur	Bell Aircraft Corporation, Buffalo, N. Y.
Schwartz, R. T.	Headquarters, Air Materiel Command, Wright-Patterson Air Force Base, Dayton, Ohio
Sechler, E. E.	California Institute of Technology, Pasadena, Calif.
Seide, Paul	NACA - Langley Laboratory
Shapiro, Oscar	U. S. Naval Air Development Center, Johnsville, Pa.
Shempp, William M.	NEPA Division, Fairchild Engineering & Airplane Corporation, Oak Ridge, Tenn.
Shinn, D. A.	Headquarters, Air Materiel Command, Wright-Patterson Air Force Base, Dayton, Ohio
Shortal, Joseph A.	NACA - Langley Laboratory
Shuler, William T.	Civil Aeronautics Administration, Washington, D. C.
Sibila, A. I.	Chance Vought Aircraft, Dallas, Tex.
Slomski, Joseph	NACA - Lewis Laboratory
Smith, Henry G., Jr.	Hughes Aircraft Company, Culver City, Calif.
Smith, Howard W.	Boeing Airplane Company, Seattle, Wash.
Smith, Randall C.	East Coast Aeronautics, Inc., Mt. Vernon, N. Y.
Snyder, George	Boeing Airplane Company, Seattle, Wash.
Soulé, Hartley A.	NACA - Langley Laboratory
Spiess, Paul C.	Civil Aeronautics Administration, Washington, D. C.
Stein, Manuel	NACA - Langley Laboratory

Stevens, J. E.	Chance Vought Aircraft, Dallas, Tex.
Stone, Mel	Douglas Aircraft Company, Inc., Long Beach, Calif.
Stowell, Elbridge Z.	NACA - Langley Laboratory
Strang, Charles R.	Douglas Aircraft Company, Inc., Santa Monica, Calif.
Swanson, Warren E.	North American Aviation, Inc., Los Angeles, Calif.
Tatnall, Francis G.	Baldwin-Lima-Hamilton Corporation, Philadelphia, Pa.
Taylor, F. C.	Carswell Air Force Base, Ft. Worth, Tex.
Templin, R. L.	Aluminum Company of America, New Kensington, Pa.
Thompson, Floyd L.	NACA - Langley Laboratory
Thornton, Kirby F.	Aluminum Company of America, New Kensington, Pa.
Tobey, Harry	Piasecki Helicopter Corporation, Morton, Pa.
Trimarchi, V. C.	General Electric Company, Schenectady, N. Y.
Underwood, William J.	NACA Liaison Officer at the Air Materiel Command, Wright-Patterson Air Force Base, Dayton, Ohio
Van Every, K. E.	Douglas Aircraft Company, Inc., El Segundo, Calif.
Vollmecke, A. A.	Civil Aeronautics Administration, Washington, D. C.
Walsh, J. E.	Bureau of Aeronautics, Navy Department, Washington, D. C.
Weeks, L. M.	McDonnell Aircraft Corporation, St. Louis, Mo.
Wehle, L. B., Jr.	Grumman Aircraft Engineering Corporation, Bethpage, Long Island, N. Y.
Weisman, Y.	Consolidated Vultee Aircraft Corporation, San Diego, Calif.
Welch, H. C.	David Taylor Model Basin, Navy Department, Washington, D. C.

Williams, Walter C.   NACA High-Speed Flight Research Station
Wood, Clotaire   NACA Headquarters
Woods, R. J.   Bell Aircraft Corporation,
                                Buffalo, N. Y.
Woolard, Henry W.   Cornell Aeronautical Laboratory, Inc.,
                                Buffalo, N. Y.
Worley, G. F.   Douglas Aircraft Company, Inc.,
                                Santa Monica, Calif.

Yagiela, Stanley   Civil Aeronautics Administration,
                                Washington, D. C.

Zender, George W.   NACA - Langley Laboratory
Zimmerman, Charles H.   NACA - Langley Laboratory

DYNAMICS

SOME CONSIDERATIONS OF WING-FLEXIBILITY EFFECTS

ON RESPONSE DUE TO GUSTS

By Eldon E. Kordes and John C. Houbolt

Langley Aeronautical Laboratory

There is continued concern as to the role that structural flexibility plays in airplane reaction due to gusts and in gust measurements. This paper is intended to give an evaluation of the importance of wing bending flexibility.

Analyses that attempt to deal thoroughly with all the structural flexibilities are rather involved and are not well suited for evaluation studies which require the calculation of a great many individual cases. Therefore, as a basic stepping point, the problem was idealized somewhat as follows. Airplane motion was assumed to be represented by two degrees of freedom: vertical motion of the airplane and fundamental wing bending. Two-dimensional unsteady-lift theory was used and it was assumed that the idealized airplane encounters prescribed gust variations in the direction of flight. The thought behind representing airplane motion by two degrees of freedom was to see whether a method suitable for making trend studies could be found and to see if some basic parameters related to flexibility effects could be established.

A classical treatment of the idealized system led to response equations which suggested certain natural parameters and these are shown in figure 1. The purpose of this figure is to show the nature of the parameters since they denote conditions for dynamic similarity; airplanes having similar values of these parameters would have similar responses (that is, have similar values for gust-response factor as well as for certain other nondimensional quantities relating to the effects of the gust on the airplane). The first parameter μ_0 is associated with vertical motion of the airplane. It is very similar to the relative density or so-called mass parameter that has been referred to in other gust studies. In this expression W is the gross weight of the airplane, π is the value of one-half the theoretical lift-curve slope, ρ is air density, g is the acceleration of gravity, c_0 is a reference chord, and S is wing area. Because wing bending is included, a similar parameter μ_1 is also found and might be considered as the mass parameter associated with the fundamental mode. The only difference between this parameter and μ_0 is that W is replaced by W_1, where W_1 is defined by the integral shown, which involves the spanwise weight distribution w and the fundamental-mode curve y_1 normalized to unit tip deflection. The next parameter is λ which is given in terms of

the natural frequency of the fundamental mode, the reference chord, and
the forward velocity of the airplane. This parameter is very similar
to the reduced frequency parameter used in flutter. The fourth param-
eter H represents the distance in chords from the beginning of an
assumed single gust to its peak vertical-velocity value. The next param-
eter $\dfrac{x_m}{x_c}$ is associated with the bending moment due to lift and with the
alleviation moment associated with mass inertia effects, x_c is the
distance from the center line of the airplane to the center of lift, and
x_m is the distance from the center line to the center of gravity of the
semispan mass.

It may be of interest to see how the two-degree-of-freedom analysis
which led to these parameters agrees with a more complete analysis
method.

In figure 2 the bending stress developed near the root of a partic-
ular twin-engine transport airplane flying into a 10-foot-per-second
sharp-edge gust is shown. The results obtained by a recurrence-matrix
method which involves the use of influence coefficients at six semispan
stations (reference 1) and the two-degree-of-freedom analysis agree
rather well over the time interval shown, which includes the maximum
stress developed. These results lend a measure of confidence in the use
of the simplified analysis for making trend studies.

In the evaluation of flexibility effects a possible approach would
be to investigate what effect individual variations in the basic param-
eters would have on airplane response. This approach has the objection,
however, that the physical significance may not at once be evident.
Therefore, it may be more instructive to consider what happens when
operating conditions for a typical airplane are varied, such as a change
in speed or a change in mass distribution, even though a change in one
operating condition may cause a change in several of the parameters.
Thus the present evaluation is made by considering four specific oper-
ating effects and these are listed in figure 3. The first effect deals
with gust gradient distance. The second phase deals with gust shape and
for the present investigation three types have been considered; they are
a sine gust, a sine squared gust (which may also be called a
1 - cos gust), and a triangular gust. The present investigation is
limited to single gusts, but it is recognized that gust sequence or pene-
tration of successive gusts may be important. The third effect involves
the static loading conditions. The case of a twin-engine airplane with
fuel tanks outboard of the engines is chosen and three loading conditions
are considered. The first is that with a full load in the fuselage and
wing fuel tanks nearly empty. The second loading condition is with half
fuselage load and about half fuel load, and the third loading condition

is that with fuselage nearly empty and with tanks full. The total air-
plane weight for each of these three conditions is approximately the same
so that the effect of load distribution could be studied. The fourth
effect considered might be called a speed effect; it deals with changing
the speed of the airplane and is not meant here as a compressibility
effect. In making use of the parameters shown in figure 1 the
product λH can be formulated, which can be shown to be equal to $\frac{\pi}{4}$

times the period ratio $\frac{T_G}{T_1}$, where T_G is the time required to reach

maximum gust velocity and T_1 is one-fourth the natural period of the
fundamental mode.

This ratio is formulated because an analogous period ratio has
been found to be very significant in response calculations of elastic
structures under impulsive loadings. The ratio may be changed by
changing λ, which is a function of V, or by changing H. This speed
effect may thus be indicated to some extent by phase 1 indicated in
figure 3, which deals with H, but to obtain a direct measure of speed
itself, all conditions are held fixed and only speed is varied.

To evaluate the effects outlined in figure 3, case history studies
were made on a twin-engine airplane having a gross weight of about
40,000 pounds. The speed used was approximately 250 miles per hour,
unless otherwise noted.

Consider the effect of phase 1 - that of varying gust gradient dis-
tance. Figure 4 shows the results of encountering gusts of varying gust
gradient distances, where the gust was considered to be of the sine
type. The upper portion of this figure shows the variation of a bending-
moment parameter C_M with H. This nondimensional bending-moment
parameter can be used to calculate the net incremental moment developed
due to the gust from the equation shown in the figure, where k is
readily calculated from the lift-curve slope, air density, wing area, and
distance to center of lift, V is forward velocity, and U is peak gust
velocity, and of course C_M is picked from the curve. Values are shown
of C_M that would be obtained if the airplane were considered rigid and
if the airplane were considered flexible. Thus, the difference in the
two curves may be considered as a dynamic overshoot effect. The ratio
of the ordinates of the curves would lead to a response-factor curve
which is shown in the lower portion of the figure. It can be seen that
for gradient distances of about 4 the dynamic overshoot is approximately
20 to 25 percent, and for gust gradient distances of about 10 or greater
the overshoot is only about 1 percent or less. The results indicate
that for the larger gradient distances the particular airplane considered
acts essentially as a rigid body and that dynamic overshoot is only

important in this range of distance. These points will be discussed in more detail subsequently.

The influence that gust shape has on response factor is shown in figure 5. In general the trend is very similar for the three gust shapes considered and the response factor is very nearly 1 in all cases for H of 10 or greater. These results are for the second loading condition shown in figure 3, but similar agreement would be found for the other two conditions. From this it can be seen that the effect of gust shape is not quite as critical as has sometimes been supposed, at least for single gusts. Since shape does not appear to be critical, the sine gust was arbitrarily chosen for subsequent calculations.

The next phase considers the effect of loading conditions on airplane response. The variation of the response factor with gust gradient distance for the three loading conditions considered is shown in figure 6. It should be noticed that as the load is removed from the center of the airplane and is increased in the outboard portion, the effect is to increase the response factor over a wider range of gradient distance. Thus, the effect of increased spanwise mass is to increase the dynamic response effect. Considering the response factor alone, however, may be misleading, as can be seen by considering the lower half of the chart where C_M is plotted against H for each of the three loading conditions. These curves are of primary interest to the designer since they lead to the net incremental bending moment that would be developed. The condition of full fuselage load leads to the largest value of C_M and, hence, bending moment, and there is an appreciable reduction in C_M as the load goes outboard on the span. Thus, the loading conditions where load is concentrated near the center line is the critical one, as would be expected. The fact that the response factor is high for the outboard loading condition is, from the design standpoint, not important in this case.

It is of interest to consider the stresses that might be expected to occur during flight. To do this it is worthwhile to review some of the results that have been obtained by the Langley Gust Loads Branch from airplanes in thunderstorm operation. In figure 7 is shown a shot-gun pattern of the variation of peak gust velocity with gust gradient distance (see reference 2), where H is given in feet instead of chords. These data were gathered from analysis of time-history records and were deduced by assuming that the gusts encountered were of a triangular nature. Assume that it is desired to calculate the maximum stresses that would be developed by the gusts indicated here. The curved line from the origin to U = 50 feet per second represents essentially the envelope curve of the data up to a gradient distance of about 90 feet, and a nearly horizontal line is assumed to apply thereafter. If given gradient distances are considered, gusts which lead to maximum stresses

would naturally be those having the greatest vertical velocity, or those which fall along the envelope curve. To determine the stresses produced by the gusts represented by the envelope curve, the first loading condition of the example airplane was chosen since it leads to the critical bending moment. The bending stress that develops near the root of the wing as it varies with gust gradient distance is shown in figure 8. The gradient distance is given here in both feet and chord units. The results for the elastic airplane and the airplane assumed rigid are shown, and these results tend to show rather clearly the effect of dynamic response. A rather interesting effect can be noticed as gust gradient distance approaches 10 chords, which is in the neighborhood of the nominal value considered in design. In this region maximum stresses are reached but dynamic overshoot is very small. It might be concluded that, for this example, a rigid-body analysis would be quite adequate for design purposes.

It would be instructive to find out how increased speeds might affect this conclusion. That is, consider the gust which led to the maximum stresses shown in figure 8 and vary the speed so that the period ratio T_G/T_1 becomes the same as the period ratio that is found in the region of the figure where H is between 3 and 6 chords and dynamic overshoot is large. The first loading condition was used and the airplane flown with increasing speeds through sine gusts of 10-chord gradient distance. The results are shown in figure 9 where the dynamic response factor at two altitudes is plotted as a function of both velocity and period ratio T_G/T_1. Considering first the response factor at sea-level, it is seen that it is very nearly one over the entire velocity range considered. It was noted earlier that when the period ratio is varied by varying H alone, the response factor might change by as much as 25 percent. Thus the period ratio in gust treatment is much more complex than in the case of elastic structures under impulsive loading. The reason is that a change in forward speed not only changes the period ratio but changes the aerodynamic damping characteristics as well.

The results presented for an altitude of 25,000 feet show an increase in the response factor over the velocity range considered. Here again, considering the response factor alone may be misleading; the incremental bending moment at 400 miles per hour and 25,000 feet would actually be about 0.6 of the bending moment at sea level for the same velocity.

The final results presented are for the effect of flexibility on accelerations. Some acceleration measurements have been made on a Martin 202 airplane in flight through rough air (reference 3) and it was of interest to see whether the results obtained could be predicted by theoretical response calculations. To make the calculations, the

gusts shown in figure 7 were again considered. The results are shown in figure 10 where the acceleration developed at the airplane center line is plotted against the acceleration at the nodal points of the fundamental mode, this latter being used as a measure of average airplane acceleration.

According to theoretical calculations all gusts falling in the region where H is between 25 and 90 feet (see fig. 7) would establish a band formed by the curve and the $45°$ line shown in figure 10. The data obtained in flight are shown by the plotted points in the lower portion and it may be noticed that when considered as a group the flight data merge rather well into the band established theoretically.

To summarize, a simplified two-degree-of-freedom analysis has been applied to a twin-engine transport airplane in order to examine the effect of wing flexibility on gust response. Conditions varied were gust gradient distance, gust shape, static load distribution, and forward velocity. In the course of the investigation, parameters felt to be of general significance for gust response were established. Although the calculations were made for a particular airplane, the trends established should be similar for other airplanes of the same general class. Further study must be made of the effect of penetration of successive gusts, spanwise gust variation, compressibility, and probability of gust occurrence. Also, it is planned that the same general approach will be used to investigate aircraft of other classes.

REFERENCES

1. Houbolt, John C.: A Recurrence Matrix Solution for the Dynamic Response of Aircraft in Gusts. NACA TN 2060, 1950.

2. Donely, Philip: Summary of Information Relating to Gust Loads on Airplanes. NACA Rep. 997, 1950. (Formerly, NACA TN 1976, 1949.)

3. Shufflebarger, C. C., and Mickleboro, Harry C.: Flight Investigation of the Effect of Transient Wing Response on Measured Accelerations of a Modern Transport Airplane in Rough Air. NACA TN 2150, 1950.

$$\mu_0 = \frac{4W}{\pi \rho g c_0 S}$$

$$\mu_1 = \frac{4W_1}{\pi \rho g c_0 S}$$

$$W_1 = \int_0^L w y_1^2 \, dx$$

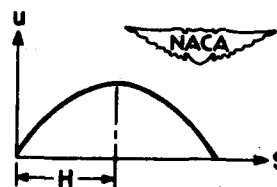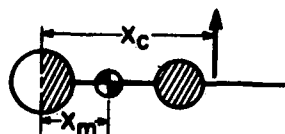$$\lambda = \frac{\omega_1 c_0}{2V}$$

$$H$$

$$\frac{x_m}{x_c}$$

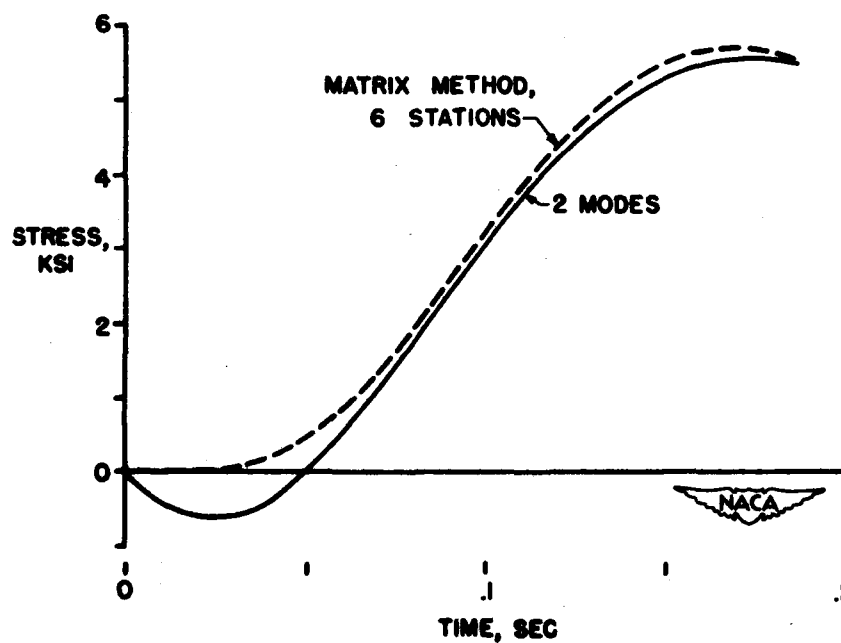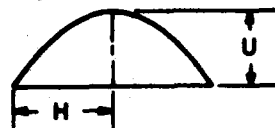Figure 1.- Basic parameters for airplane response to gusts resulting from two-degree-of-freedom analysis.

Figure 2.- Comparison of two-degree-of-freedom and recurrence-matrix solutions for response to 10-foot-per-second sharp-edge gusts.

1. GUST GRADIENT DISTANCE:

2. GUST SHAPE:

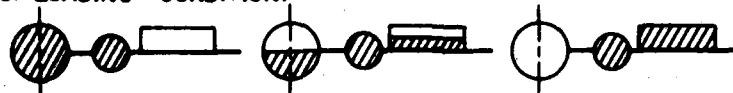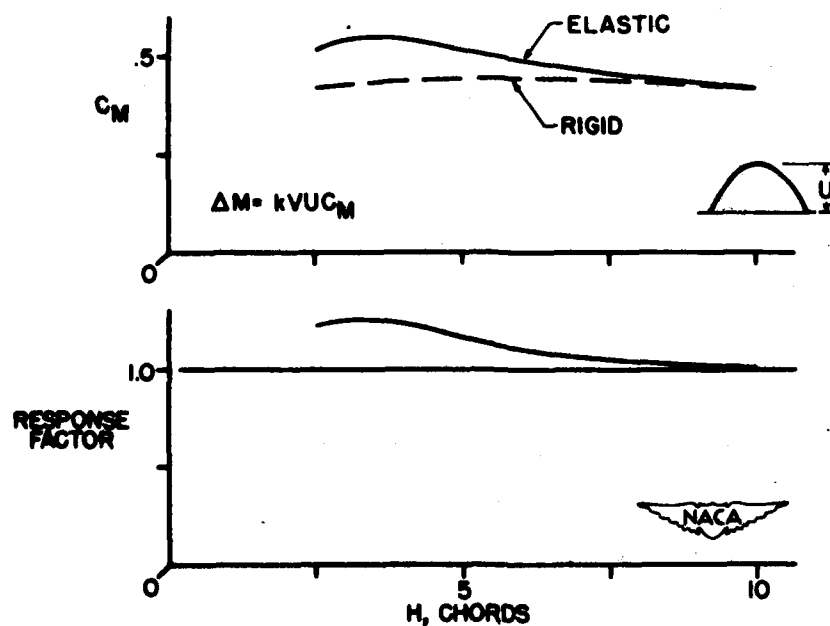SINE   (SINE)^2 TRIANGULAR

3. LOADING CONDITION:

4. SPEED EFFECT:

$$\lambda H = \frac{\omega_1 c_0}{2V} H = \frac{\pi}{4} \frac{T_G}{T_1}$$

NACA

Figure 3.- Operating condition varied for the analysis.

ELASTIC

.5

C_M

$\Delta M = kVUC_M$

RIGID

U

0

1.0

RESPONSE FACTOR

NACA

0   5   10

H, CHORDS

Figure 4.- Bending-moment parameter C_M and response factor
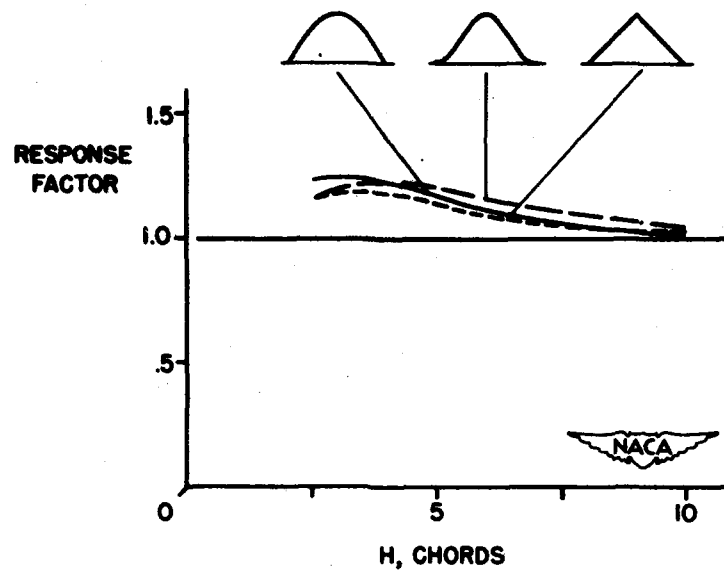as a function of gust gradient distance.

Figure 5.- Response factor for three gust shapes as a function
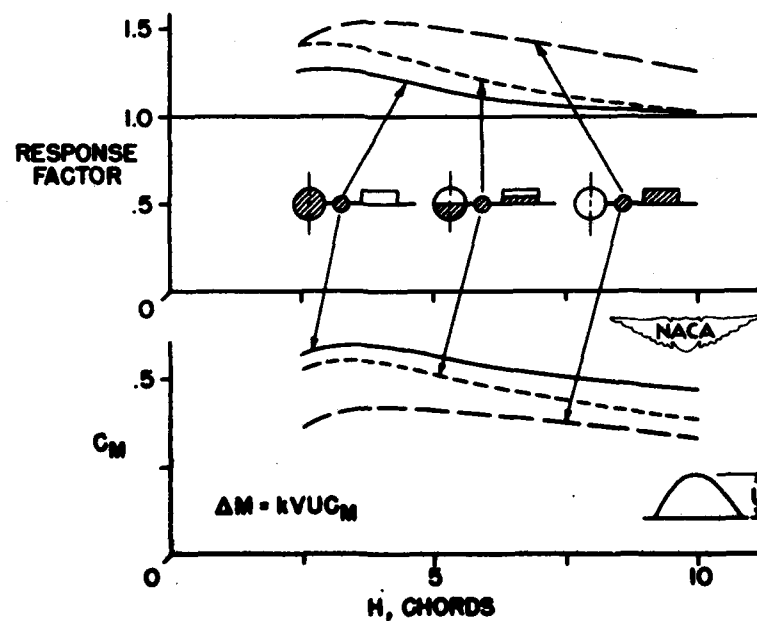of gust gradient distance.

Figure 6.- Response factor and bending-moment parameter C_M for
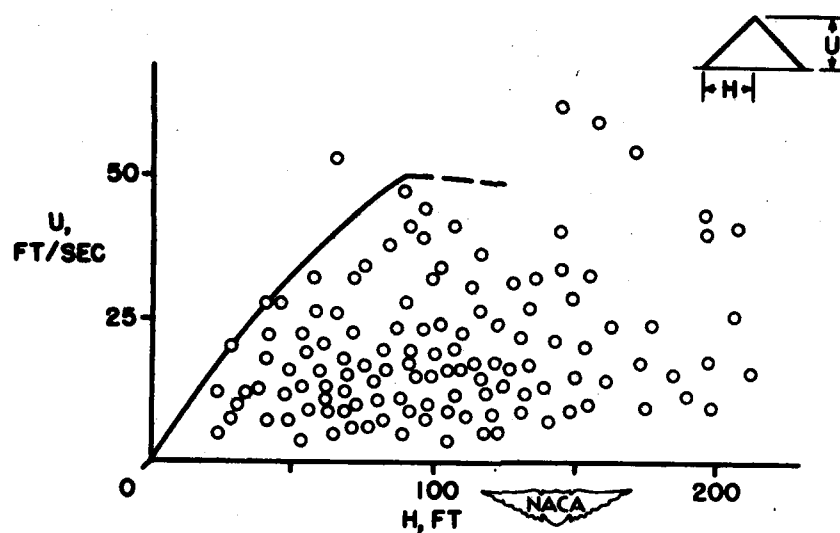three loading conditions as a function of gust gradient distance.

Figure 7.- Gust velocity as a function of gust gradient distance.
(See reference 2.)
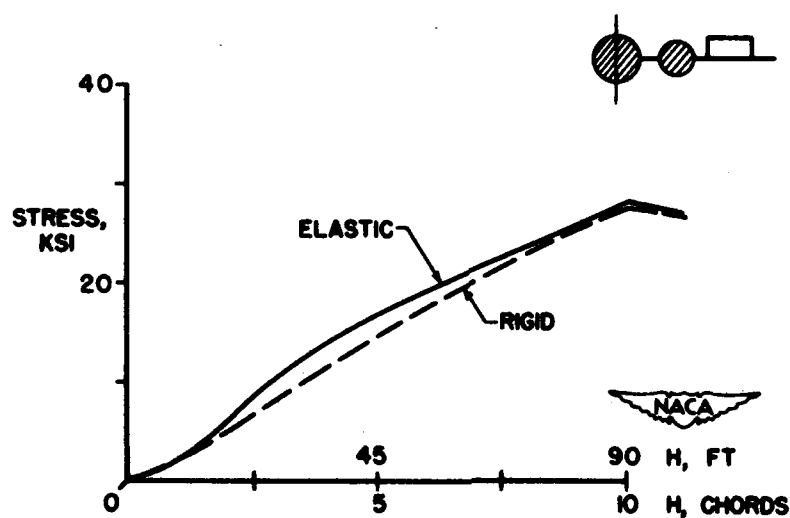

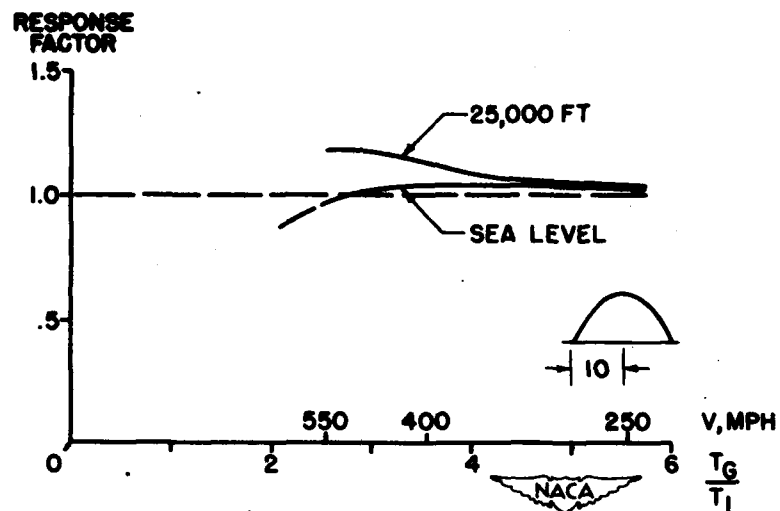Figure 8.- Maximum stress as a function of gust gradient distance.

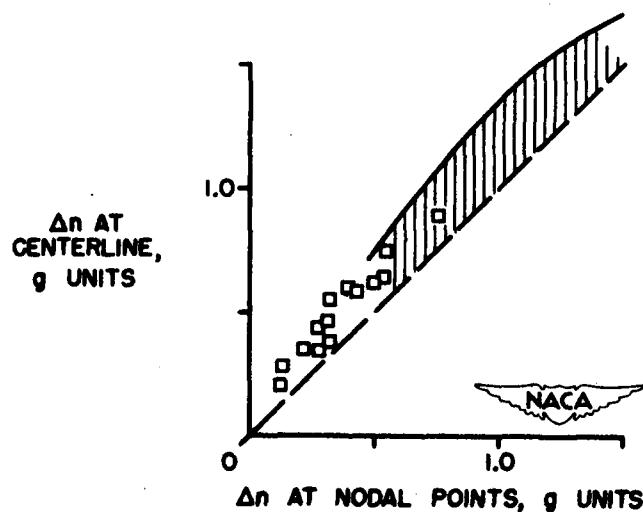Figure 9.- Response factor as a function of velocity and period ratio T_G/T_1.

Figure 10.- Acceleration at center of gravity as a function of nodal-point acceleration.

OSCILLATING PRESSURES ON FUSELAGES AND

WINGS DUE TO PROPELLERS

By Leslie W. Lassiter and Harvey H. Hubbard

Langley Aeronautical Laboratory

A rotating propeller is an intense source of oscillating pressures. At large distances from the propeller these pressures are recognized as merely unpleasant noise, but at points in the immediate vicinity of the propeller the oscillating pressures are of such magnitude that they are capable of exciting destructive vibrations in nearby parts of the airplane structure. Such vibrations are excited at the blade-passage frequency of the propeller or at some integral multiple of that frequency. The fatigue problem associated with vibrations of this nature is a serious one, since, with excitation frequencies of the order of 100 cycles per second, the structure is subjected to the stress cycle many times during a single flight. Fatigue of metal parts, then, is greatly accelerated.

Several instances of this type of vibration problem have been reported. There have been instances where panels failed in the fuselage wall near the propeller tip and, in some cases, wing panels in the vicinity of the propeller have also failed. The present paper is concerned with an evaluation of the oscillating pressures that occur in both phases of the problem. The discussion is concerned first with the fuselage wall problem, the nature of which is illustrated schematically in figure 1. The vibration amplitudes along the fuselage wall are shown in an exaggerated manner by the shaded panel blur. It is seen that the greatest amplitudes occur at about 1/4 radius ahead of and behind the plane of rotation.

It is, of course, desirable from the designer's standpoint that he be able to predict the magnitudes of the oscillating pressures so that he can calculate the vibration amplitudes and associated stresses in the structure. An experimental and theoretical investigation, therefore, was conducted to determine the significance of the various parameters involved in the problem. This investigation was primarily concerned with pressures in the region near the propeller tips and the type of data obtained is illustrated in figure 2. This figure presents a sample free-space pressure distribution (at zero forward speed) of the fundamental Fourier component of pressure near the propeller tip, as obtained along the line parallel to the axis of rotation at a distance of 1/6 radius from the tip. The root-mean-square values of the pressure are plotted in pounds per square foot as a function of distance in terms of propeller radii from the rotational plane. The maximum values occur

at distances of 1/4 radius ahead of and behind the propeller plane, and the largest pressures are contained in a region about 1 radius wide in the vicinity of the propeller plane.

For a propeller operating in free space, the pressure was found to be a function of propeller dimensions, torque, thrust, tip Mach number, and the point in space at which the measurement was made. The presence of a reflecting surface such as the fuselage causes the pressure at its surface to be increased above the free-space value at the same point. The amount of this increase is a function of the fuselage shape; a flat surface causes a doubling, whereas a curved surface increases the pressure by a lesser amount.

A theory which is useful in predicting these oscillating pressures at any point in space near the propeller was developed and is presented in reference 1. The agreement of the theory with experiment may be seen by comparison of the curves in figure 2. Good agreement was found for the lower harmonics up to a tip Mach number of 1.00 which was the limit of this series of tests.

In addition to the problem of propeller-excited vibrations in the fuselage wall, similar difficulties have been encountered in the wing structure of pusher configurations like that shown in figure 3. The shaded portion of the wing indicates the region where trouble occurred. In this area fatigue failures of the secondary structure of the wing, the wing panels, and the trailing-edge structure have been noted. They have been observed to occur not only in the region immediately ahead of the propeller, but also in the region beyond the propeller tip. Recently, the work on fuselage pressures near the tip of the blade has been extended to include the area ahead of the propeller where a wing might be located. In this latter investigation measurements were made along lines parallel to B-B in figure 3, in addition to the previous measurements along lines parallel to A-A. The experiments were conducted over a tip Mach number range extending to 1.20 and the data were correlated with theory at several different tip Mach numbers. The results of these tests are illustrated in figures 4 to 8.

Figure 4 presents the free-space root-mean-square pressure of the fundamental Fourier component as a function of distance from the propeller axis. Pressure units are pounds per square foot. These particular measurements were made along the line 1/4 radius ahead of the propeller at tip Mach numbers of 0.90 and 1.20. The maximum value of the fundamental Fourier component is seen to occur at the 0.5 station for both tip Mach numbers, but the magnitude at 1.20 is approximately twice that at a tip Mach number of 0.90.

Similar graphs of the distribution of harmonics higher than the first show a tendency for the maximum of the curve to move progressively

outward toward the blade tip. At about the sixth harmonic the maximum is found to occur even beyond the tip.

The dashed curve at the top of figure 4 is the distribution calculated by the theory for a tip Mach number of 1.20. It is seen that, even at this tip Mach number, the theory agrees reasonably well with the measured distribution. It should be pointed out that, for convenience in calculating these pressures, the torque and thrust forces acting on the blade are assumed to be concentrated at some effective radius.

The effective radius then is a function of the blade loading and the manner in which the forces at each blade element contribute to the free-space pressures at a point in space for a given harmonic. The value of the effective radius thus may differ for the various harmonics and for different blade loading.

For the fundamental frequency the effect of increasing distance from the propeller is beneficial in decreasing the free-space pressures. This attenuation effect is illustrated in figure 5. The curve on the right indicates the attenuation with distance from the tip in the z direction, whereas the attenuation with distance in the y direction is shown by the curve at the left. The pressure amplitudes of the fundamental component are thus seen to be attenuated rapidly as distance is increased. There is some evidence, however, to indicate that the effect of distance may be less beneficial in the case of the higher-order harmonics which have spatial distributions different from that of the fundamental Fourier component.

As was stated, the curves shown in figures 2 to 5 relate only to the fundamental component of pressure. It must be remembered that the total-pressure variation is generally composed of many of these Fourier components, all integral multiples of the blade-passage frequency. This is especially true near the blade tip because of the tendency for the higher harmonics to peak in that region; therefore, the total-pressure variation with time is not by any means a sinusoidal one. This variation is illustrated in figure 6, which shows a sample wave form of the total pressure in free space.

This wave form represents a time history of the pressure at a point in space during one revolution of a two-blade propeller. Each pair of peaks, positive and negative, corresponds to a blade passage. Positive pressure is measured upward from the reference line; negative pressure is downward. Although the particular wave form shown was obtained from a free-space measurement, its general shape applies also to wave forms observed at a reflecting surface. Neither the free-space nor surface-pressure wave forms are necessarily symmetrical about the reference pressure as this one is; in general they are not symmetrical.

When a wing is introduced into the oscillating pressure field, it is acted upon by the pressure in two ways. First, the phase and magnitude differences between pulses impinging on the top and bottom surfaces of a wing cause an alternating differential pressure to exist across the wing. Near the trailing edge, where the structure is relatively thin, this differential pressure tends to flex the structure. Figure 7 illustrates the variation of differential pressure across a thin wing as a function of distance from the propeller axis and gives a comparison with free-space peak-to-peak values at the same location. The wing surface used consisted of a thin flat board without camber. The values plotted in this figure are the peak-to-peak values of the total pressure obtained from wave forms similar to that of figure 6. It may be that the total pressure is not of as much importance as its individual components, but it is thought that discussion of the total pressure is justified by the large differences in magnitude and distribution existing between it and its components.

It is seen that the pressure differential across a thin wing is much greater than the free-space pressure at the same point. The two have similar spatial distributions, however, with the maximum pressure occurring in the region near the blade tip and slightly past the tip. It will be remembered that the fundamental component of pressure peaked at the 0.5 station; however, the higher harmonics, of which many are present, peak further out along the blade to give the resultant total differential pressure distribution shown in the figure. It is this differential pressure which may have been responsible for structural failures near the wing trailing edge, since it imposes oscillating loads which contribute to accelerated fatigue.

Another factor to be considered in conjunction with the wing structure is the pressure acting on each surface individually. It is this pressure which affects the wing panels and their associated members. There is a large difference in the magnitudes of these panel pressures for a given wing surface, depending upon whether the propeller blade approaches the surface or recedes from it. Figure 8 illustrates the variation of the surface pressure with distance along the wing for both top and bottom surfaces as the blade passes. The values plotted here are obtained from the positive and negative amplitudes of the total-pressure wave forms, as illustrated in figure 6. The curves at the top relate to the surface approached by the blade (in this illustration the top surface); those at the bottom of the chart relate to the opposite surface, from which the blade is receding. The peak pressures in both cases are plotted in units of pounds per square foot, compression or suction.

From the curves at the top, it is seen that where the surface is approached by the blade, the pressure variation with time is essentially symmetrical about the reference or atmospheric pressure. Wing panels on that surface, then, are subjected alternately to large compression and

suction loads. Both positive and negative magnitudes are greatest opposite the propeller tip, and they remain quite high even beyond the tip. It will be remembered that the trouble area indicated in figure 3 extended past the tip also. If the magnitudes on the surface from which the blade receded are compared with those on the opposite surface, it is seen that the surface approached by the blade is subjected to greater pressures and may be expected to prove most critical structurally. It is important to note that the direction of propeller rotation is significant since that determines which surface is subjected to greater pressures. Reversal of propeller rotation in the diagram of figure 8 would result in making the bottom surface most critical.

In summary: two phases of the propeller-excited vibration problem have been presented. One phase pertains to fuselage pressures in the region near the propeller tip; the other pertains to pressures on the wing structure near the propeller. It has been shown in this preliminary investigation that these oscillating pressures may be calculated and hence the order of magnitude of the problem can be defined.

REFERENCE

1. Hubbard, Harvey H., and Regier, Arthur A.: Free-Space Oscillating
    Pressures near the Tips of Rotating Propellers. NACA Rep. 996,
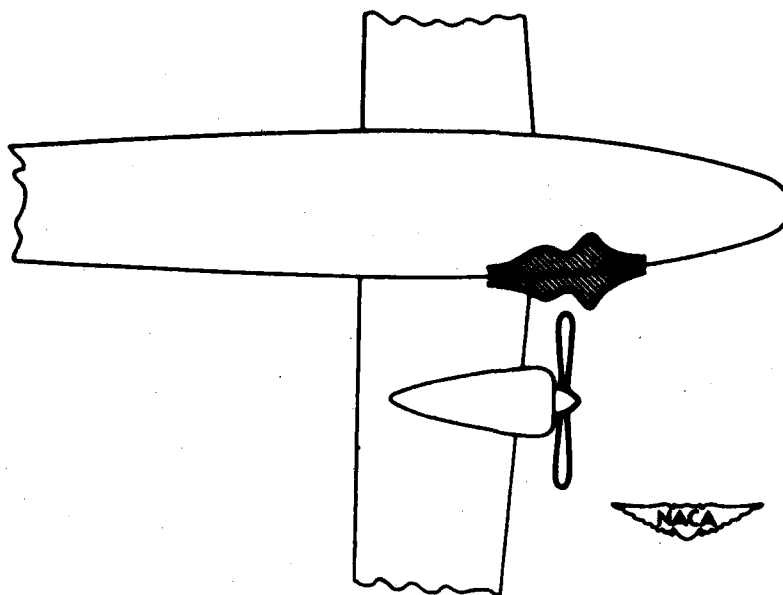   1950. (Formerly NACA TN 1870.)

Figure 1.- Nature of propeller-excited vibrations in a fuselage wall.
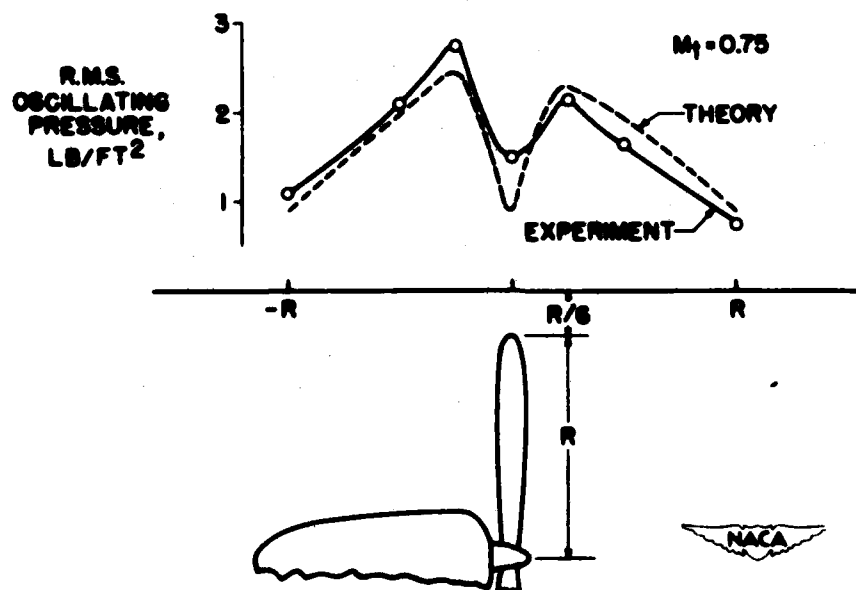

Figure 2.- Free-space pressure distribution of the fundamental Fourier component near the propeller tips.
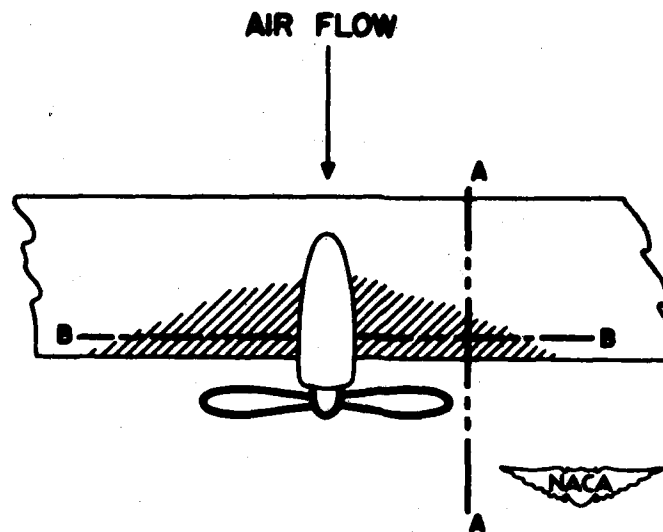
Figure 3.- Observed area of fatigue failures in pusher configurations.
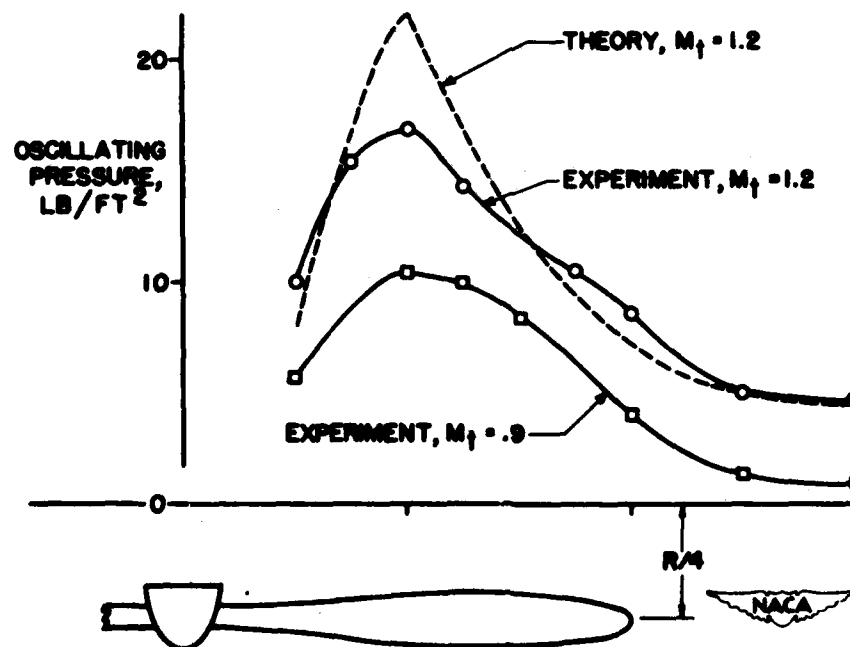
Figure 4.- Free-space pressure distributions of the fundamental Fourier component ahead of a propeller.
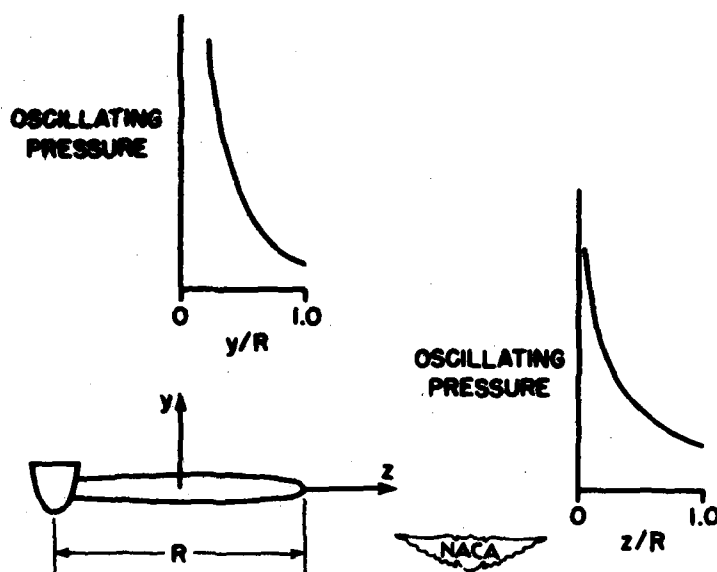
Figure 5.- Free-space pressures of the fundamental Fourier
component as a function of distance from the propeller.
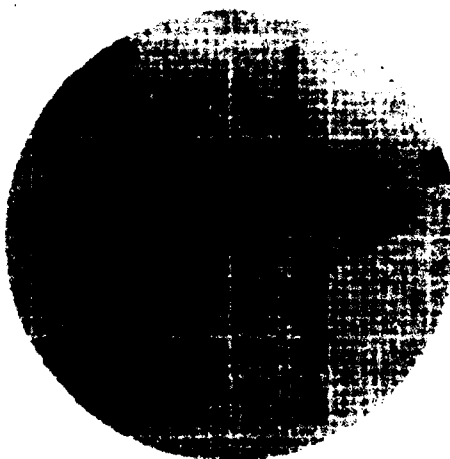
L-68450

Figure 6.- Sample wave form of total pressure in free space.

Figure 7.- Total-pressure distribution for free space compared to differential pressures across a thin wing.

Figure 8.- Distribution of total pressure at the surfaces of a thin wing during a propeller blade passage.

WING-ANALYSIS PROBLEMS

DEFLECTIONS OF SOLID M OR W AND SWEPT WINGS

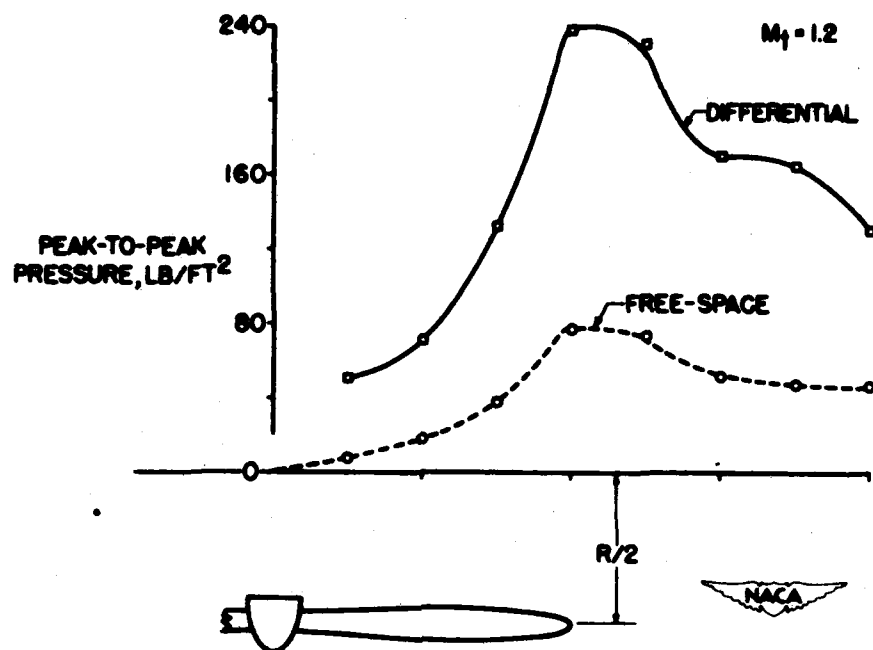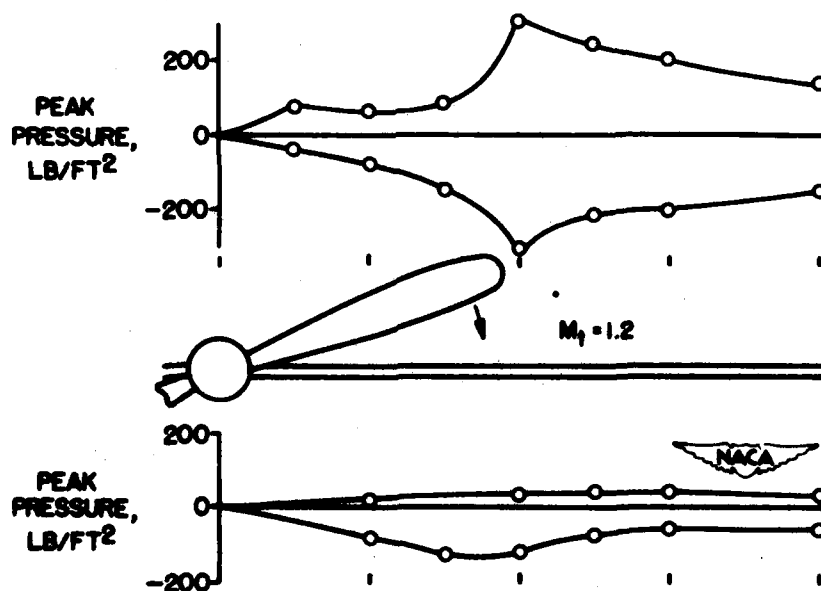## By George W. Zender and Richard R. Heldenfels

Langley Aeronautical Laboratory

Thin high-speed aircraft wings may be swept and have solid or nearly solid construction. Swept wings of fairly large aspect ratio (aspect ratios at least greater than 2) resemble ordinary cantilever beams outboard of the triangular region. This suggests that ordinary beam theory with slight modification may be used to calculate the deformations.

An experimental study is therefore being undertaken to determine the extent to which beam theory may be used for calculating the deformations of solid wings of swept and M or W plan forms. The first models tested in this program are shown in figure 1. The models had a rectangular cross section, 45° sweep angle, were of 24S-T4 aluminum alloy, and were full-span models with a center section. The center section was clamped between two tungsten carbide blocks and loads were applied to both halves of each model in order to minimize the effect of jig deformations. Systematic deflection data were taken on one side only, but two points were checked on the other side.

Figure 2 shows the deformations of the swept model subjected to vertical tip loads. The left-hand figure shows the vertical deflection of the center line and the right-hand figure shows the twist of the wing. Two types of twist are shown. The first is the twist about the center line which might be called the structural twist and is designated by the symbol θ. The other is the twist measured in a plane parallel to the root which is equivalent to the angle of attack and which is designated by the symbol α. The angle of attack α contains components of the twist θ and the bending slope. Figure 2 shows three theoretical curves which illustrate the results that can be obtained from ordinary beam theory, using various assumptions for the effective root. The root designated by the length L_1 measured along the center line results in too little deflection; the distance L_2, which is the length corresponding to the intersection of the center line and the clamped root, results in too much deflection. These two effective roots are the extremes which might result from an arbitrary selection. The figure also shows that an effective root one-third the distance from L_1 to L_2, designated by L, gives very good agreement with the test data for deflections. It is noticed, however, that the use of L slightly overestimates the angle-of-attack change. This results from using ordinary beam theory which neglects the small amount of structural twist produced by bending loads, as shown by the square test points in the right-hand figure. The component of this twist parallel to the root offsets slightly the angle-of-attack change due to bending of the model.

Many tests were made under vertical loads to determine the variation of the effective root location with the point of load application. Figure 3 summarizes the results of these tests. The location of the effective root a/b is plotted as a function of the ratio l/c. The distance a is measured from the rear corner of the sweptback wing to the effective root, and b is the distance from the rear corner to a root at the intersection of the center lines of the outer part and center section. The distance along the center line to the point of application of the load is designated by l, and c is the structural chord. The circles give the test results and the solid line has been faired through the test points. Note that as l/c becomes large, that is, bending moment predominates over shear at the root, a/b approaches a constant value. The two dashed lines are estimated locations of the effective root for sweep angles of 30° and 60°. These estimates are based on test data obtained from reference 1. This figure may also be used for a distributed loading and the effective root obtained considering l as the distance to the centroid of the loading.

A similar investigation was made to determine the effective root associated with a torque about the center line. The twists produced by a tip torque about the center line are shown in figure 4. It was found that the effective root could be taken at $L = L_2$, that is, $\frac{a}{b} = 1$, and the twist θ calculated from elementary torsion theory. The solid line shows the twists calculated with this effective root. The use of different effective roots for bending and torsion is inconvenient, but in most wing deformation analyses the torques are small compared with the bending moment and very little error is incurred by using the effective root for bending for the torques. In all the subsequent comparisons between experiment and calculations, the calculations were made on this basis.

Figure 5 shows the deformations produced by a couple applied to the tip of the swept model. The plane of the couple is parallel to the root; thus, effectively it is a combination of a torque and a bending moment. The deformations consist of deflections and rotations α and θ. Calculations are in good agreement with the test data. Effective root location was determined by taking $\frac{a}{b} = \frac{1}{3}$, which is the asymptotic value shown in figure 3.

Figure 6 shows similar results when the couple is applied at the half span. Note that outboard of the applied load, the rotations α and θ are constant and the deflection varies linearly as would be expected for rigid body movements. Calculations are again in good agreement with tests.

The preceding methods for the deformation analysis of swept wings can be applied to M or W wings if the inner and outer portions are treated as individual swept wings. Figure 7 shows the results for a vertical load applied at the tip of a W model. Again the left-hand figure shows the vertical deflection of the center line and the right-hand figure shows the twist. The plane of the structural twist θ is different for each part of the wing; thus, there is a discontinuity in the curve at the midspan station. Fairly good agreement is obtained between calculations and tests, but not quite as good as for the swept case. The procedure for analyzing the inner portion of the model is the same as that previously described for the swept model. The deformations of the outer part are obtained from superposition of rigid body motions due to deformations of the inner part and deformations of the outer part due to the loads on the outer part. The latter was calculated using an effective root determined from figure 3. Note that for this model, the inner part is under combined bending and torsion which causes a decrease in the angle of attack near the root, but farther outboard the angle of attack increases.

Figure 8 shows similar results for a vertical load applied at the half span of a W model. The location of the effective root a/b was 4/10 for the effective root at the inboard end of the model. No effective root was necessary for the outer panel since no loads were applied in this region. The calculated deflection and the rotations α and θ are constant in the outer part as would be expected from rigid body movements. The actual deflection varies slightly because of coupling between bending and twisting. Note that the angle of attack is negative at all stations along the span. Since the tip and half-span loads have opposite effects on the angle-of-attack change, the structural designer has some control over the angle-of-attack changes of M or W wings. For swept wings, however, all vertical shear loads cause a decrease in the angle of attack and no such control is possible.

Figure 9 shows results for a couple applied at the tip parallel to the plane of the root. Both parts of the model are under combined bending and torsion which cause both deflections and rotations. At the midspan station, where the direction of the loads change, the deflection shows a change in slope and θ has a discontinuity.

Figure 10 shows similar results when a couple is applied at the half span. In the outer part, which is not loaded, α and θ are constant and the deflection varies linearly.

In conclusion it has been shown that the deformations of swept and M or W wings can be calculated by elementary beam theory with effective roots. The accuracy has been demonstrated for 45° specimens and several types of arbitrary loads. The material presented is the initial phase of an investigation which will ultimately include the effective root location for other sweep angles, plan forms, and cross sections.

REFERENCE

1. DeGroff, Harold M.: Theoretical and Experimental Effect of Sweep upon the Stress and Deflection Distribution in Aircraft Wings of High Solidity. Part 3. Experimental Investigation of the Effect of Sweep upon the Stress and Deflection Distribution in Cantilever Plates of Constant Chord and Thickness. Tech. Rep. No. 5761, Pt. 3, Contract No. W33-038-ac-16961, GALCIT, Air Materiel Command, U. S. Air Force, Oct. 1950.
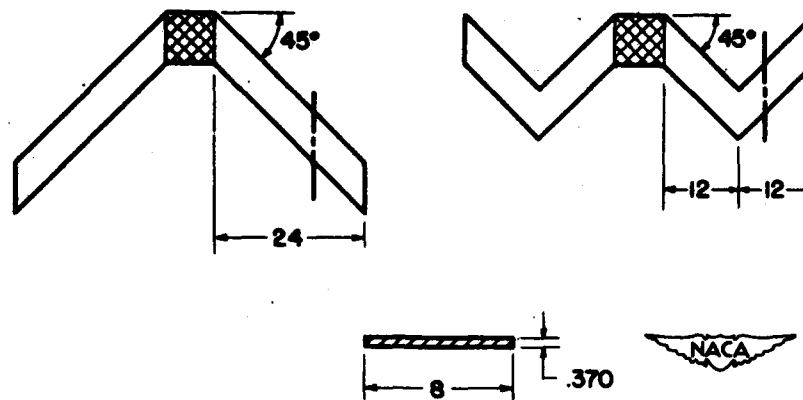
Figure 1.- Swept and M or W models.
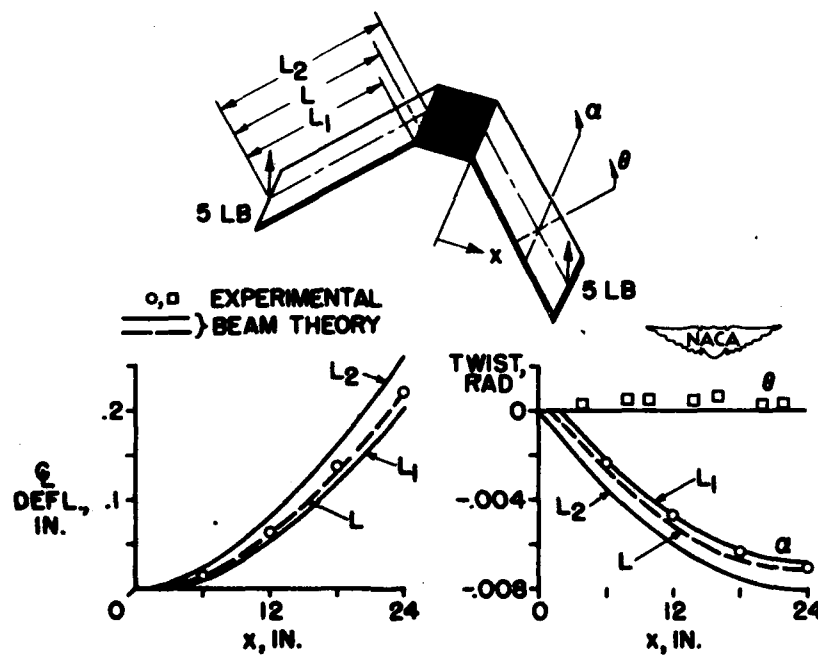
Figure 2.- Deflections and twists of swept model for vertical tip load.
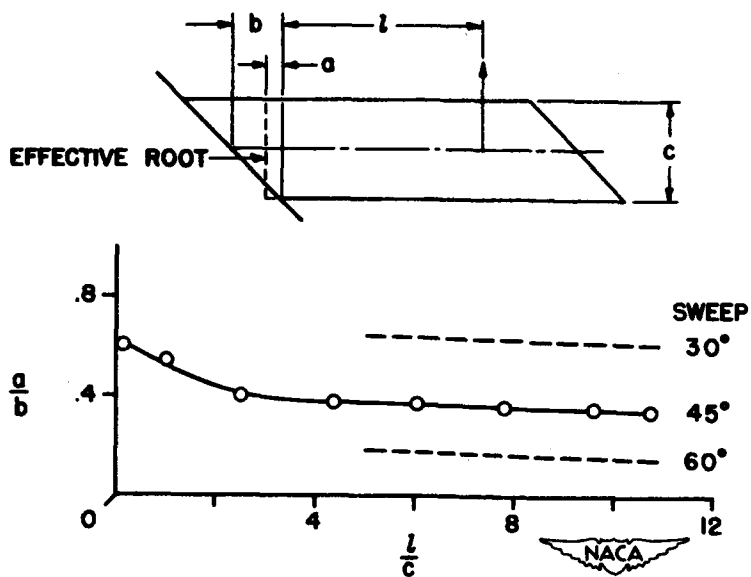
Figure 3.- Effect of load position on location of effective root.
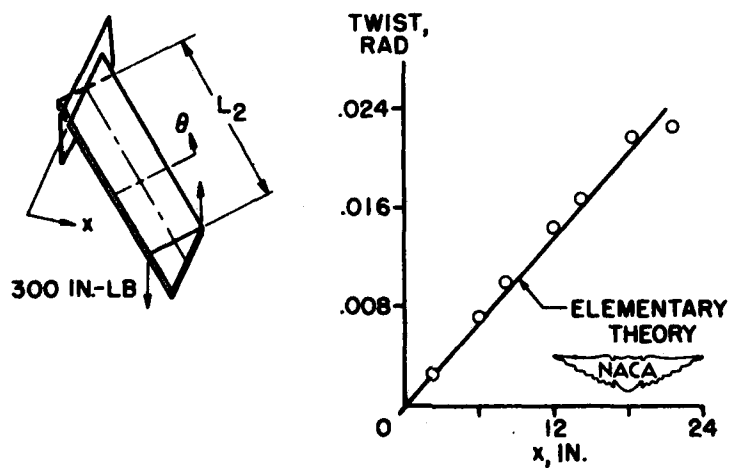
Figure 4.- Twist of swept model for tip torque about center line.

Figure 5.- Deflections and twists of swept model for tip couple.

Figure 6.- Deflections and twists of swept model for half-span couple.

Figure 7.- Deflections and twists of W model for vertical tip load.

Figure 8.- Deflections and twists of W model for vertical
half-span load.

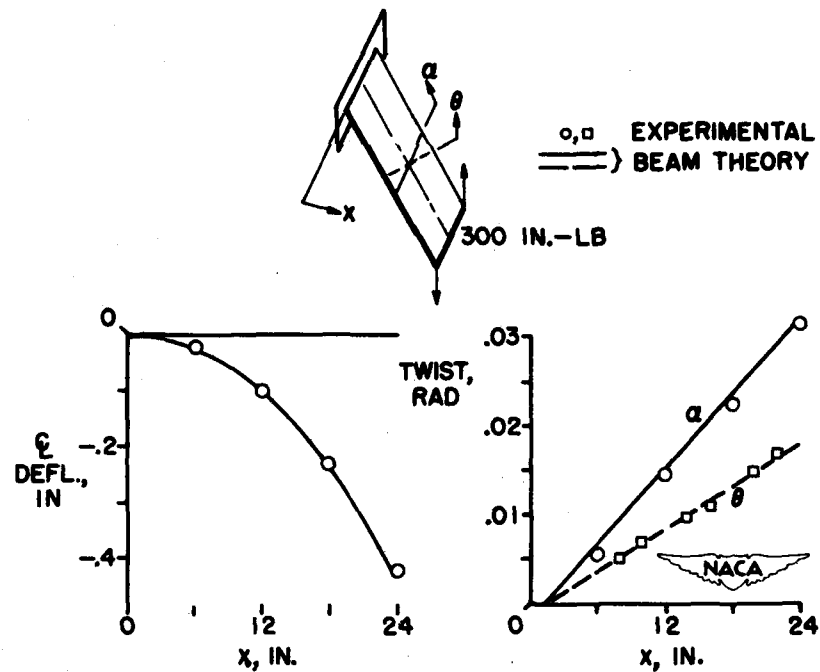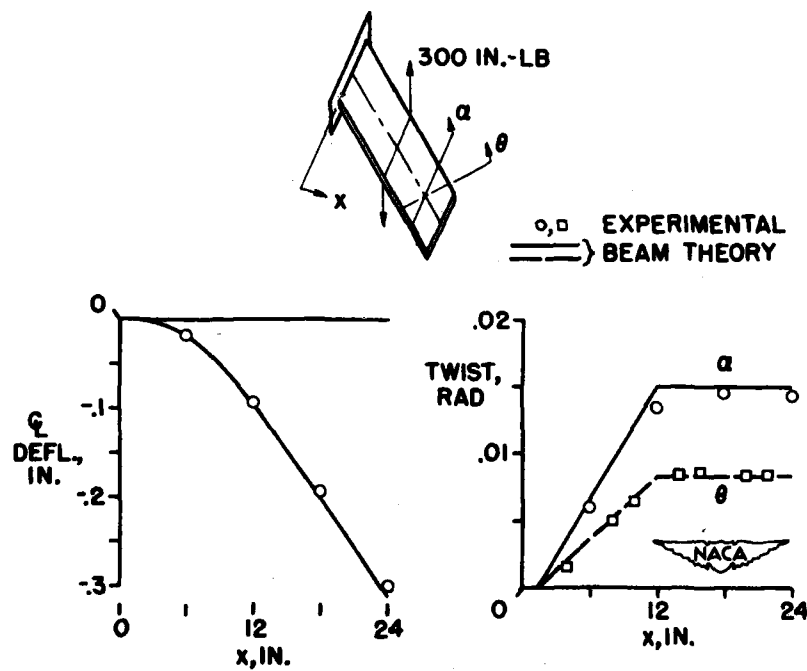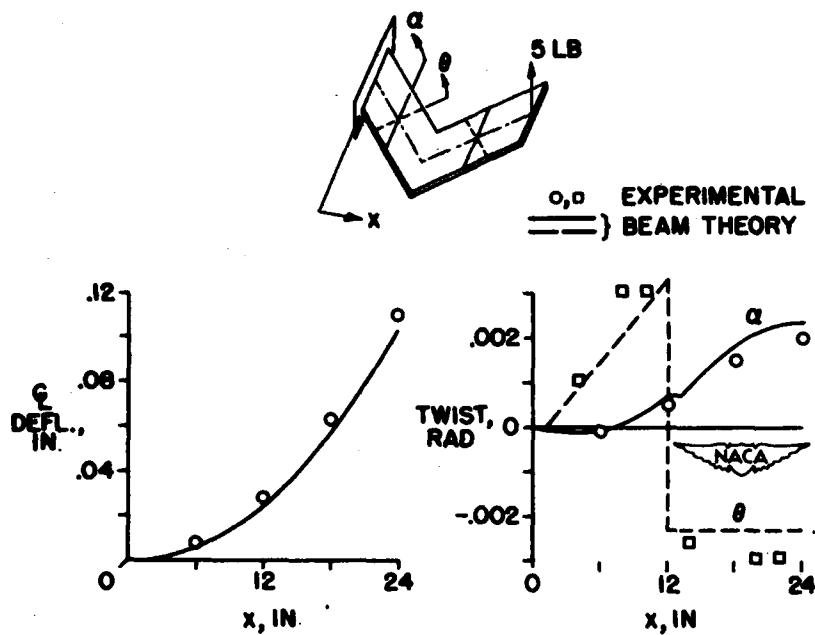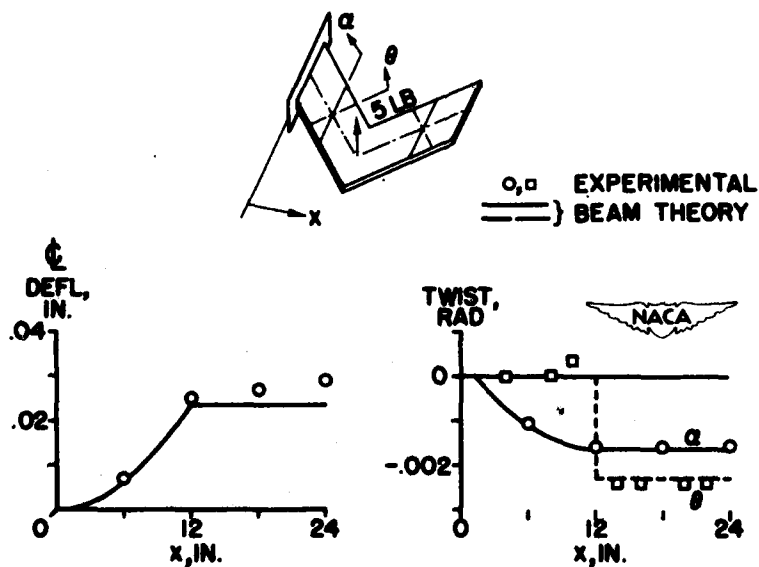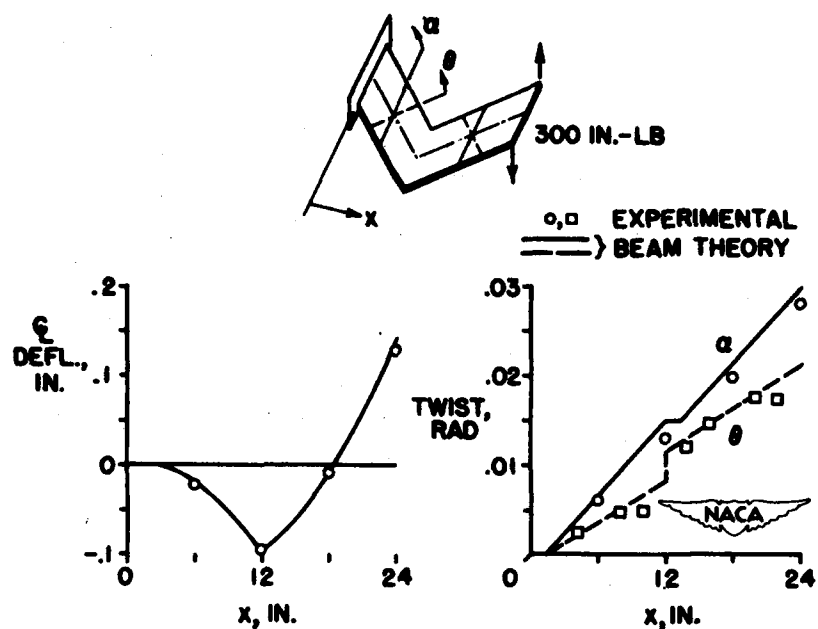Figure 9.- Deflections and twists of W model for tip couple.

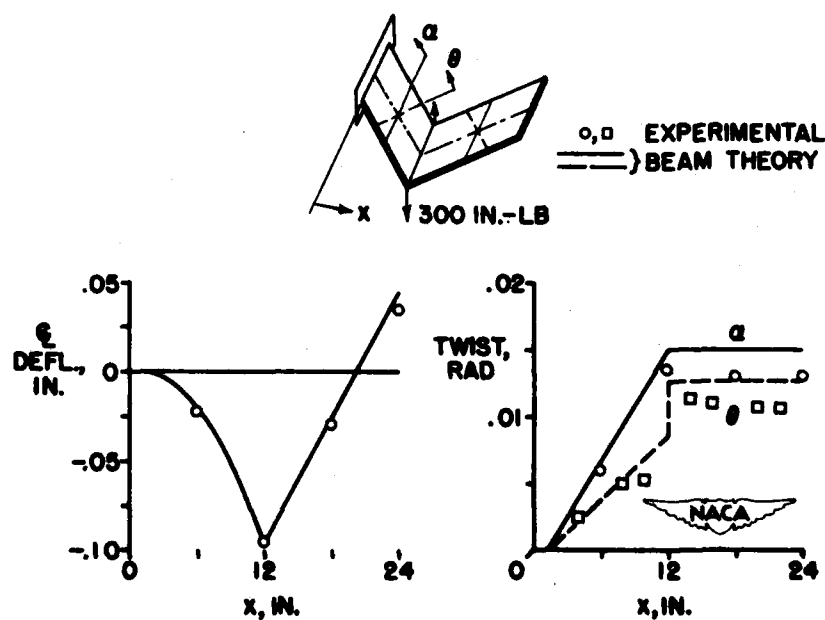Figure 10.- Deflections and twists of W model for half-span couple.

DEFLECTIONS AND STRESSES OF SOLID DELTA WINGS

By Manuel Stein and J. Edward Anderson

Langley Aeronautical Laboratory

The previous paper by George W. Zender and Richard R. Heldenfels has discussed the application of beam theory to thin solid wings of high aspect ratio. For thin solid wings of low aspect ratio it is no longer adequate to use beam theory to study structural deformation. Wings of this type are more nearly plates than beams and should be analyzed by plate theory. Plate theory, however, utilizes a fourth-order partial differential equation, solutions to which are not readily obtained, especially for plates of variable thickness under arbitrary loading. In a paper being prepared by the NACA there is presented an approximate plate theory based on a method suggested by Professor Eric Reissner for analyzing the distortion of such wings. (Essentially the same theory derived in a different manner has appeared in a very recent Swiss paper (see reference 1).) The present paper describes this theory and its application to delta wings.

Figure 1 shows a thin cantilever delta wing of arbitrary thickness variation. A natural assumption from the point of view of structural deformation and one that is convenient from the point of view of calculating aerodynamic loading due to structural deformation is that the deflection of any cross section parallel to the root consists of only a translation and a rotation. Thus, if the spanwise variation of the translation of the trailing edge is denoted by $W(x)$ and the spanwise variation of the rotation is denoted by $\theta(x)$, the deflection at any point in the wing is given by

$$w = W(x) + y\,\theta(x) \tag{1}$$

The right-hand side of equation (1) can be regarded as the first two terms of an expansion of w in powers of y. For greater accuracy a third term, $y^2\alpha(x)$, which represents a parabolic camber deformation may be added to the series. It might be mentioned that in assuming the displacement of any cross section to be made up of a translation and a rotation nothing new is being done. What is new, however, is that these quantities are being calculated more accurately by regarding the wing as a plate rather than as a beam.

The next step in the analysis is to choose the functions W and θ so as to minimize the potential energy of the system. This results in two ordinary differential equations for W and θ, which are given as follows:

$$\left(a_1 W''\right)'' + \left(a_2 \theta''\right)'' = p_1 \tag{2}$$

$$\left(a_2 W''\right)'' + \left(a_3 \theta''\right)'' - 2(1 - \mu)\left(a_1 \theta'\right)' = P_2 \qquad (3)$$

where

$$a_1 = \int_{TE}^{LE} D \, dy$$

$$a_2 = \int_{TE}^{LE} Dy \, dy$$

$$a_3 = \int_{TE}^{LE} Dy^2 \, dy$$

$$p_1 = \int_{TE}^{LE} p \, dy$$

$$p_2 = \int_{TE}^{LE} py \, dy$$

and

$$D = \frac{Eh^3}{12\left(1 - \mu^2\right)} = \text{Plate stiffness}$$

$$p = P(x, y) = \text{Lateral pressure}$$

$$h = h(x, y) = \text{Local thickness}$$

The primes denote differentiation with respect to x. The a's are functions only of the plate material and configuration and are defined by the integrals shown. The right-hand sides of these equations, p_1 and p_2, are the running lateral load and running torque, respectively, on sections parallel to the root and are given by chordwise integrals as shown here.

With equations (2) and (3) solved for W and θ the deflections of the wing are known. The stresses can then be determined by suitable differentiation of the deflections. The theory presented herein so far applies to solid or nearly solid thin wings under any loading of any

plan form, not only delta wings. In what follows some specific problems involving delta wings for which these equations have been solved exactly are discussed and comparisons are made with experiment.

Figure 2 shows a comparison between theory and experiment for the deflections of a 45° triangular plate of uniform thickness under uniform load. The circles show the experimentally measured deflections along the chord at the 0.2, 0.4, 0.6, 0.8, and tip spanwise stations. The dashed lines show the deflections at these stations calculated by means of equations (2) and (3). If the theoretical analysis is refined by the addition of the parabolic camber term previously mentioned, the solid curves are obtained which are in somewhat better agreement with the test results.

Figure 3 shows a similar comparison for a 60° triangular plate. Again the circles are experimentally measured deflections, the dashed curves were obtained by use of equations (2) and (3) and the solid curves by the analysis refined by the addition of the parabolic camber term.

Now let us look at the stresses. Figure 4 shows the comparison between theory and experiment for a 45° triangular plate of uniform thickness under uniform load. The circles give the experimentally determined maximum principal stresses along the chord very near the root and at the 0.2, 0.4, and 0.6 spanwise stations. Again the dashed curves give the results of calculations based on linear chordwise deflections and the solid curves include the effect of the parabolic camber term. While the linear approximation gave fairly accurate deflections, it appears from this comparison that the inclusion of the parabolic camber term is necessary for satisfactory stress calculations. The maximum stress occurs at the root at the trailing edge. It may be of interest to remark that this stress is 55 percent higher than the stress given by the usual Mc/I formula of beam theory. Thus, in a delta plate there is a stress concentration analogous to the stress build-up at the root of the rear spar in conventional sweptback wings.

For the purposes of examining theoretically the effects of change in cross-section shape and spanwise-thickness taper, an exact theoretical solution to the equations presented has been obtained for a triangular plate of diamond chordwise cross section and linear spanwise taper under uniform loading. The results for deflections along the leading and trailing edges are shown in figure 5 and for comparison there are shown the deflections along the leading edge and along the trailing edge of a uniformly thick triangular plate of the same weight under uniform loading. The tapered plate deflects considerably less, but the tip tends to curl up under the uniform loading.

In figure 6 theoretical stress curves are presented for the two 45° triangular plates of the same weight under uniform loading as was

done for deflections. The curves at the left show the stresses along the root chord. The curves at the right show stresses along the chord at 60-percent span. The maximum stress in the diamond cross-section plate is well below that of the uniform plate. Values of stress close to the maximum value appear all along the span of the diamond cross-section plate.

Figure 7 presents the results of an experimental investigation and a theoretical study of the natural vibration of a 45° triangular cantilever plate. This figure shows the shape of the nodes in the interior of the plate for the first three natural modes of vibration as determined by experiment. The upper numbers give the experimentally determined values of the frequencies. The lower numbers are the frequencies estimated by an approximate solution to the equations of the present theory by an energy method assuming only six degrees of freedom.

In general it may not be possible to obtain closed-form solutions of the differential equations presented for wings having certain desired airfoil section, taper, and loading. In such cases numerical methods may be used. To check the accuracy of the numerical methods for delta wings using the present theory, the case of a 45° triangular plate of uniform thickness under uniform load was solved by a numerical method which considers five stations along the span and which utilizes the simple quadratic differentiation approximation. A comparison between this numerical method and the closed-form solution of the differential equations is shown in figure 8 where the curves are the results of closed-form solution of differential equations (2) and (3) and the squares are the results of numerical solution of the same equations. The results are as good as can be expected. The solution involves five simultaneous linear algebraic equations for the linear chordwise deflection theory. For the parabolic camber theory it would be necessary to solve 10 equations.

A method of analyzing thin solid or nearly solid wings has been presented. This paper has shown that accurate results can be obtained by this method for triangular plates of uniform thickness under uniform load. It has also been indicated that the method is readily applicable to triangular plates of other than uniform thickness and that the equations of this theory may be readily solved by numerical methods.

REFERENCE

1. Schürch, H.: Zur Statik von dunnen Flugzeug-Tragflächen. Mitt. Nr. 2, Inst. für Flugzeugstatik und Flugzeugbau an der E.T.H., Leemann (Zürich), 1950.

$$w = \boxed{W(x) + y\,\theta(x)} + y^2\,\alpha(x)$$
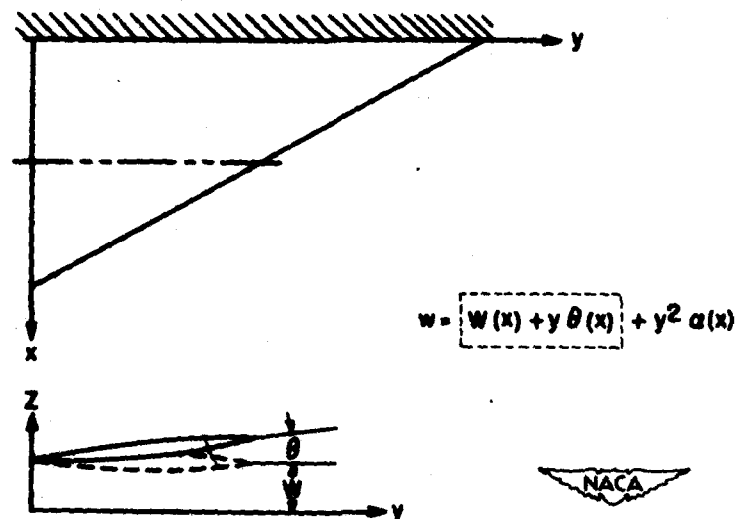
Figure 1.- Coordinate system and assumed deflection function used for a cantilever delta wing of arbitrary thickness variation.
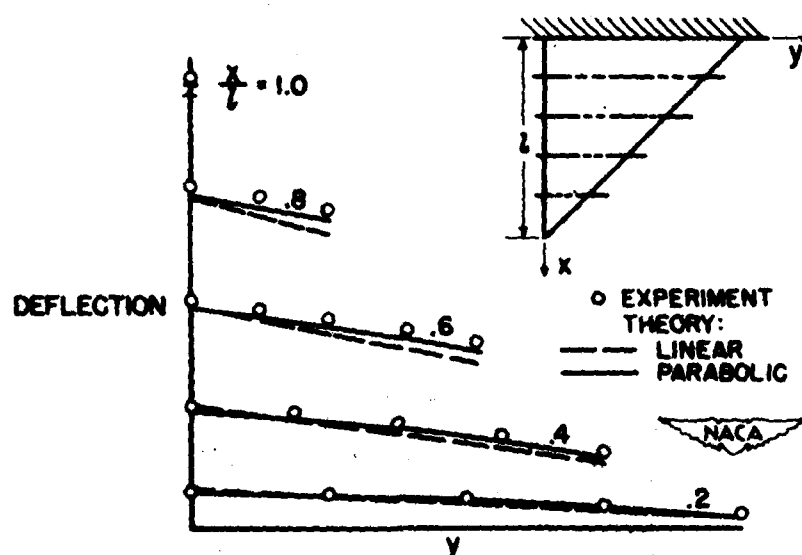
Figure 2.- Deflections of a 45° triangular plate of uniform thickness under uniform load.
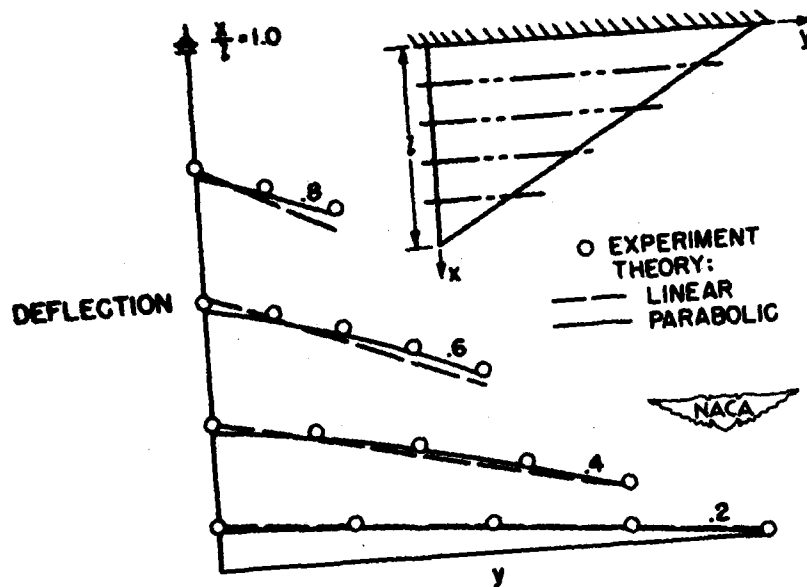
Figure 3.- Deflections of a 60° triangular plate of uniform thickness under uniform load.
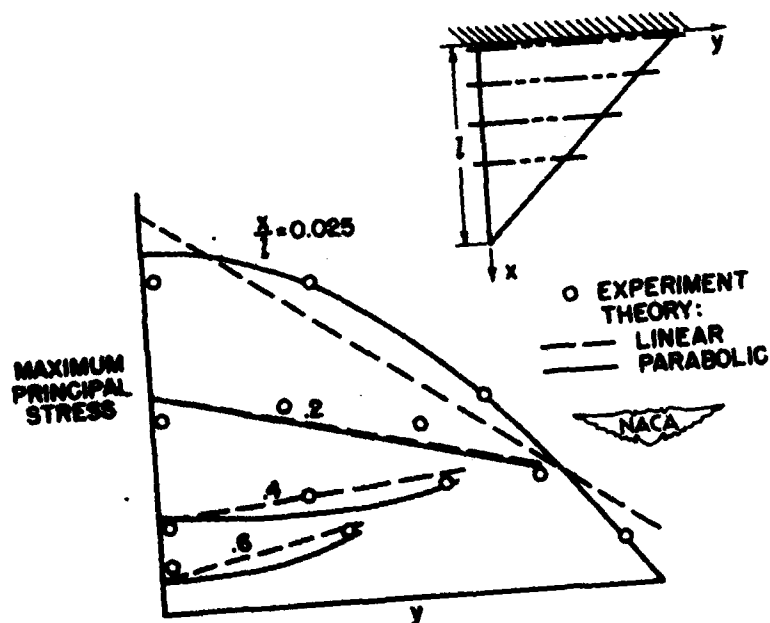
Figure 4.- Maximum principal stress in a 45° triangular plate of uniform thickness under uniform load.
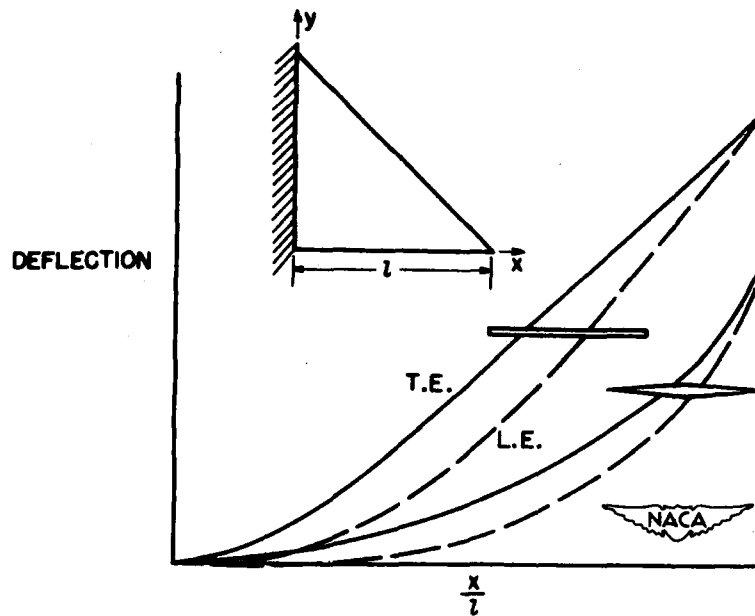
Figure 5.- Deflection under uniform load of uniform and tapered
plates of equal weight.

(a) $\frac{x}{l} = 0$.   (b) $\frac{x}{l} = 0.6$.
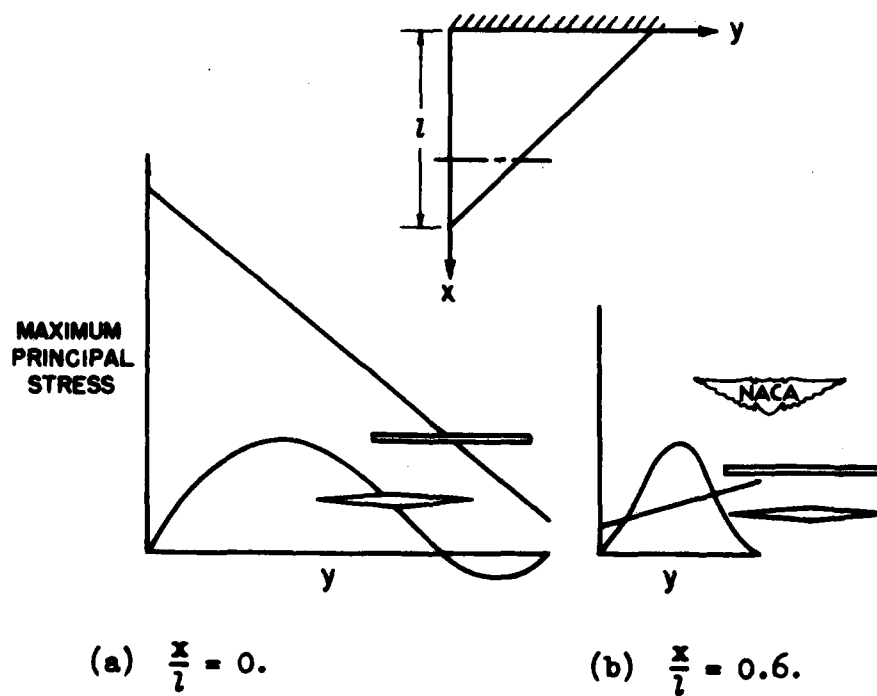
Figure 6.- Maximum principal stress under uniform load for uniform
and tapered plates of equal weight.
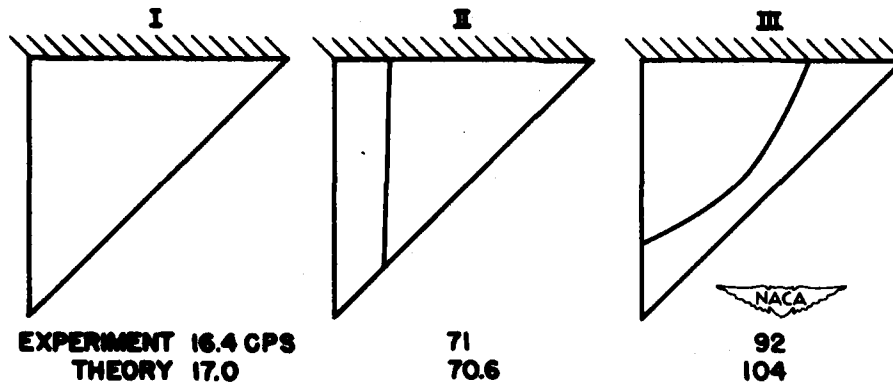
Figure 7.- First three modes of vibration of a uniform $45°$ triangular plate.
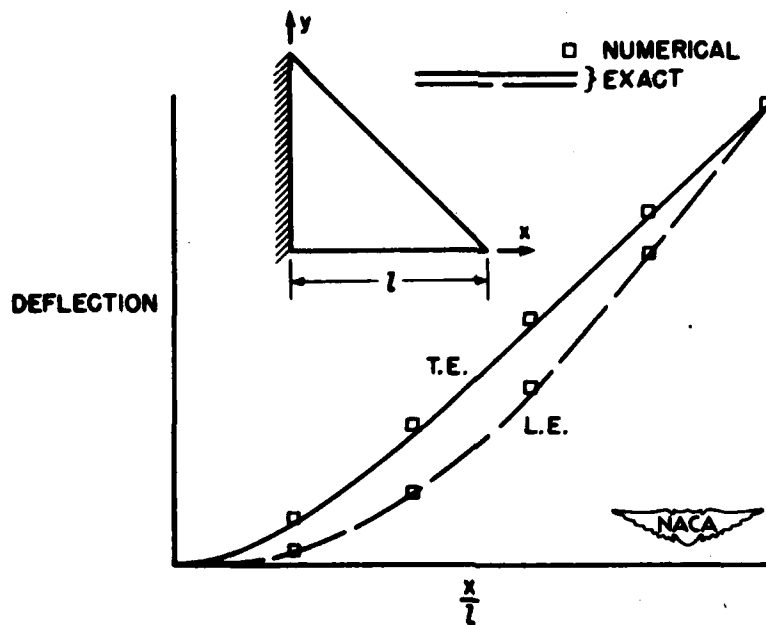
Figure 8.- Comparison of deflections of a $45°$ triangular plate obtained by numerical solution and by exact solution.

STABILIZATION OF COMPRESSION COVERS

OF SHELL WINGS BY POSTS

By Paul Seide and Paul F. Barrett

Langley Aeronautical Laboratory

Some interest has been displayed in the use of vertical posts as a means of stabilizing the thick compression cover of thin wings. In order to obtain information that might serve as a basis for design, a theoretical buckling analysis of this type of construction was made.

The theoretical analysis was confined to the type of structure shown in figure 1. The structure considered is a long box beam subjected to pure bending. The box beam consists of top and bottom covers (not necessarily of the same thickness), two side webs which are not shown, and vertical posts connecting the top and bottom covers. The chordwise and spanwise spacings of the posts are uniform; however they may differ from each other. Although only two spanwise rows of posts are shown here, the analysis applies to a box beam with any number of rows. In analyzing this structure, it was assumed that the covers remained flat and that the side webs provided them with simple support. The posts themselves were assumed not to restrict the rotation of the covers at the points of attachment.

In the computations attention was restricted to the problem of determining the post axial stiffness required for the posts to act as ribs or shear webs when buckling occurs; so that either transverse or longitudinal nodes through the posts could be obtained. With this axial stiffness the posts act as though they are rigid and no advantage results from increasing the stiffness. The results of the analysis and computations that apply to the particular case of covers of equal thickness are shown in figure 2. The ordinate is the required post axial stiffness and the abscissa is the ratio of longitudinal distance between posts to cover width L/b. To see the meaning of the curves, consider, for example, the curve which applies for a box with one spanwise row of posts. For any combination of L/b and post axial stiffness that falls on or to the right of the curve, buckling will occur with nodes through the posts, in this case with transverse nodes, where a chordwise line of posts acts as a rib. The buckling stress coefficient for transverse nodes corresponding to the particular value of L/b is given at the top of the chart. For any combination falling to the left of the vertical asymptote to this curve it is not possible to obtain rib action, and buckling will always occur with vertical movement of the posts. Rib action is obtainable at higher buckling stress coefficients if more rows of posts are used. Similar sets of curves were

obtained for various values of the ratio of tension-cover to compression-cover flexural stiffness and are presented in reference 1 where numerical values of post stiffness are given.

A summary of the buckle patterns obtainable by using one spanwise row of rigid or effectively rigid posts is given in figure 3. Similar charts are available in reference 1 for two and three rows of posts. The three regions of the chart correspond to three different modes of buckling. For values of L/b and D_T/D_C, the ratio of the flexural stiffness of the tension cover to that of the compression cover, that fall in region I, buckling occurs with rib action along every chord-wise line of posts; in region II, with spar action along every spanwise row; and in region III, with vertical movement of the posts. The dashed lines represent the nodes that occur. Taking the value of $\frac{D_T}{D_C} = 1$, that is, covers of equal thickness, it can be seen that buckling with spar action cannot occur and that either buckling with translation of the posts or rib action, depending on the post spacing, is obtainable. It is apparent that, for ratios of cover flexural stiffness usually encountered in aircraft construction, spar action with posts cannot be obtained.

In order to obtain some idea of the behavior under load of an actual box beam stiffened by posts, the specimen shown in figure 4 was designed and tested. The nominal thickness of the covers was 3/8 inch, the box depth was about 6 inches, and the box width was 28 inches. Three rows of $\frac{3}{8}$-inch-diameter posts, spaced 6 inches in the spanwise direction, were used. The weight of the posts, including all attachment material, was about 6 percent of that of the compression cover. According to the theory, the box would develop a cover buckling stress of 40,000 psi, and the compression cover would buckle with transverse nodes through the posts.

The box beam was mounted in the combined load testing machine of the Langley structures research laboratory and subjected to a pure bending moment which put the upper surface in compression. Strains were measured at three locations on the upper surface of the top cover to serve as a basis for detecting buckling. The growth of the strains with applied bending moment is shown in figure 5. If the structure behaved as an ordinary beam, the strains would be expected to increase linearly with moment. The noticeable departure of these curves from linearity is due to secondary bending effects which included an over-all downward dishing of the two covers relative to their edges. This over-all dishing continued to grow with load until it became of the order of the cover thickness and then, rather suddenly, there was super-imposed on it the buckle pattern indicated by the theoretical analysis, namely, a short-wave pattern with transverse nodes through the posts.

When this happened, the strains indicated by gages 1 and 3 reversed. The bending moment at which this strain reversal took place was taken as the experimental buckling load and was about 2 percent below the theoretically computed moment. The structure continued to take load until failure occurred through crippling of several posts at a point 8 percent above the strain-reversal buckling load.

The results of the test showed that despite differences between the test specimen and the idealized structure used in the analysis, the mode of buckling predicted by the theory does occur at the predicted load. However, the test also showed that significant prebuckling deformations may occur, namely, cross-sectional deformations due to downward dishing of the covers during bending. In actual wings, such cross-sectional deformations could very likely produce undesirable aerodynamic effects, and it would therefore be necessary to use supplementary stiffening to maintain the airfoil shape. Possibly for proportions similar to those tested a proper combination of posts and ribs would make a satisfactory design both from the viewpoint of deformations and strength. Possibly for some other proportions posts alone would be adequate.

REFERENCE

1. Seide, Paul, and Barrett, Paul F.: The Stability of the Compression Cover of Box Beams Stiffened by Posts. NACA TN 2153, 1950.

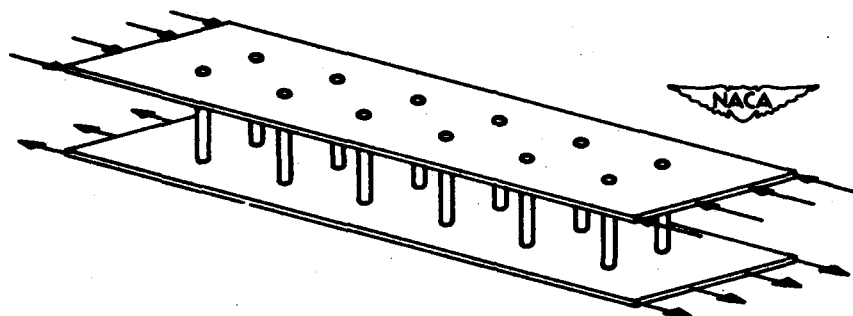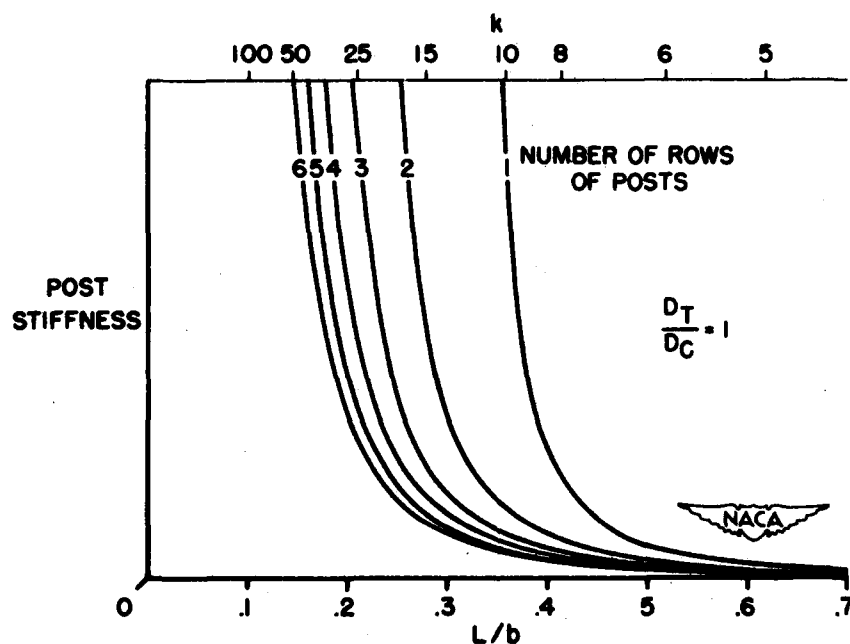Figure 1.- Idealization of box beam stiffened by posts.

Figure 2.- Minimum post axial stiffness required for
compression cover to buckle with transverse nodes
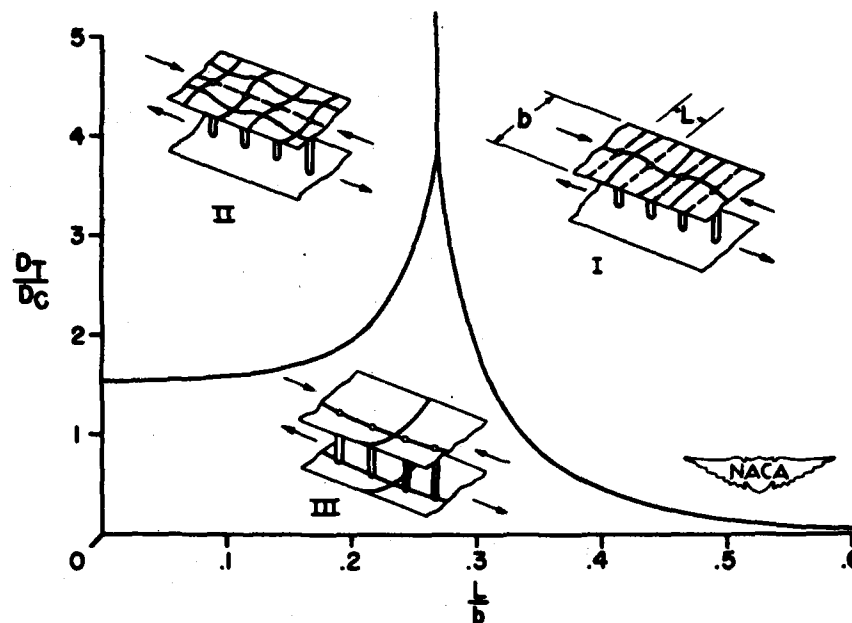through the posts.

Figure 3.- Buckling phenomena attainable for box beams with rigid or effectively rigid posts.
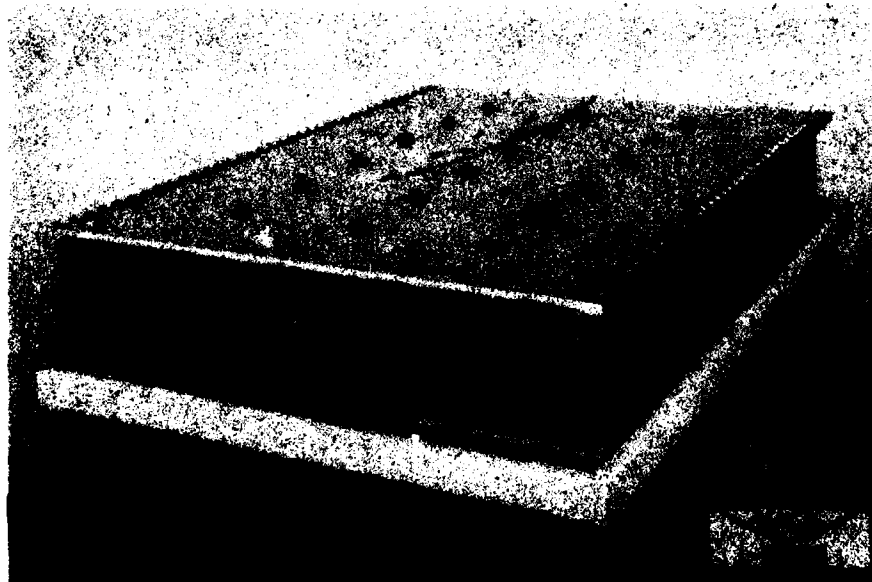
Figure 4.- Box beam used in experimental investigation.
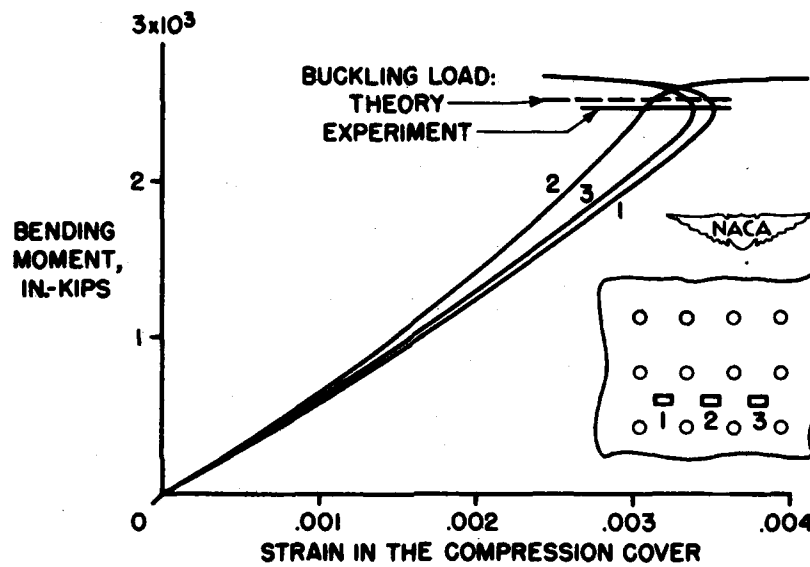
Figure 5.- Load-strain curves for box beam stiffened by posts.

STABILITY OF MULTIWEB BOX BEAMS

By Richard A. Pride, Aldie E. Johnson, Jr.,
and Roger A. Anderson

Langley Aeronautical Laboratory

The thinness of wings required for high-speed aircraft leads, in some cases, to the use of multiweb construction, (fig. 1). The skin in the central portion of the airfoil section may be slightly curved or flat as dictated by aerodynamics. The webs may be integrally attached to one of the skin surfaces or may be joined by attachment angles and riveting.

The buckling strength of the resulting multiweb beam has been investigated theoretically when subjected to a pure bending moment (reference 1). It has been found that for a beam with integral joints and many webs, beam buckling can be predicted by the usual plate buckling formula

$$\sigma_{cr} = \frac{k_c \pi^2 \eta E t_c^2}{12\left(1 - \mu^2\right) b_c^2}$$

where η is a plasticity correction factor and the value of k_c can be obtained from figure 2. In this figure k_c is plotted against the ratio of web depth b_w to the web spacing b_c for several ratios of web thickness to cover-plate thickness. Buckling coefficients greater than 4 indicate beam proportions for which the webs provide a stabilizing effect to the covers. Coefficients below 4 indicate beam proportions where the webs have a destablizing effect on the cover. Crushing stress induced in the webs by bending of the covers has been neglected. In the course of planning experimental research, charts similar to figure 2 were also prepared for the case of a beam with only two shear webs and also for the case of three shear webs, whereas this chart is for the case of many shear webs. When the k_c values given in figure 2 for $\frac{t_w}{t_c} = 1.0$ for multiwebs are compared with the corresponding curves for the two- and three-web construction (fig. 3), it can be seen that the curves do not greatly differ. Accordingly, the simpler two-web section was selected for the experimental study.

Results of pure bending tests on two-web sections are shown in figure 4. The experimental buckling stress is plotted against calculated buckling stress and the closeness of the points to a 45° line

indicates the adequacy of the pure bending theory. Both elastic and
plastic buckling tests are included in this data. Various airplane
companies and other laboratories have conducted tests on fabricated
beams, and in those instances where the type of fabrication approxi-
mated integral joints between webs and covers (for example, refer-
ences 2 and 3), the agreement with theory was satisfactory. In other
tests in which beams were fabricated with thin webs and heavy covers
jointed by substantial attachment angles, buckling of webs and covers
occurred independently and the present integral-plate theory was not
applicable. Some theoretical and experimental research is being done
to study the effect of attachment angles on the behavior of fabricated
beams. The remainder of this discussion will be confined, however, to
beams in which a definite interaction between web and cover buckling
exists.

The buckling produced by a spanwise variation in bending moment
will now be considered. Since multiweb beams used in aircraft wings
are subjected to distributed loads, the webs of the beam carry shear
stress and the bending stress varies along the span. A buckling ana-
lysis of a multiweb beam under this general kind of loading has not
been made. However, analyses have recently been made of the webs alone
and compression covers alone, which indicate significant qualitative
effects.

Figure 5 shows the theoretical interaction curve between pure
bending and pure shear in a single simply supported web plate. The
figure is plotted in terms of the ratios of particular stresses present
under combined loads to the critical values of those stresses when they
are acting alone. Gradient in the bending moment has been neglected,
but the effect of crushing stress of the type produced by bending of
the covers has been included. A different interaction curve is shown
for each of several values of the crushing-stress ratio. The flatness
of the curves near their upper ends indicates that the ability of the
webs to carry bending stress is not reduced substantially until the
shear stress approaches its critical value. The closeness of the
curves near their upper ends shows that for moderate values of shear
stress the crushing stress has little effect on the bending strength of
the web. It is only when the shear is large that the crushing stress
need be considered as a contributing factor.

Figure 6 shows the results of theoretical calculations (refer-
ence 4) for buckling in compression of a simply supported plate repre-
senting a portion of the compression cover bounded by two webs and two
ribs. The effect of a linear stress gradient on plates of three length-
to-width ratios is shown. Beneath the plates are the corresponding
nondimensional buckling-stress diagrams. The horizontal line is the
uniform stress required to buckle the plate and is shown as 100 percent

stress at buckling. The sloping lines represent different degrees of gradient stress at buckling. Here it is seen that the stress at the more highly stressed end of the plate is appreciably higher at buckling than the uniform compressive stress required to buckle the plate. This effect is especially pronounced in the smaller aspect ratios.

In a qualitative way, the theoretical work just described for the individual components indicates that beam buckling strength of a multi-web beam as predicted by pure bending theory should be adversely affected by the presence of shear and crushing stresses in the webs but should be increased by the presence of stress gradients in the covers as well as the webs. In order to study the over-all effect of web shear and moment gradient on a beam, NACA has proceeded with an experimental program.

Figure 7 shows the type of test being conducted. The two-web section is supported as a cantilever beam with a concentrated shear load and end moment applied at one end of the beam. This produces a constant shear diagram and a moment diagram which varies linearly from a minimum at the outboard end to a maximum at the inboard end of the test section. By use of the combined load testing machine of the Langley structures research laboratory, the values of the minimum moment and the maximum moment and the shear load at buckling can be changed in the test section. The test section may be thought of as representing any one bay between bulkheads of a wing.

The results of tests are presented in figure 8, as a series of moment diagrams at buckling for a beam subjected to various loadings. The length between bulkheads of this particular beam is 9.6 times the spacing of shear webs. The horizontal line is the pure bending moment required to buckle the beam and is shown as 100 percent pure bending strength. The lines of various slopes represent moment diagrams resulting from various amounts of shear loading. The maximum moment developed at buckling was greater than 100 percent, and the length over which the uniform buckling stress was exceeded was about twice the spacing of shear webs. For this particular beam this result is not surprising, since for the greatest shear loading the web shear stress was only about 6 percent of its critical value. Also, the crushing stress was only about 1 percent of its critical value. These small values result in an extremely small reduction of pure bending strength for a web plate (see fig. 5). The corresponding reduction for the beam as a whole is negligible.

NACA is proceeding with tests on beams with webs thinner than the cover so that the web shear stress will be larger in relation to its critical value than in the test results presented here. On the basis of the tests that have been completed, it can be concluded that for

long beams under gradient bending in which the web shear and crushing stresses are not large in comparison to their critical values, the pure bending strength can be exceeded over a length equal to one to two times the spacing of shear webs at the more highly stressed end of the beam.

REFERENCES

1. Schuette, Evan H., and McCulloch, James C.: Charts for the Minimum-Weight Design of Multiweb Wings in Bending. NACA TN 1323, 1947.

2. Islinger, J. S.: Bending Tests of Multi-Web Beams Using Thick 75S-T Sheet and FS-1h Sheet Cover Skins. Rep. No. 950, ser. no. 8, McDonnell Aircraft Corp., Sept. 9, 1948.

3. Eggwertz, Sigge F.: Buckling Stresses of Box-Beams under Pure Bending. Rep. No. 33, Aero. Res. Inst. of Sweden (Stockholm), 1950.

4. Libove, Charles, Ferdman, Saul, and Reusch, John J.: Elastic Buckling of a Simply Supported Plate under a Compressive Stress That Varies Linearly in the Direction of Loading. NACA TN 1891, 1949.
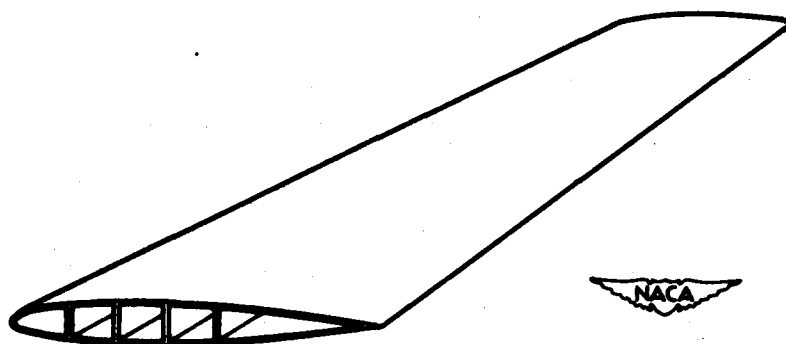
Figure 1.- Multiweb wing.
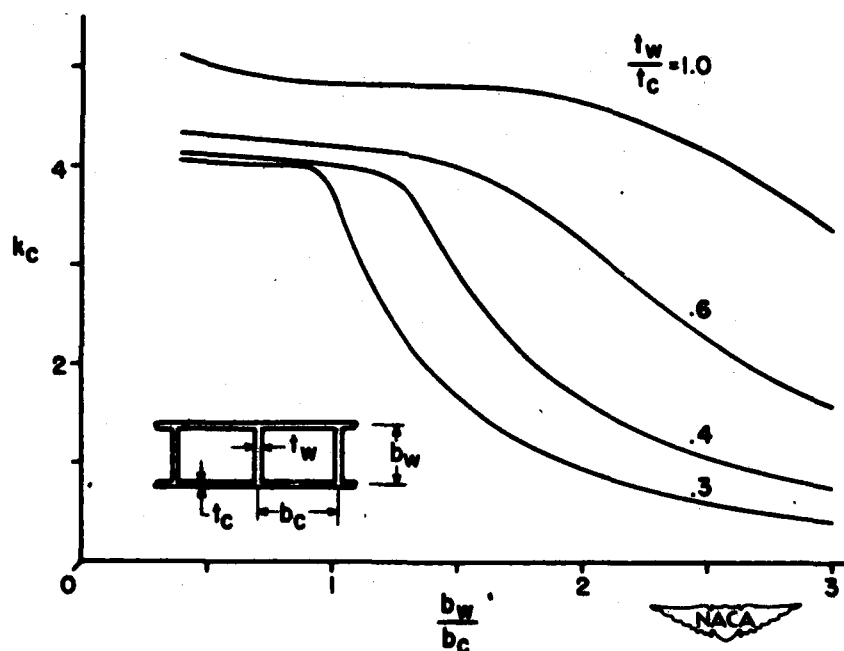
Figure 2.- Values of k_C in the formula for critical stress of multiweb beam under pure bending. $\sigma_{cr} = \dfrac{k_C \pi^2 \eta E t_C{}^2}{12\left(1 - \mu^2\right) b_C{}^2}$.
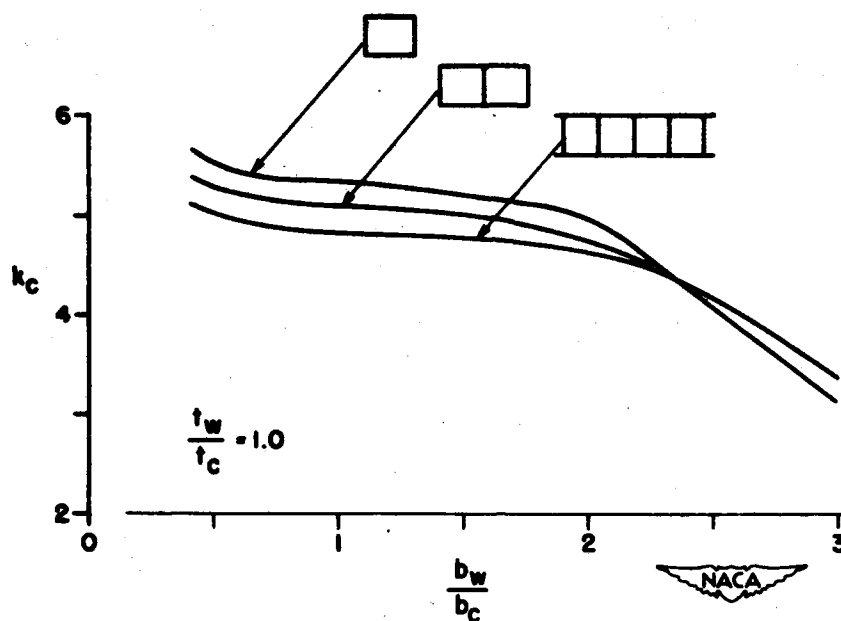
Figure 3.- Influence of number of webs on k_C for beams in pure bending.
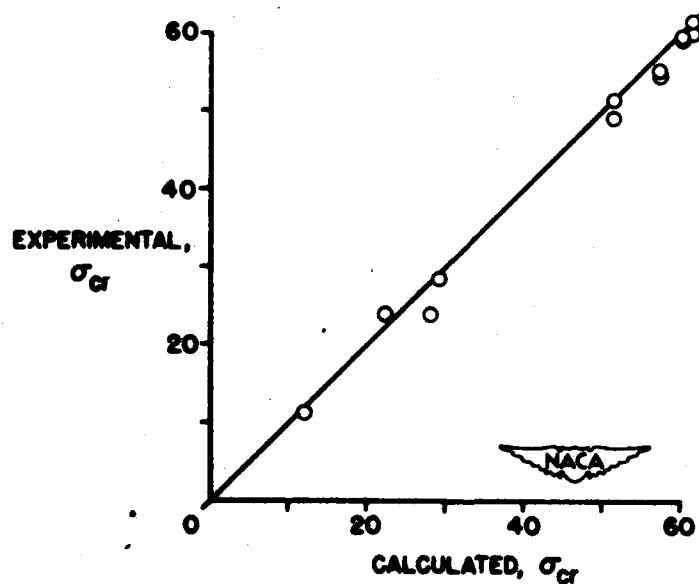
Figure 4.- Comparison of calculated and experimental buckling stresses for two-web section under pure bending.
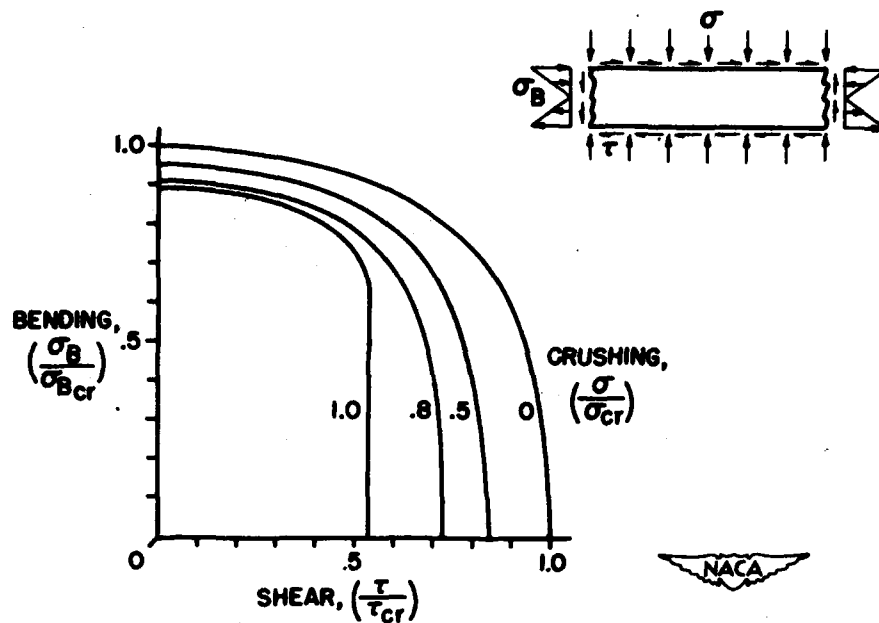
Figure 5.- Combinations of shear, bending, and crushing stress which produce buckling of an infinitely long flat plate with simply supported edges.
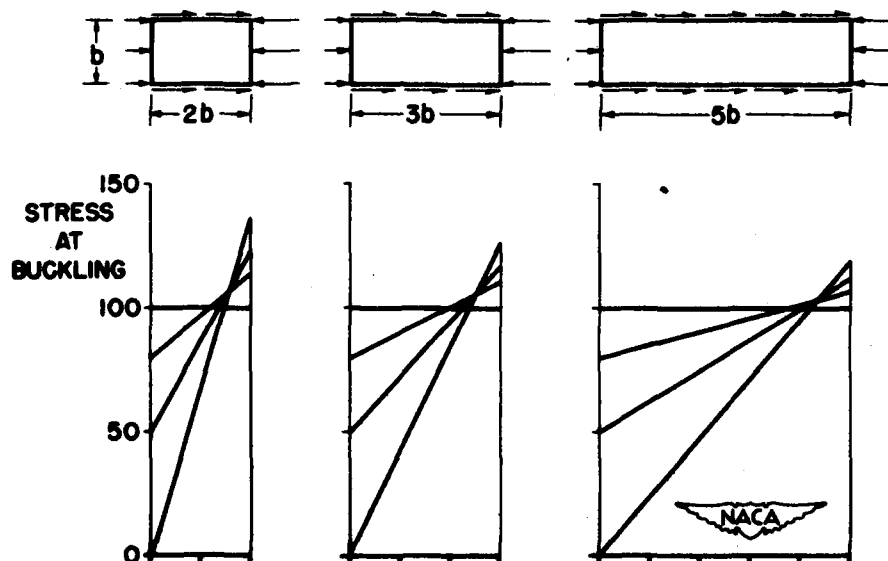
Figure 6.- Theoretical stress diagrams at buckling for simply supported plates under a compressive stress that varies linearly in the direction of loading.
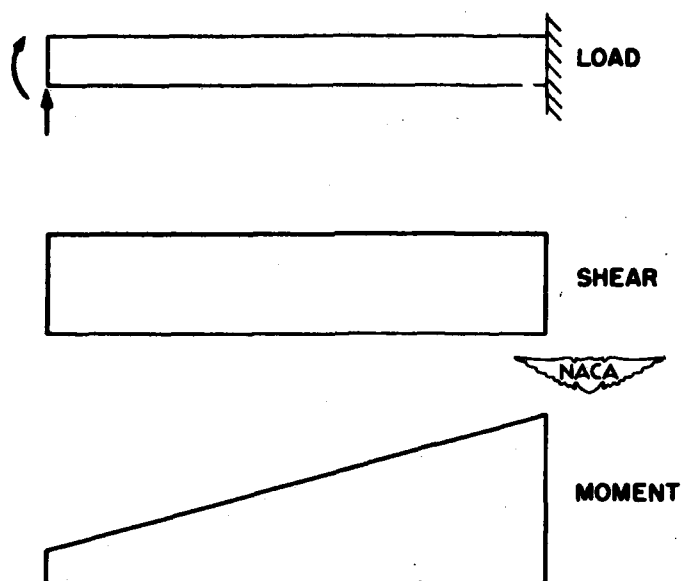
Figure 7.- Loading, shear, and moment diagrams for test specimen.
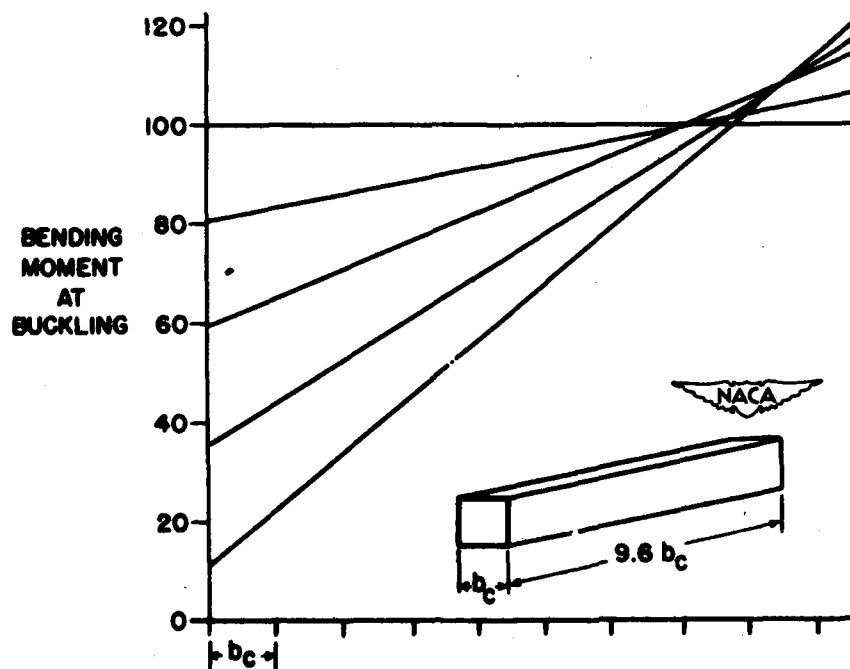
Figure 8.- Experimental moment diagrams at buckling for test specimen under gradient bending.

DESIGN FOR STIFFNESS AS WELL AS STRENGTH

By Norris F. Dow

Langley Aeronautical Laboratory

INTRODUCTION

While there have been a number of studies of minimum weight design of aircraft structures, most of them have been concerned primarily with the strength-to-weight ratio of the structure rather than the stiffness-to-weight ratio. The reason that the major emphasis has been upon strength rather than stiffness is that until recent years a structure of adequate strength would usually achieve adequate stiffness automatically. Now stiffness is becoming more of a problem, partly because higher speeds are imposing more severe stiffness requirements and the accompanying thinner wings are making these requirements harder to meet, and partly because increases have been made in the strength-to-weight ratio without corresponding increases in the stiffness-to-weight ratio, so that the more efficient structure from a strength standpoint has become less likely to be adequately stiff.

The present paper is a study to determine what are the possibilities of increases in stiffness-to-weight ratio. This study is made along two lines to determine the possibilities associated with

(1) The use of the most effective distribution of a given material

(2) The use of the most effective material

A few detailed studies of both stiffness and strength are made along both these lines, and current and possible future developments are discussed.

MOST EFFECTIVE DISTRIBUTION OF MATERIAL

First let us consider the possibilities associated with the most effective distribution of material. The principles involved in the distribution of material for maximum stiffness are extremely elementary, consisting basically of putting the material where it will carry the load most directly. If you have a simple tension load, you don't carry it with a helical spring; you use a straight rod. If you have a bending load, you don't use a plus-sign section; you use an I-beam. (See fig. 1.)

By the same token, if you are primarily concerned with torsional stiffness of the wing, you would prefer not to put a big percentage of material in longitudinal stiffeners but to put as much as possible of the material in the skin where it will work for you, as suggested schematically in figure 2.

In more technical language, the principles for obtaining maximum stiffness can be stated thus:

(1) Put the material at the point of maximum stress, in the direction of maximum stress.

(2) Keep the distance over which the high stress acts to a minimum.

(3) Avoid local or general bending or twisting distortions which reduce the effectiveness of the material.

(4) Avoid slippages in joints by making the structure as integral as possible.

Because of the desirability of making everything as integral as possible and because of general interest in integral stiffening, a detailed study has been undertaken of the characteristics of sheet with various configurations of integral stiffening. Integrally stiffened sheet has been proposed in a number of configurations (references 1 to 4), varying from fairly simple ribbing to complex gridworks tailored for specific designs. In order to make our study cover as many of these configurations as could reasonably be done, we considered first simple longitudinal or transverse ribbing (see fig. 3), and then the case for which the ribs are skewed at an angle θ to the longitudinal axis. The resulting waffle-like plates have densities and properties that can be varied by varying size, spacing, and orientation of ribs. The present paper is concerned primarily with the stiffness properties of waffle-like plates, specifically their axial and shear stiffnesses, which are related to the stiffnesses which waffles can provide to resist bending or twisting of the structure as a whole, and the bending and twisting stiffnesses of the waffles themselves, which are related to their own resistance to local bending or buckling distortions. After all, the main reason for having stiffening of any kind is to increase the resistance to local deformations. If it were not for such local deformations or buckling, simple solid sheet could be used, and such solid sheet would always provide a structure of maximum stiffness for a given weight of a material. The problem is to increase the buckling resistance of sheet with the least possible loss in its compressive and shear stiffness properties.

Let us examine first the compressive and shear stiffness properties of a typical waffle. With the waffle as the upper surface of the wing, the compressive stiffness measures the stiffness provided against bending of the wing, and the shear stiffness measures the stiffness provided against twisting of the wing. Curves of compression and shear stiffnesses for a typical waffle proportion are plotted in figure 4. In this figure the ordinate is the ratio of stiffnesses of waffle and solid sheet of equal weight, and the abscissa is the angle θ at which the ribs are skewed. The curves were calculated assuming pin joints at the corners of the grids. With such pin joints the compressive stiffness decreases to a minimum with the ribs at approximately $60°$, and the shear stiffness increases to a maximum with the ribs at $45°$. Accordingly, from the standpoint of stiffness of the wing as a whole, the choice of the best angle for the stiffening elements depends upon the relative importance of the bending stiffness and the torsional stiffness of the particular wing in question.

As might be expected, skewing the stiffening elements also affects the stiffness of the waffle to resist local deformation or buckling. Evidently, the choice of the best angle for the stiffening for a particular application can hardly be made on the basis of axial or shear stiffness properties alone. Calculations, similar to those for the axial and shear stiffnesses, of the bending stiffness and the twisting stiffness of the waffle show that these properties vary even more substantially than the compression and shear properties as the angle of ribbing is varied. The curves of bending and twisting stiffnesses are plotted in figure 5 as the ratio of stiffnesses of waffle and equal weight solid against the angle of ribbing. While the compression and shear stiffnesses were never greater than those of equal weight solid sheet, the bending and twisting stiffnesses can be substantially greater and, hence, the buckling strength can be increased.

In order to determine approximately what are the effects of skewed stiffening on the buckling strength, buckling loads were estimated from the bending and twisting stiffnesses using orthotropic plate theory. The resulting values for the buckling loads showed that for a given waffle proportion in the elastic range the critical compressive load should increase as the ribs are skewed because of the profound effect on buckling of the twisting stiffness which is a maximum at $45°$. Although this was only a preliminary analysis it was qualitatively confirmed by elastic buckling tests of long square tubes made up from waffles. In figure 6 are plotted the results of the buckling tests on waffles having ribs at $0°$, $30°$, and $45°$. In each case the circle represents the measured critical load divided by the critical load for a solid sheet of equal width and weight. The results confirm that the stiffening elements can be skewed to increase the shear stiffness, and at the same time the elastic compressive buckling strength is actually increased.

If the waffle is compared with conventionally stiffened (that is, riveted up) construction, it appears to have several favorable features from the stiffness standpoint quite apart from those associated with favorable angular orientation. First, because the waffle can readily be provided with high twisting as well as longitudinal and transverse bending stiffnesses, it can be expected to resist buckling with less over-all depth of section than the conventional panel. Accordingly, it can be effectively placed out closer to outside fibers to contribute greater bending or twisting stiffnesses to the structure as a whole. Second, proper proportioning of skin and grid permits ineffectivenesses due to local buckling distortions of the skin to be readily avoided. And third, any losses in stiffness due to loosenesses in riveted joints between skin and stringers are obviously completely eliminated.

The foregoing discussion of waffle-type stiffening has been concerned primarily with the stiffness properties, and the evaluation of stiffness properties are only one small phase of the structural evaluation of such integrally stiffened construction. Studies of other properties such as ultimate strength characteristics are proceeding, and Langley is negotiating with the Wyman-Gordon Company in order to obtain some waffles fabricated as press-forgings to aid in these studies. The test specimens which were made to check the buckling strengths were castings and hence are of no value for other than such tests entirely in the elastic stress range.

MOST EFFECTIVE MATERIAL

Let us now turn to the consideration of the possibilities associated with the use of the most effective material. Perhaps the first idea that comes to the mind of the aircraft designer confronted with the problem of making the structure stiffer is to use steel in place of aluminum. Steel has a Young's modulus $2\frac{1}{2}$ to 3 times that of aluminum and its smaller volume for the same weight permits it to be crowded out closer to outside fibers. This smaller volume, however, is usually the stumbling block, for associated with it are the well-known buckling difficulties always associated with thin sheets, and buckling is of necessity accompanied by loss of effective widths of skin and hence losses in both stiffness and strength. Buckling difficulties can of course be reduced by the standard procedures of adding stiffeners, or possibly integrally stiffened steel plates similar to the various types just described could be fabricated.

Another possibility to be considered is a solid steel-faced magnesium-core sandwich. Let us examine the stiffness properties of

such a sandwich in the same way that we did for the waffle. In this case the variable is the relative thickness of faces and core, indicated pictorially in figure 7 by the curve and quantitatively by the value of the abscissa. In this figure is plotted the bending stiffness of the sandwich compared to solid aluminum of equal weight. One end of the curve represents zero core, that is solid steel; the other end represents solid magnesium. At the same time that the relative proportions of face and core are changed, the over-all thickness of the sandwich is changed, as represented by the width of the curve, in order to keep the weight constant. For the point on the curve corresponding to the proportions for which the sandwich has the same over-all thickness as well as the same weight as aluminum, the sandwich has approximately 40 percent greater bending stiffness than aluminum, or if the faces are made slightly thicker and the core correspondingly thinner so that the weight is still the same, the sandwich can be thinner and yet still somewhat stiffer in bending than aluminum.

This curve represents only the elastic bending stiffness and correspondingly the resistance to local deformation or buckling in the elastic stress range. The properties in the plastic range depend upon the stress-strain properties of the steel and magnesium alloy used, and both very high-strength steel faces and a high-strength magnesium-alloy core are needed if the sandwich is to compete with a high-strength aluminum alloy such as 75S-T6 at high stresses beyond the elastic range. For the case of 75S-T6 plate and a sandwich of equal weight and thickness, for example, these curves of figure 8 show the relative stress-strain characteristics when the sandwich is made with 4340 steel faces and ZK60A magnesium-alloy core. While a comparison on the basis of efficiency to resist plate buckling would be much more favorable to the sandwich than this, still these curves do indicate the necessity of using the best possible materials if the sandwich is to compete with 75S in the high stress region. Except for this region the sandwich can provide, with less thickness, resistance to buckling equal to that for aluminum of equal weight. Accordingly, for thin wings for which stiffness is critical a steel-clad magnesium skin can provide greater bending or torsional stiffness to the wing as a whole than aluminum skin of the same weight because the sandwich skin can be made thinner without reducing the resistance to local deformation or buckling and because being thinner it can be placed effectively nearer the extreme fibers of the wing.

At the present time the General Plate Company is attempting to fabricate for us steel-clad magnesium sandwiches for structural evaluation. General Plate has successfully bonded a number of dissimilar materials (see reference 5) and has had some success bonding steel on magnesium on small pieces, but as yet nothing of any size has been produced.

One feature to remember particularly about the curves for the steel-clad magnesium sandwich is that while the sandwich can have, for the same weight and thickness, greater elastic bending stiffness than aluminum, or for the same bending stiffness and weight it can have less thickness than aluminum and hence can provide greater bending or twisting stiffness to a thin structure as a whole, nevertheless, even in the elastic range, it has no greater axial stiffness than aluminum; that is, the initial slopes of the stress-strain curves for the sandwich and for equal weight aluminum are the same. To improve the axial stiffness characteristics (and correspondingly the shear stiffness characteristics) a material with a higher ratio of modulus of elasticity to density than magnesium, aluminum, or steel is needed.

The fact that such metals as magnesium, aluminum, titanium, and iron all have approximately the same modulus-to-density ratio, as noted in the following table, has given rise to the impression that there is little hope of any improvement in this ratio:

Material	Modulus $(10^6$ psi$)$	$\dfrac{\text{Modulus}}{\text{Density}}$ $(10^6$ in.$)$
Magnesium	6.5	103
Aluminum	10	102
Titanium	16	100
Iron	28	100

Higher values of the modulus-to-density ratio, however, are not contrary to nature. A number of materials having high modulus-to-density ratios are listed in the following table:

Material	Modulus $(10^6$ psi$)$	$\dfrac{\text{Modulus}}{\text{Density}}$ $(10^6$ in.$)$
Aluminum	10	102
Chromium	28	108
Molybdenum	46	125
Tungsten carbide	96	177
Titanium carbide	55	280
Beryllium	42	640

Chromium is a little better than aluminum; molybdenum is even better. In fact molybdenum might well be suitable for some highly specialized applications for which high stiffness is a primary requisite. If a face material similar to molybdenum were available for cladding magnesium, for example, it would make a very interesting sandwich. Molybdenum itself is probably too scarce to make a molybdenum-clad magnesium-core sandwich useful for other than limited applications. For possibly even more limited applications there are the carbides. For example, there is tungsten carbide which has a Young's modulus of 96,000,000 psi and a modulus-to-density ratio of 177, and there is titanium carbide with a modulus of 55,000,000 psi and a modulus-to-density ratio which is nearly three times that of aluminum. Finally there is beryllium, included here primarily for completeness to show that a high modulus-to-density ratio is not contrary to nature, for even if beryllium should become available in quantity its poisonous characteristics might preclude its use.

The carbides are becoming available in somewhat bigger pieces. Possibly carbides should be considered as presently applicable to such things as thin wings for very small missiles or to small wind-tunnel models for which stiffness is the primary requisite, but even for such applications only if adequate allowance for the limitations of the carbides such as the fact that they are very brittle can be made. Further study of their limitations is proceeding, and the Kennametal Corporation is under contract to supply us with carbide test specimens to aid in this study.

Despite such limitations as scarcity, brittleness, or toxicity, molybdenum, the carbides, and beryllium do show that a high modulus-to-density ratio is not contrary to nature. Since a high modulus-to-density ratio is not contrary to nature, is there any possibility of improvement in the modulus-to-density ratio of common materials? Most authorities are of the opinion that there is no possibility of improvement in either modulus or modulus-to-density ratio. There are, however, a few dissenters. The chief dissenters are Köster in Germany (reference 6) and Dudzinski in Great Britain (references 7 and 8), but there have also been a few investigators in this country (references 9 to 11) who have suggested that Young's modulus is susceptible to manipulation by alloying in much the same way that other mechanical properties of metals can be manipulated. Dudzinski has suggested that the modulus-to-density ratio as well can be improved.

Because this statement is a somewhat controversial one, let us review some of the data on which it is based. First consider the data based on Köster's work, presented by Zener as evidence that small amounts of alloying elements which form solid solutions may be expected to decrease the modulus. These data are reproduced in figure 9 which shows the

effect on Young's modulus of solid solutions of aluminum, manganese, beryllium, and magnesium in copper. Notice particularly that both manganese and beryllium decrease the modulus when alloyed with copper, even though their moduli individually - given by the numbers in brackets - are both greater than that of copper. The fact that the modulus of the alloy is not simply the weighted average of the moduli of the elements suggests the possibility that for some combinations improvements might be realized. Actually, just a little farther along the curve for aluminum alloyed with copper, beyond the point at which simple solid solutions are formed, the modulus increases to a value substantially higher than that for either aluminum or copper alone, as shown in figure 10. This plot is also based on Köster's work. Here again is shown the effect on Young's modulus, this time for various percentages of aluminum alloyed with copper. Finally, let us look at possible variations in the modulus-to-density ratio (fig. 11). Here the data are derived from Dudzinski's work in which he shows how the modulus-to-density ratio of aluminum may be changed by adding alloying elements. Dudzinski has gone so far as to state that he believes a practical aluminum-alloy with a Young's modulus of 12,000,000 psi can be developed. This prediction, depending as it does upon the interpretation of the word "practical", does not seem so extravagant when it is considered that the Aluminum Company of America lists its alloy 32S as having a Young's modulus of 11,500,000 psi.

Despite data such as these, the prevailing impression seems to be that there is no hope of improvement in the modulus-to-density ratio. In fact the possibility has been suggested that Köster's and Dudzinski's data may be drastically in error.

In an effort to help clarify this situation, Langley requested the Aluminum Company of America to make some aluminum-alloy sheet having a Young's modulus of 12,000,000 psi and a density approximately the same as that of pure aluminum. The Aluminum Company of America assured us that the sheet could be made but that it would be a far cry from the practical alloy that Dudzinski was trying to develop. That is unquestionably how it turned out because among other things, the material is very brittle. Undeniable, however, as the stress-strain curves given in figure 12 show, by adding alloying elements to pure aluminum they have both

(1) Increased the mechanical properties

(2) Increased the Young's modulus

They did not quite achieve the 12,000,000 they were shooting for in the with-grain direction but they exceeded it in the cross-grain direction. However, since the average elongation in the with-grain

direction was between 2 and 3 percent over a 2-inch-gage length, at the same time that they were raising the modulus, they were also increasing the brittleness.

At present it appears that most high modulus-to-density-ratio materials are brittle. The problem that evidently must be solved if higher modulus-to-density-ratio structural materials are to be achieved appears to be that of providing ductility. Whether this goal can be achieved is still a matter for speculation.

CONCLUDING REMARKS

Taken as a whole, the problem of designing aircraft structures for stiffness as well as strength should be considered to be in its infancy, and so considered it seems to be a healthy infant. It is a problem that promises to grow in importance, and its future certainly does not appear hopeless. Integrally stiffened construction, new materials, and new combinations of materials all offer possibilities and certainly in time at least some of the possibilities will be realized.

REFERENCES

1. Sandorff, Paul, and Papen, G. W.: Integrally Stiffened Structures. Aero. Eng. Rev., vol. 9, no. 2, Feb. 1950, pp. 30-38.

2. English, J. B.: The Development of Rolled Integrally Stiffened Sheet of Aluminum Alloys. Reynolds Metals Co., Sponsored by U. S. Air Force, Air Materiel Command, June 1950.

3. Wolfe, K. B., Pipitone, S. J., and Motherwell, G. W.: Significant Structural Design and Fabrication Developments. Preprint No. 378, Paper presented before SAE Meeting (Los Angeles), Oct. 5-8, 1949.

4. Dow, Norris F., and Hickman, William A.: Structural Evaluation of an Extruded Magnesium-Alloy T-Stiffened Panel. NACA TN 1518, 1948.

5. Siegel, Sidney: Modern Composite Metals. Reprint, Jour. Metals, July 1950.

6. Köster, Werner, and Rauscher, Walter: Beziehungen zwischen dem Elastizitätsmodul von Zweistofflegierungen und ihrem Aufbau. Z.f. Metallkunde, vol. 39, 1948, pp. 11-120.

7. Dudzinski, N., Murray, J. R., Mott, B. W., and Chalmers, B.: The Young's Modulus of Some Aluminium Alloys. Rep. No. Met. 10, British R.A.E., July 1946.

8. Dudzinski, N.: The Young's Modulus of Some Aluminium Alloys. Part II. Rep. No. Met. 36, British R.A.E., Sept. 1948.

9. Templin, R. L., and Paul, D. A.: Modulus of Elasticity of Aluminum Alloys. Tech. Pub. No. 366, Am. Inst. Mining and Metallurgical Eng., Sept. 1930.

10. Zener, Clarence: Relation between Residual Strain Energy and Elastic Moduli. Acta Crystallographica, vol. 2, pt. 3, June 1949, pp. 163-166.

11. Dorn, John E., and Tietz, Thomas E.: The Modulus of Elasticity - A Review of Metallurgical Factors. Metal Progress, vol. 58, no. 1, July 1950, pp. 81-84.
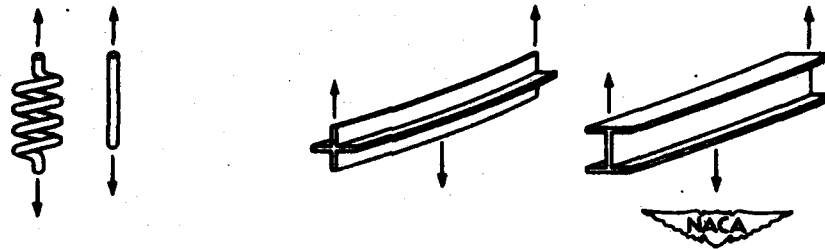
Figure 1.- Tension and bending members designed for low and high stiffnesses.
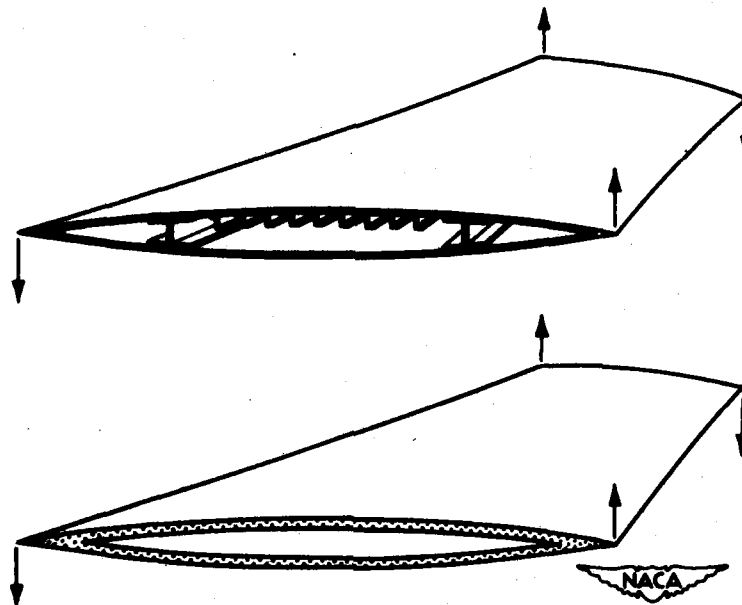
Figure 2.- Wings designed for low and high torsional stiffnesses.
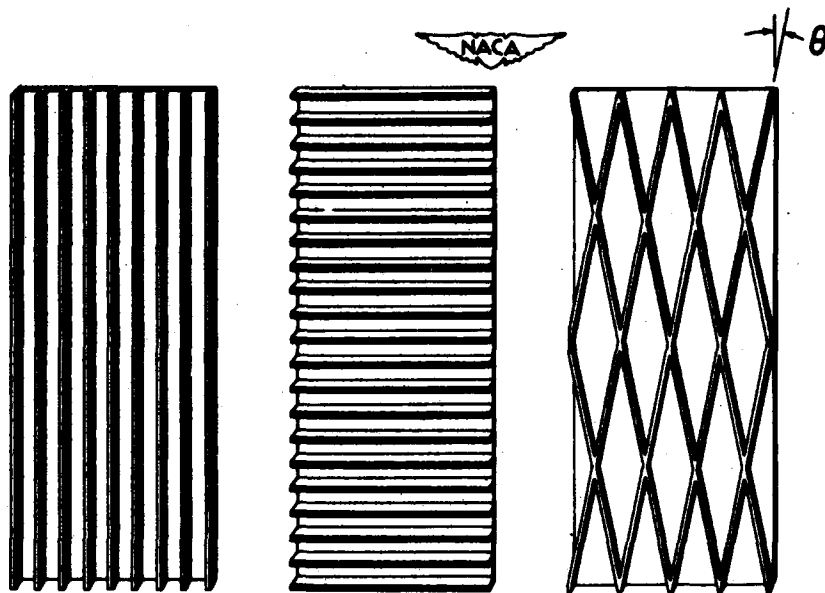
Figure 3.- Configurations of integrally stiffened sheet considered.
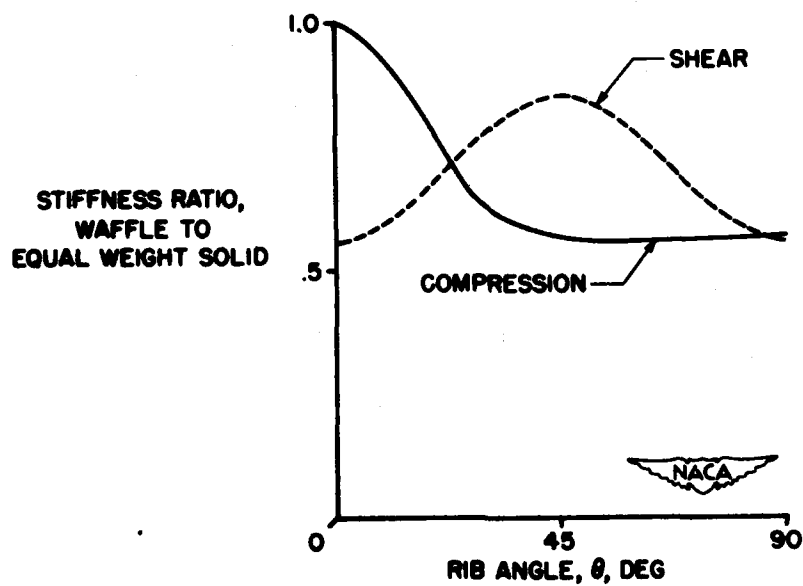
Figure 4.- Compressive and shear stiffnesses of waffles.

12
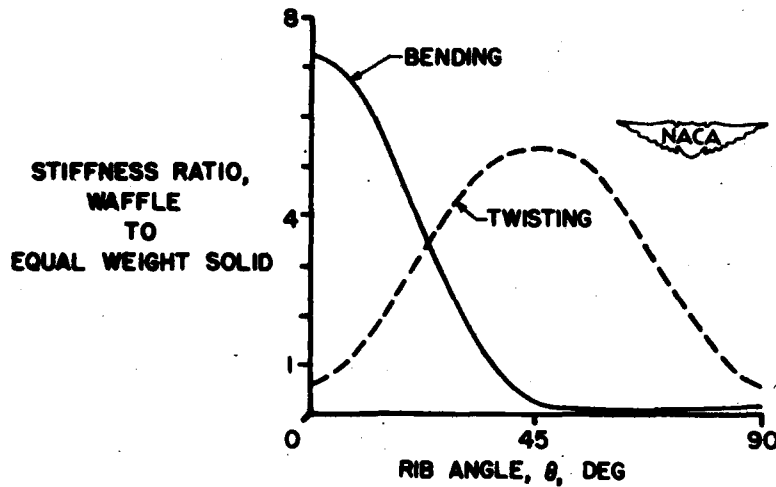
Figure 5.- Bending and twisting stiffnesses of waffles.
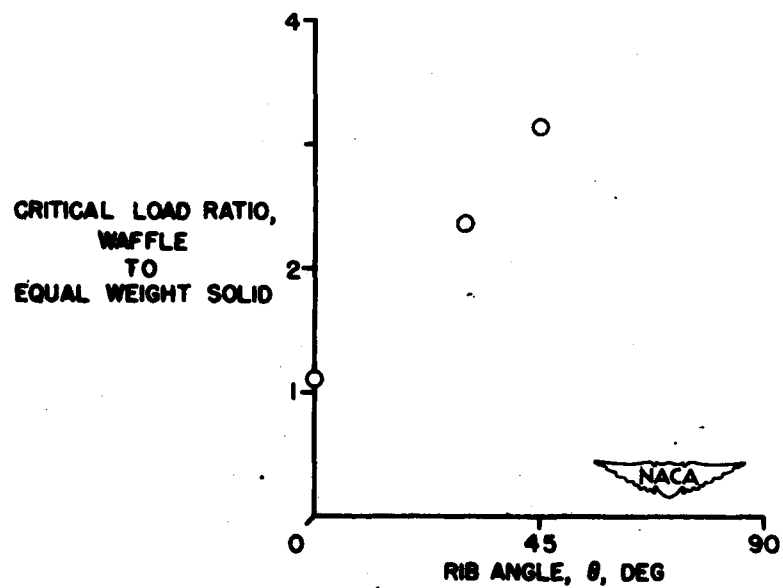
Figure 6.- Experimental buckling loads for waffles.
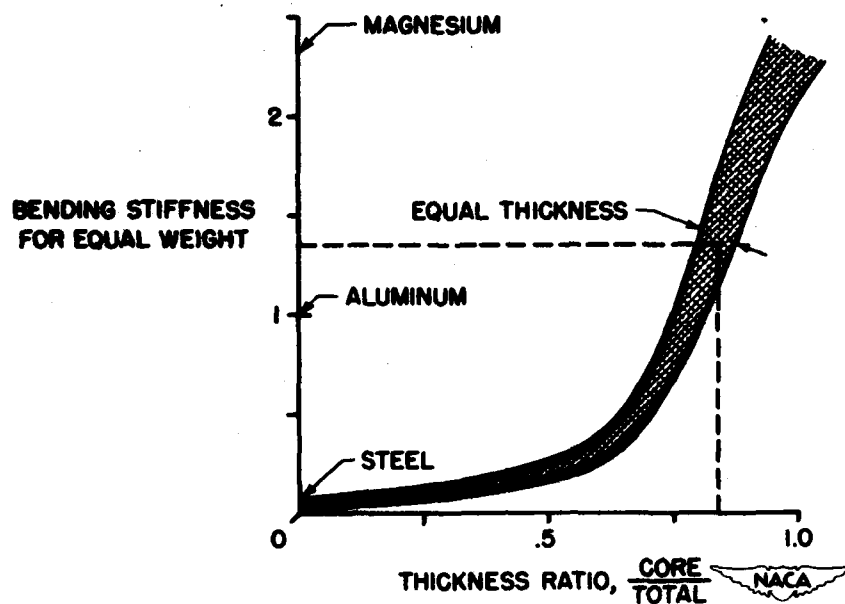
Figure 7.- Bending stiffnesses of steel-clad magnesium sandwiches.
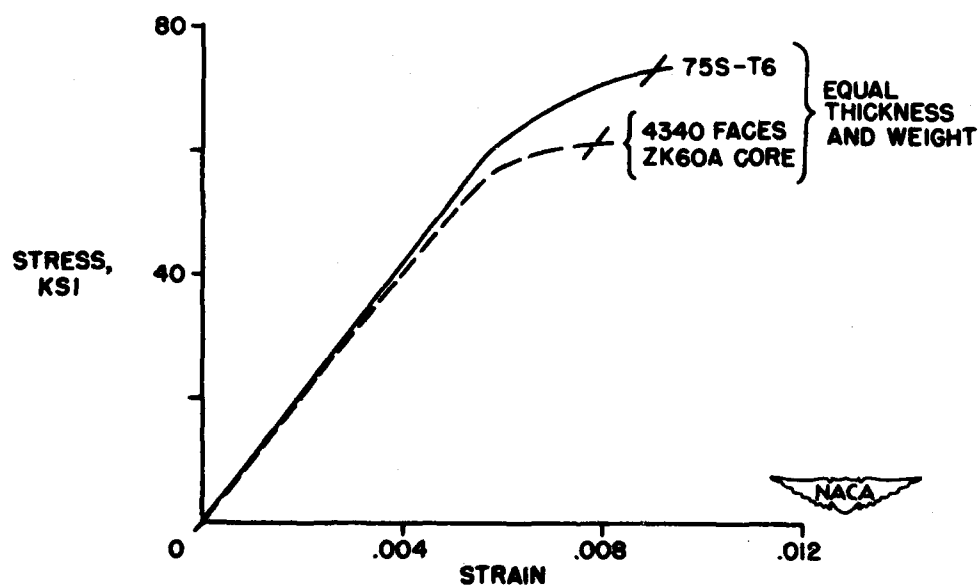
Figure 8.- Calculated stress-strain curve for steel-clad magnesium sandwich.

BINARY ALLOYS OF COPPER
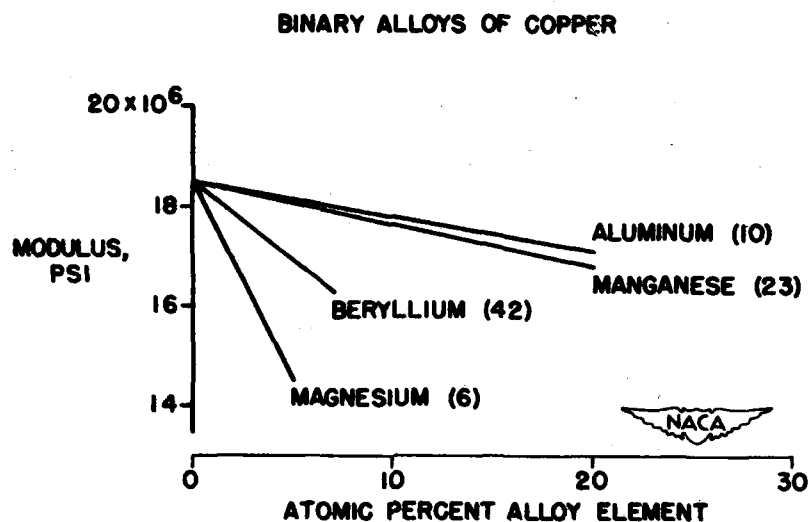
Figure 9.- Effect on modulus of adding alloying elements in solid solution with copper.
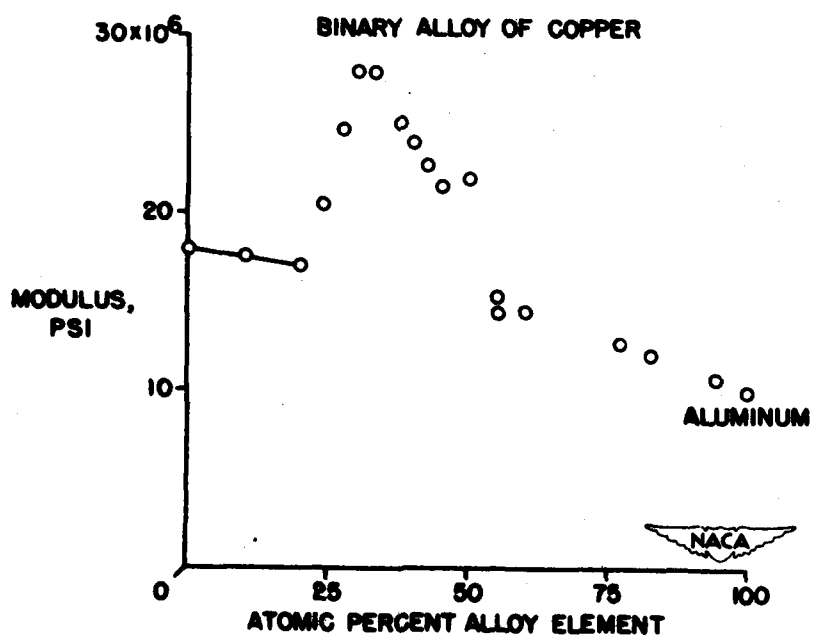
Figure 10.- Effect on modulus of alloying aluminum with copper.

BINARY ALLOYS OF ALUMINUM
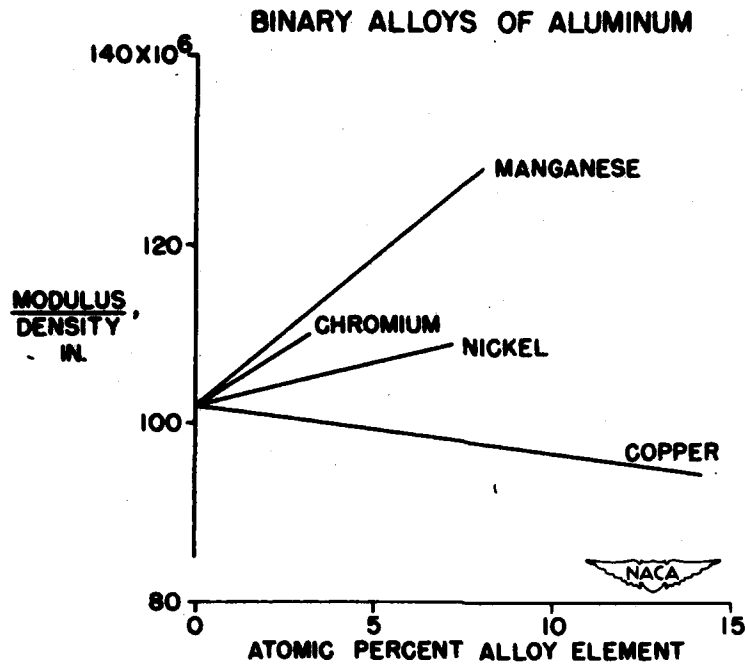
Figure 11.- Effect on modulus-to-density ratio of adding
alloying elements to aluminum.
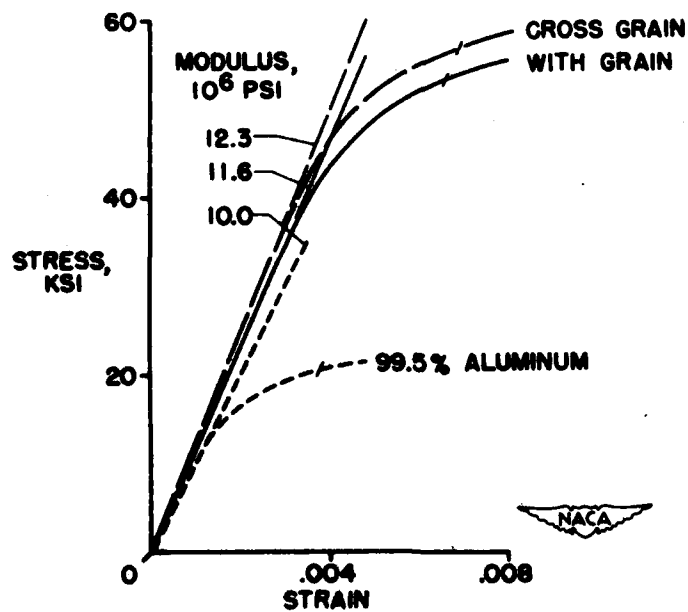
Figure 12.- Stress-strain curves for special high modulus
aluminum alloy.

PLASTICITY

THEORIES OF PLASTICITY

By S. B. Batdorf and Bernard Budiansky

Langley Aeronautical Laboratory

Before the occurrence of structural failure, plastic flow usually develops. This plastic flow reduces the stiffness of the material, changes the stress distribution, gives rise to residual stresses, and produces permanent distortions. In addition, it plays a role in the fracture of ductile materials and probably is involved also in creep and fatigue. A portion of our research effort has therefore been devoted to the development of an adequate understanding of plasticity. Although this goal has not yet been achieved, it is felt that substantial progress has been made, and this paper will constitute a report on our activities in this field. As such it will be primarily an account of a search for an acceptable theory. Practical applications will be the concern of the next paper.

The general character of the stress-strain behavior of materials in simple tension or compression has been known for a long time and this has permitted adequate solutions to be found for the stress distribution, buckling loads, and maximum strength of beams and columns. The solution of the corresponding problems for plates and shells such as go to make up the bulk of the airframe, however, requires a knowledge of the plastic strain laws for arbitrarily varying combined-stress loading conditions, and just what form these laws should take has not as yet been established.

Figure 1 shows a plot of a typical stress-strain curve for a strain hardening material in simple tension. There are two equations in general use for describing the stress-strain relations beyond the elastic range of the material. One of these, $\sigma = E_S \epsilon$, relates the total stress to strain by means of a reduced modulus called the secant modulus which is defined in the figure. The other, $d\sigma = E_T d\epsilon$, relates increment of stress to increment of strain by using the slope of the curve or the tangent modulus. When these laws are generalized for application to combined-stress loading conditions, they retain their character of having either finite or incremental form. The generalization of the finite one has been guided in part by the form of the elastic equations for three-dimensional states of stress, while the generalization of the incremental one has been influenced by the equations for fluid flow. Although the two types of law are equivalent in the case of simple tension, in their general formulations they are not. One of the most conspicuous differences is that finite laws imply that stress and strain are uniquely associated, whereas according to incremental theories the relation between stress and strain depends upon the loading path, or stress history.

Analyses based on plastic stress-strain laws are much more complicated than those based on elastic laws because, although the equations of elasticity are linear, those of plasticity are nonlinear. Of the two types of plastic stress-strain law, however, the finite law is much easier to use because with it the stress distribution can be obtained directly in terms of the final load. The incremental law, on the other hand, requires that once plastic action has started the stress distribution must be found for each increment of load, this process being continued until the final load is reached. One would therefore prefer to use the finite type of stress-strain law. More important, however, is the question of which is right. Both types of equation can be written with adjustable parameters which can be so chosen as to agree with experimental results for proportional loading - that is, loading in which all stress components increase at the same rate. When this is done, however, the two types of law will disagree as to the stress-strain relationships for all other types of loading and the disagreement is sharpest, generally speaking, when the loading deviates the most strongly from proportional loading. One of the cases in which the loading departs strongly from proportionality is that of buckling. So let us now see what kind of results are obtained here from the two types of theory.

During the war, an extensive series of tests on plastic buckling of plates was conducted at the Langley Laboratory. On the basis of these and other data, Gerard, then of the Republic Aviation Company, proposed the secant modulus as the effective modulus for plate buckling (reference 1). (The same proposal was made independently by McDonald of Dow Chemical Company.) Shortly after this, Handelman and Prager of Brown University gave a theoretical solution to the problem of plastic buckling of plates on the basis of the incremental theory of plasticity (reference 2) and Stowell of Langley solved it on the basis of the finite theory of plasticity (reference 3). (Incidentally, both solutions had been obtained by Bijlaard in 1938, but his work was not generally known in this country; a review of his work appears in reference 4.) In figure 2 the results of the two theories are compared with experimental data on the buckling of long hinged flanges. In this figure buckling stress is plotted against the elastic buckling strain. The ratio of the heights of the buckling curve and the elastic line may be regarded as a knock-down factor to be used above the elastic limit. At higher stresses the finite theory says there is a knock-down factor and the incremental theory says there is not. In fact, in this particular case the finite theory predicts a curve coinciding with the stress-strain curve for the material, which means the secant modulus applies. Test data obtained from extruded cruciform section columns that buckled by twisting are in good agreement with the finite theory. (A cruciform column is equivalent to four flanges with a common hinge line).

Figure 3 shows similar results for simply supported plates buckling in compression. Square tubes were used as test specimens. The dotted curve is the incremental-theory result computed by Handelman and Prager. Although it is reduced below the elastic value at high values of stress, it is not reduced nearly enough. The finite-theory result falls below the stress-strain curve in this case and is again in good agreement with experiment.

These comparisons tend to confirm the finite type of law for plasticity and rule out the incremental type. However, many plasticity experts reject the finite type of law in favor of the incremental type and it may now be of interest to inquire into the reasons for this.

There is first of all a theoretical objection to finite laws based on continuity considerations (fig. 4). The closed curve in figure 4 represents the original elastic limit of a material being subjected to compression and shear. This means that starting from stress O no plastic action occurs as long as the combinations of shear and compression stays inside the closed curve. If now a material is loaded in pure compression up to point A beyond the original elastic limit, then the new elastic limit in compression is A and the dotted curve indicates the supposed location of the new elastic boundary. If an increment of stress is then added, bringing the stress to the state represented by point B in the plastic region, the finite theory predicts that an increment of plastic shear strain $d\gamma^P$ will be produced, given approximately by the formula

$$d\gamma^P = \frac{d\tau}{G}\left(\frac{E}{E_S} - 1\right)$$

where $d\tau$ is the increment of shear stress and G is the elastic shear modulus. If the increment of stress is such as to bring the material to the state represented by point C in the elastic range, no plastic action is involved so the plastic shear strain is zero. One would expect on continuity considerations that, as B and C are brought closer together until they actually converge on the boundary, the same answer would be obtained whether we used B or C. This, however, does not occur according to the finite theory of plasticity. Incremental theories of the types that have been considered up to the present are free from this discontinuity in behavior because according to these theories the plastic shear strains associated with AB and AC are both zero.

As a matter of fact, it is just this difference between the two theories which is responsible for the success of the finite type of theory in accounting for the buckling of long hinged flanges, because these are, for practical purposes, columns which fail by twisting and the buckling stress of these flanges is determined almost entirely by the

effective shear modulus. The plastic shear strain associated in the finite theory with stress change AB, which was considered theoretically objectionable, gives us the knock-down factor needed to produce agreement between theory and experiment for buckling.

At this point it was decided to investigate the problem of the shear stiffness of a plastically compressed material by direct experiment. A forged billet of 14S-T4 aluminum alloy was machined into a thin cylinder which was then compressed into the plastic region and then twisted, with the compressive stress held constant. It turned out that the initial modulus at the beginning of twisting was substantially the elastic modulus as predicted by the incremental theories and in contradiction to the finite theories.

This posed quite a dilemma. The finite type of theory was in good agreement with plastic-buckling experiments, but disagreed with direct tests under controlled loading conditions using cylinders. The incremental type of theory on the other hand was in good agreement with the cylinder tests but in disagreement with buckling experiments. There appear to be three possible explanations for this situation: (1) Incremental type theories might be right, but the measured buckling stresses might be far below the theoretical because of the eccentricities in the specimens; (2) the Handelman and Prager results for incremental theory were obtained before Shanley's concept of plastic buckling developing with increasing load was generally accepted and did not incorporate this principle, whereas the results shown for finite theory do incorporate it; and (3) it is possible that neither type of plasticity theory is right since each of them appears to disagree with a certain class of experiments. Let us now examine each of these possibilities.

It can be noted in figure 2 that the buckling stress of long hinged flanges falls in a relatively small scatter band. One would expect that if initial eccentricity were responsible for the discrepancy, the scatter band would be wide, with at least a few points close to the theoretical value. This makes it appear quite unlikely that initial eccentricities are responsible for the discrepancy between the experimental results and the predictions of the incremental theory. Besides, there is another explanation for the scatter. Coupons cut from different parts of the cross section were found to have slightly different yield strengths. If the highest and lowest theoretical curves corresponding to these variations in yield stress are plotted here on the basis of finite theory, the experimental points are all included within the two limiting curves, which are shown dashed in figure 2.

The second possibility was that the error in the incremental-theory solution is due to the neglect of the Shanley principle. But incorporation of the Shanley principle will make no change so far as long-hinged-flange results are concerned. The reason for this is that

the buckling stress of a long hinged flange is determined by shear stiffness alone, and according to incremental theory the effective modulus in shear of a plastically compressed material is the elastic value whether the material continues to load in compression or not. In the case of the simply supported plate the incorporation of the Shanley principle in the buckling calculation does change the results but not enough to bring the theory into good agreement with the experiment. However, to clinch the matter, an experiment was conducted in which a simply supported plate was annealed in order to give it a very low buckling stress. The results are shown in figure 5 in which all theoretical curves incorporate the Shanley principle. The curves up near the top show the results before annealing. The test data are in excellent agreement with finite theory but also in fair agreement with incremental theory. The bottom curves show the results after annealing. The test data are still in fairly satisfactory agreement with finite theory, but disagree seriously with the incremental theory. Also, the scatter is so very small in relation to the large discrepancy that it can hardly be seriously supposed that the discrepancy is due to initial eccentricities. In further support of this view, there is the fact that light would not pass between a straight edge and the specimen below the buckling load.

If one concludes that laws of the incremental type are wrong for buckling and that finite laws are wrong for a right-angle loading path, then one is in the uncomfortable position of having no generally reliable theory of plasticity on the basis of which to make structural analyses. In an effort to remedy this situation, a fresh start has been made and a theory has been developed for the stress-strain relationships in the plastic range on a new basis (reference 5). As was mentioned before, finite and incremental theories in their simpler forms can be considered to be patterned after the laws of elastic solids and viscous liquids, which are treated as uniform homogeneous mediums. In reference 5 a metal was considered to be an inhomogeneous medium, specifically a polycrystal composed of a large number of randomly oriented grains. Plastic deformation was considered to be due to slip in those grains for which slip planes were most highly stressed in shear. The resulting theory is a little like the kinetic theory of gases in that the macroscopic quantities that are of interest for engineering purposes are obtained by summing the contributions of a large number of elementary physical processes.

This theory has been applied to proportional loading of cylinders in biaxial tension and found to be in excellent agreement with experiment (reference 6). All proposed plastic laws are reasonably adequate when applied to proportional loading, however, and our principal concern must be how the theory works out when the stress ratios vary during the loading. Before discussing this problem, some fundamental

differences between this and previous types of plasticity theory must be explained.

Figure 6 shows a schematic representation of the elastic-plastic boundary of a material loaded in compression and shear according to conventional theory and according to what will be called herein the slip theory. The solid ellipse is in each case the original elastic limit of a material without strain hardening. Suppose the material is loaded in compression to the state A. As a result of this loading, conventional theories contemplate a new elastic boundary something like the dashed line which separates the region of loading from the region of unloading. In the region of loading the plastic stress-strain law applies, which is of either finite or incremental type. According to slip theory, when the material is loaded to point A there are three regions: Regions (1) and (2) correspond to continued plastic deformation, while region (3) is the new elastic region corresponding to the unloading region. A small stress AB in region (1) induces plastic deformation in only those grains of the material which already experienced plastic deformation while going from 0 to A, so that all plastically loaded grains continue loading or at least do not unload. The equations of the slip theory imply that a finite stress-strain law should be valid in this region. In region (2) some plastically deformed grains are loading and some are unloading. In this region the slip theory is equivalent to a mixture of finite and incremental types of theory, being mainly finite at the upper end and mainly incremental at the lower end.

As a result of this transition, in some respect slip theory agrees with finite theory, in others with incremental theory, while in still other respects it agrees with neither one. For example, according to finite theory, the plastic strain in the stress state A is independent of the loading path. According to incremental theories the plastic strain depends on the loading path, and in particular a loading path which is always on the right-hand side of the compression axis would lead to a different strain from a loading path which is always on the left. According to the slip theory the strain at point A is independent of the loading path provided the loading path stays within region (3) but will depend on loading path if any part of it traverses region (2). As a second example, let us consider the initial shear stiffness at stress A associated with stress increment AB. According to finite theory this is below the elastic value by an amount which depends on point A, but not on the slope of the line AB, provided AB points upwards or corresponds to continued loading. The incremental theory gives the elastic modulus G under all circumstances. The slip theory agrees with the finite theory in region (1), with the incremental theory in region (3), and makes a transition between these results in region (2).

This particular feature of the slip theory suggests a possible explanation of the dilemma encountered earlier in this paper. According to the Shanley principle, plastic buckling can be expected to occur with increasing load. One may expect the corresponding stress increment to lie in region (1), so that the stiffness and, therefore, the buckling stresses are those predicted by the finite laws of plasticity. The experiments on plastic cylinders, however, were carried out in region (2) in which, according to slip theory, the predictions of the finite laws are no longer valid.

This suggested explanation has been subjected to direct test in some further experiments performed at the Langley Laboratory. A group of cylinders were compressed to point A and then while the compressive load continued to increase they were loaded in torsion. In this way stress-strain data were taken with the stress increment AB having a number of different slopes, some in region (2) and some in region (1). The instrumentation was carefully worked over to get maximum sensitivity in order to get a good measurement of the effective shear stiffness at the very beginning of twisting. It was found that the initial shear stiffness was the elastic value G for all cases in region (2) and also for a case near the border here in region (1). In the case of the very steepest stress increment, a rather remarkable thing happened; the effective shear stiffness was the elastic value for the first 50 or 100 pounds per square inch of applied shear stress and then very rapidly dropped off to the reduced value predicted by finite theory. This suggests that the slip theory may be qualitatively correct about the effective shear stiffness but that quantitatively it leaves something to be desired.

The slip theory has also been tested by investigating the validity of its fundamental physical assumptions by observing a polished and etched specimen of aluminum under a microscope during tensile testing. This study confirmed some of the basic concepts of the theory and suggests that others may need refinement if accurate results are to be obtained.

Summing up what has been said about theories, one may say that finite theories are not satisfactory when very abrupt changes occur in the loading path such as the right-angle turns investigated in the plastic-cylinder experiments. Because of this many experts have tended to reject finite theories in favor of incremental theories except for proportional loading where the two types of theory agree. However, incremental theories of the types proposed up to this time are unsatisfactory for buckling. A new type of theory based on a physical model of a plastically deforming metal suggests that finite and incremental theories each contain limited range of application. There are some prospects that the new approach might lead to the generally valid formulation of stress-strain laws in the plastic range that is at present lacking. But this would require some refinements in the theory and we cannot be sure that

they can be successfully incorporated. In the meantime it appears that there is now theoretical as well as experimental justification for using a finite law in a wider variety of problems than has been generally conceded up to now, which is very fortunate since this is the simplest type of law to use in a structural analysis.

REFERENCES

1. Gerard, George: Secant Modulus Method for Determining Plate Instability above the Proportional Limit. Jour. Aero. Sci., vol. 13, no. 1, Jan. 1946, pp. 38-44 and 48.

2. Handelman, G. H., and Prager, W.: Plastic Buckling of a Rectangular Plate under Edge Thrusts. NACA Rep. 946, 1949. (Formerly NACA TN 1530).

3. Stowell, Elbridge Z.: A Unified Theory of Plastic Buckling of Columns and Plates. NACA Rep. 898, 1948. (Formerly NACA TN 1556.)

4. Bijlaard, P. P.: Theory and Tests on the Plastic Stability of Plates and Shells. Jour. Aero. Sci., vol. 16, no. 9, Sept. 1949, pp. 529-541.

5. Batdorf, S. B., and Budiansky, Bernard: A Mathematical Theory of Plasticity Based on the Concept of Slip. NACA TN 1871, 1949.

6. Batdorf, S. B.: The Interpretation of Biaxial-Tension Experiments Involving Constant Stress Ratios. NACA TN 2029, 1950.

Figure 1.- Stress-strain curve for simple tension.
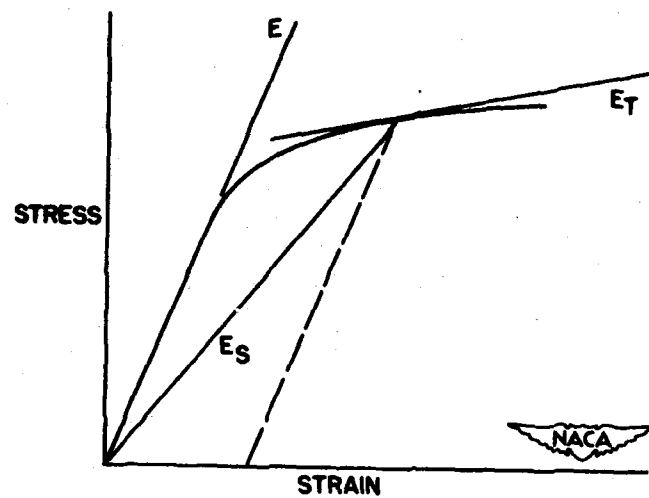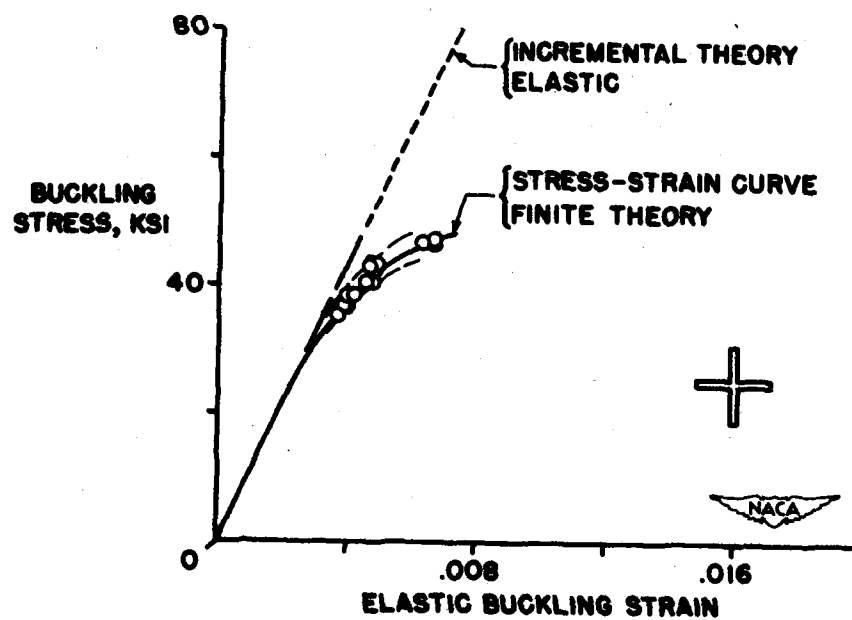

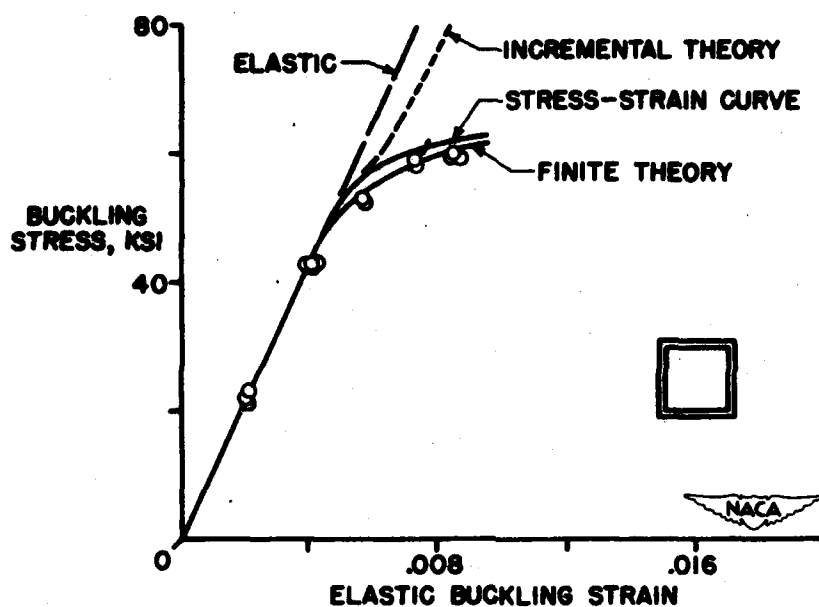Figure 2.- Buckling stresses of long hinged flanges.

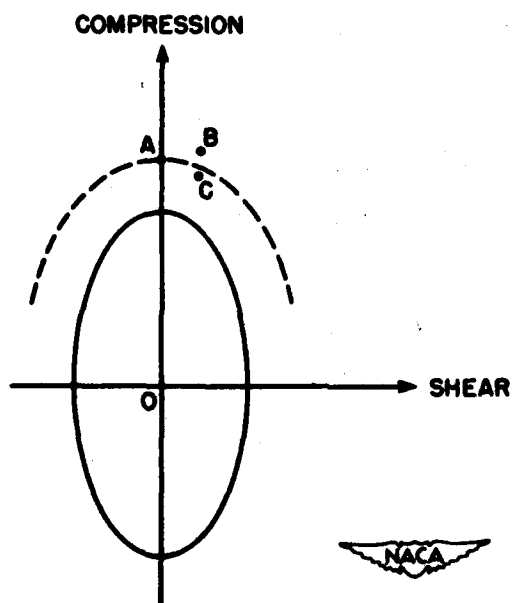Figure 3.- Buckling stresses of square simply supported plates.

Figure 4.- Loading and unloading in finite and incremental theories.
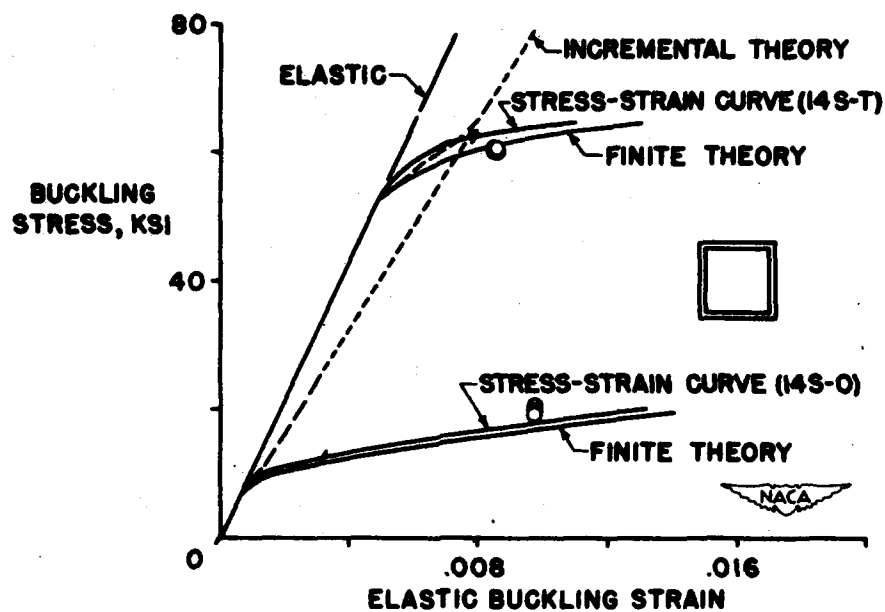
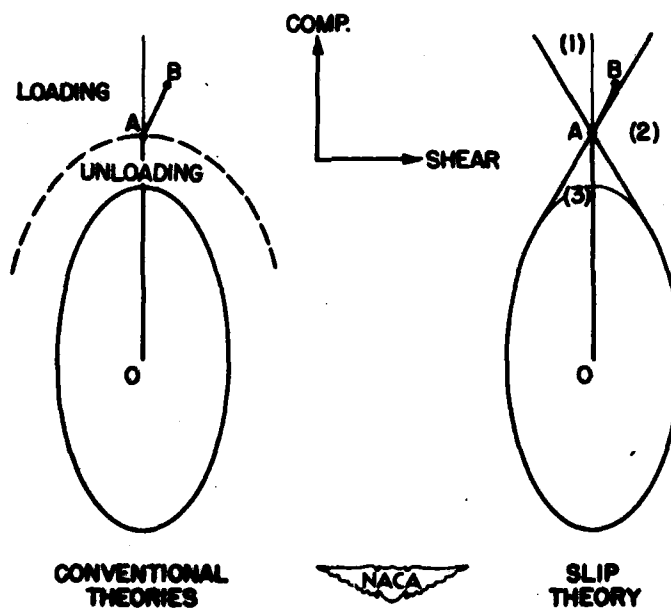Figure 5.- Buckling of heat–treated and of annealed 14S aluminum-alloy plates.

Figure 6.- Comparison of slip and conventional theories with respect to elastic and plastic regions.

SOME APPLICATIONS OF PLASTICITY TO STRUCTURAL ANALYSIS

By Elbridge Z. Stowell, George E. Griffith,
George J. Heimerl, and John E. Duberg

Langley Aeronautical Laboratory

Three applications of plasticity theory are discussed: the first concerns stress distribution, the second concerns maximum strength, and the third is concerned with the selection of efficient materials.

Stress distribution.- It is well known from both theory and experiment that stresses are increased by the presence of a hole or notch. In case of a circular hole in a wide plate under tension, the stresses are undisturbed some distance away from the hole but increase rapidly as the edge of the hole is approached, finally reaching a value three times as large as the stress applied to the sheet (fig. 1 and reference 1). It has been known for a long time that this stress concentration factor of 3 is reduced in the plastic range of the material, but just what numerical value it takes at any applied stress level and what the stress distribution is have not been known. Experiments have been conducted here on 24S-T3 aluminum-alloy sheet to help throw light on these questions (fig. 2 and reference 2). As the stress level increases so that the material at the edge of the hole becomes plastic, the stress peak rounds off and the stress concentration diminishes.

An approximate theoretical solution has been obtained by using plasticity theory for the stress distribution in this case by using a finite stress-strain law (reference 3). One or two radii from the edge of the hole the theory is not in too good agreement with experiment, but a long way from the hole and right at the edge, where the stress is of greatest interest, the agreement is very close. Figure 3 shows a plot of stress concentration factor as a function of applied stress far removed from the hole. The factor remains 3 until the stress at the hole reaches the elastic limit. As the applied stress increases, the stress concentration factor drops off toward unity.

Fortunately the theory gives a very simple formula for the stress concentration factor for a circular hole, namely

$$1 + 2 \frac{E_s}{E_\infty}$$

In this formula E_s is the secant modulus corresponding to the stress at the edge of the hole and E_∞ is the secant modulus at the applied

stress. At sufficiently low stresses, both of these moduli are equal to the elastic modulus so that the well-known value of 3 is obtained in the elastic range of the material. By use of this formula, stress concentration factors for materials other than 24S-T3 can be found if the stress-strain curve for the material is known.

The above formula for a circular hole can be generalized in a rather natural way in order to apply it to other types of stress raiser, as follows:

$$1 + \left(K_T - 1\right)\frac{E_S}{E_\infty}$$

where K_T is the stress concentration factor obtained in the usual way from the theory of elasticity. A test has been made of this formula by experiments on large sheets, 4 feet by 12 feet, of 24S-T3 material with semicircular notches and fillets (fig. 4). The plot, which is similar to that of figure 3, is for the sheets with the semicircular notches for which the elastic stress concentration factors were about 2, 4, and 6. The curves were computed from the generalized formula just given and the points are experimental. A plot entirely similar to this plot was obtained from the tests on the sheets with fillets.

Since a method for finding the maximum stress at the edge of a hole is available, the question may be what happens when that stress reaches the very highest stress ever reached by the stress-strain curve for the material? Will the specimen fracture? Some preliminary experiments made at Langley Laboratory indicate that this is so, at least for the light metal alloys. If further experiments confirm this result, a method for computing the fracture stress for perforated sheet for aluminum and magnesium alloys, which should be more accurate than present methods of calculation, will be available.

Maximum strength.- The second application of plasticity is to problems of maximum strength.

No discussion of this subject would be complete without mention of the subject of columns. From the point of view of the plasticity involved, the subject is much simpler than the corresponding problem in the maximum strength of plates in that it is a one-dimensional problem, whereas plates are a three-, or perhaps more accurately, a two-and-one-half-dimensional problem. Although this problem of column strength has been discussed in the literature for about fifty years, it has not been until the last few years that the mechanics of column behavior and the plasticity have been correctly combined to show the existence of a maximum load. Shanley (reference 4) was the first to point out the existence of a difference between the buckling (first

bending) load and the maximum load in 1947-48, and the results of the
calculations (reference 5) which show how much the maximum load can
exceed the tangent-modulus buckling load are shown in figure 5. The
factor by which the tangent-modulus load must be multiplied to get the
maximum load is plotted against the ratio of tangent-modulus load to
the load at the yield stress. The different curves represent different
materials as defined by the value of n in the well-known Ramberg-
Osgood formula. The maximum load is, usually, never more than a few
percent above the buckling load.

In the case of a plate, the maximum load in some cases may be very
much more than the buckling load because of the additional support pro-
vided by the adjacent structure. The simplest case of a plate is that
of a long hinged flange and this case was studied first. Figure 6 .
shows the test setup; the specimen was an extruded cruciform-section
column consisting of four identical flanges mutually stabilizing each
other.

If one analyzes the buckling and post-buckling behavior of a plate
on the basis of purely elastic considerations, no maximum load is ever
reached. Figure 7 shows the curve of load carried by the flange as a
function of the rotation of the midpoint. Elastic considerations lead
to the upper curve which has no maximum. Actually, the experimental
curve (fig. 7) shows a very definite maximum so that a detailed consid-
eration of plastic effects is required to obtain a satisfactory solution
for maximum strength.

Such a detailed study has been made (reference 6) and the behavior
of the plate is found to be as indicated in figure 8. At successively
higher loads, the strain distribution across one flange will be shown
at the left of figure 8. Application of the theory of plasticity will
then give the corresponding stress distribution shown at the right of
figure 8. The significant thing to note is that, although the strain
along the hinge-line increases indefinitely as the load increases, the
corresponding stress does not; it reaches a maximum and then diminishes.
In fact, the reversal in the hinge-line stress occurs at the same time
(or very nearly so) that the load on the flange reaches a maximum. The
hinge-line stress falls off because it is given by the product of the
hinge-line strain and the effective modulus, and the effective modulus,
which depends on the shear stress as well as the compressive stress, is
decreasing more rapidly than the hinge-line strain is increasing.

The strain and stress distribution here correspond to a flange of
one particular width-thickness ratio. From a number of such solutions
for different values of the width-thickness ratio, a general curve for
the maximum strength of a flange can be drawn (fig. 9). (In the ordinate,
the critical stress has been divided by the compressive yield stress in

order to make the curve nearly independent of material.) The points represent experimental data obtained from a series of 24S-T4 cruciform section columns. An interesting feature of the calculations is that no matter what cruciform column in the series is considered, the combined-stress intensity along the hinge line was a constant, to about one percent.

A similar analysis has been carried out on the maximum strength of a square simply supported plate. It was assumed again that the strain distribution was the same as if the material remained elastic and the plastic stress-strain relations were used to compute maximum loads. Results for the plate are compared with those for the flange in figure 10. In the lower region the curves essentially coincide, with differences appearing in the upper region. Test points are shown for flanges, Z-, I-, and channel-section columns. Since the Z-, I-, and channel-sections are composed of combinations of flanges and webs, one would expect the test results to be between the curves for the flange alone and for the plate alone, and this proves to be the case. Again here, in calculating the plate curve, the stress intensity along the side edges proved to be a constant at failure.

The applications of plasticity discussed so far have been at room temperature. In order to show that the basic achievements at room temperature also apply at elevated temperatures, some test on buckling and maximum strength have been carried out. Figure 11 (taken from reference 7) shows test points corresponding to the indicated temperatures and superimposed upon the same theoretical curves of figure 10.

Selection of efficient structural material.- An interesting problem in structural design is the selection of the material which will permit the design of the structure with minimum weight. The criterion to be employed depends on the design condition - whether the structure is being designed by stiffness considerations, strength considerations, or by considerations of buckling strength - and these conditions therefore require separate treatments.

Figure 12 shows stress-strain curves for several available structural materials, including one magnesium, two aluminum, and one titanium alloy, and stainless W steel. Since stress is load per unit area, a division of stress by density will be a measure of load per unit weight. Figure 13 (taken from reference 8) shows the same stress-strain curves as in figure 12 but with stress now divided by density so that the ordinate is a measure of the efficiency with which a load is carried. In the elastic range, all the materials lie nearly on the same line; this result is a consequence of the familiar fact that all common materials have about the same ratio of Young's modulus to density. Beyond the elastic limit, differences appear.

If yield strength is the sole criterion determining design, then the most efficient material is found by choosing that material with the highest ratio of yield stress to density. This quantity is indicated by a tab on each curve and it turns out that titanium alloy is the best.

If ultimate strength is the criterion, ultimate stress-density ratios may be used in a similar manner.

If, however, stiffness is the sole criterion determining design, as aerodynamic considerations sometimes require, then the most efficient material is found by choosing that material with the highest ratio of stress to density at the permissible strain. At low values of strain there is little choice. At high values of strain there is a spread, with titanium alloy appearing to best advantage for some values of strain and 75S-T6 aluminum alloy for other values.

If buckling is the criterion determining design, the most efficient material is found by a slightly more complicated method. The ratio of buckling stress to density is plotted against an appropriate structural index. For column buckling, figure 14 shows as abscissa the column index, which is the product of the load P to be carried, the end fixity c, and the shape factor f, divided by the square of the distance L over which the load must be transmitted. With this index a single curve represents the buckling condition for any one material. On this basis, the choice again depends on the value of the index, with titanium alloy again best at high values of the index.

A similar plot for plate buckling is shown in figure 15, in which the index suitable for plates is the product of the load P to be carried and the square root of the buckling coefficient k, divided by the square of the width b of the plate. At low values of the index, magnesium alloy looks best and at higher values 75S-T6 and then titanium alloy takes over. It should perhaps be mentioned that the fact that a curve for ZK60-A is not shown for structural index of 6, for example, does not mean that a plate could not be designed for that value of the index. The curve was discontinued because higher values of the structural index would correspond to large and presumably unacceptable plastic strains, if the plate were designed to carry the load at the buckling stress. However, any point to the right of a curve represents a non-buckling condition at the corresponding stress and structural index, so that for practical purposes each of these curves may be thought of as terminating in a horizontal line which represents the highest stress for which one would be willing to design the plate.

These methods can be used to select materials for use at elevated temperatures. As mentioned previously, plate-strength research shows

that methods used at ordinary temperatures also apply at elevated
temperatures provided the stress-strain curve is known at the higher
temperatures. Comparisons similar to these can be made at elevated
temperatures provided creep is not important enough to change the picture
seriously. Figure 16 shows the results of such comparison at temper-
atures up to 800°. For tension or compression loading, titanium alloy
is best up to about 400°, with high-strength steel replacing it
above 400°. For column buckling, titanium and aluminum alloys are about
equally good up to 400°, then titanium alloy takes over up to 800°,
being finally replaced by steel farther up. For plate buckling the
materials, in succession, are magnesium alloy, aluminum alloy, titanium
alloy, and steel.

These applications of plasticity theory, which are adapted to the
use of a finite stress-strain law, show that there is no need to wait
upon the discovery of the most general stress-strain laws in order to
obtain immediately useful results to some practical problems.

REFERENCES

1. Timoshenko, S.: Theory of Elasticity. First ed., McGraw-Hill Book
   Co., Inc., 1934, p. 77.

2. Griffith, George E.: Experimental Investigation of the Effects of
   Plastic Flow in a Tension Panel with a Circular Hole. NACA TN 1705,
   1948.

3. Stowell, Elbridge Z.: Stress and Strain Concentration at a Circular
   Hole in an Infinite Plate. NACA TN 2073, 1950.

4. Shanley, F. R.: Inelastic Column Theory. Jour. Aero. Sci., vol. 14,
   no. 5, May 1947, pp. 261-267.

5. Duberg, John E., and Wilder, Thomas W., III: Inelastic Column
   Behavior. NACA TN 2267, 1951.

6. Stowell, Elbridge Z.: Compressive Strength of Flanges. NACA TN 2020,
   1950.

7. Heimerl, George J., and Roberts, William M.: Determination of Plate
   Compressive Strengths at Elevated Temperatures. NACA Rep. 960, 1950.

8. Heimerl, George J., and Barrett, Paul F.: A Structural-Efficiency
   Evaluation of Titanium at Normal and Elevated Temperatures. NACA
   TN 2269, 1951.
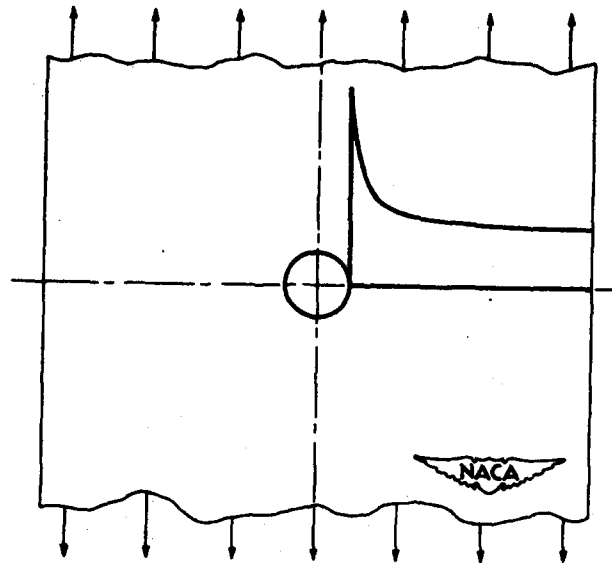
Figure 1.- Theoretical elastic-stress concentration at circular hole.
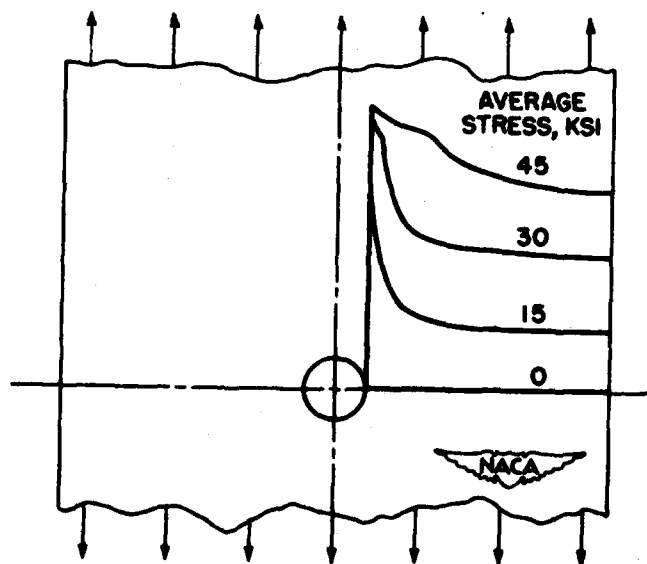
Figure 2.- Experimental stress distribution near circular hole.
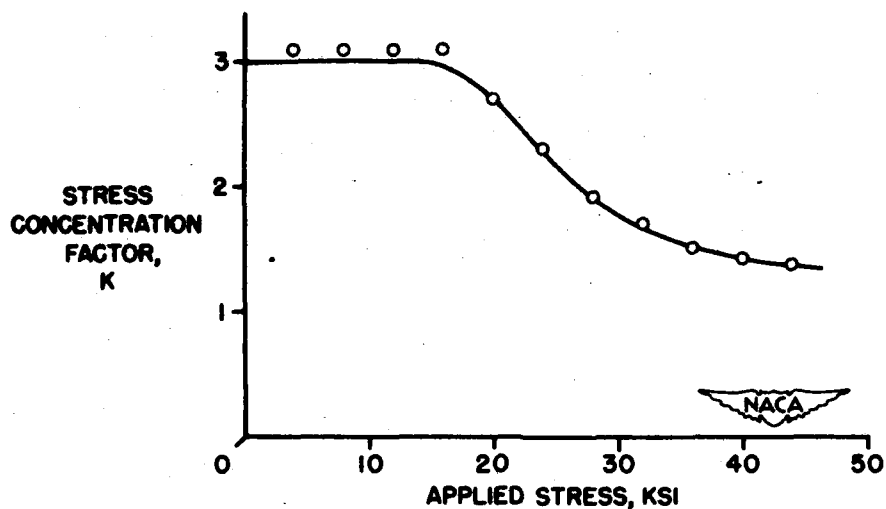
Figure 3.- Theoretical stress concentration for a circular hole,
as a function of the applied stress, compared with experiment.
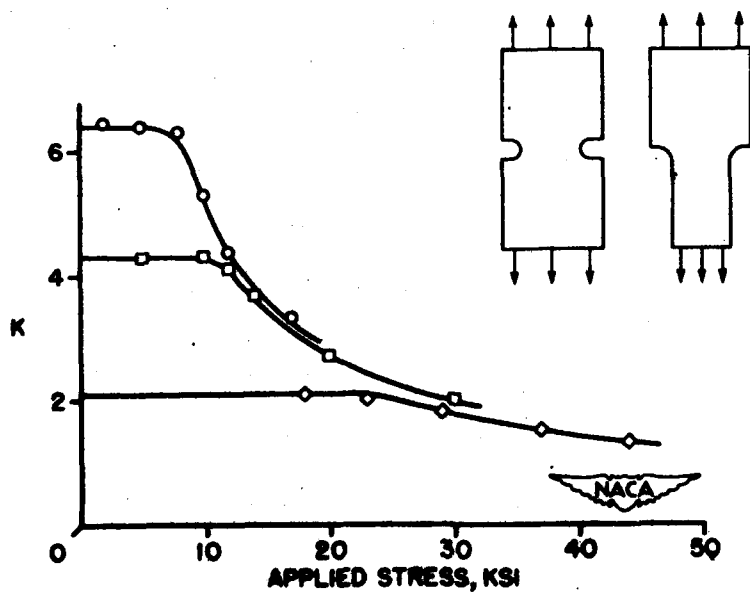
Figure 4.- Theoretical stress concentrations for semicircular
notches, as a function of the applied stress, compared with
experiment.
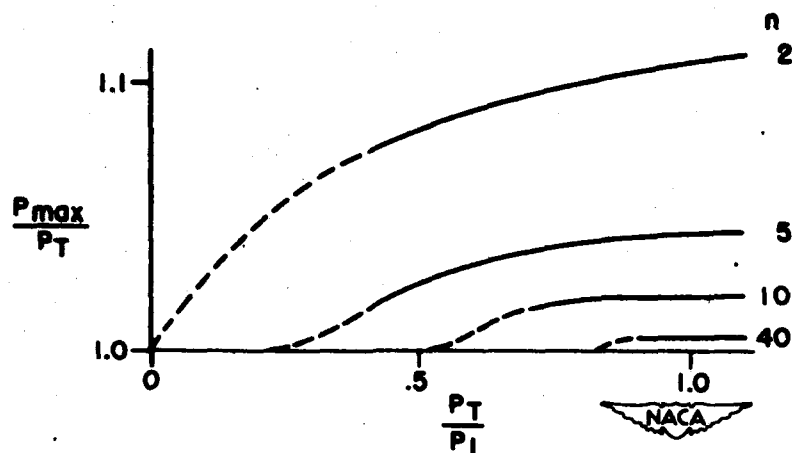
Figure 5.- Relation of maximum load for columns to tangent-
modulus load.
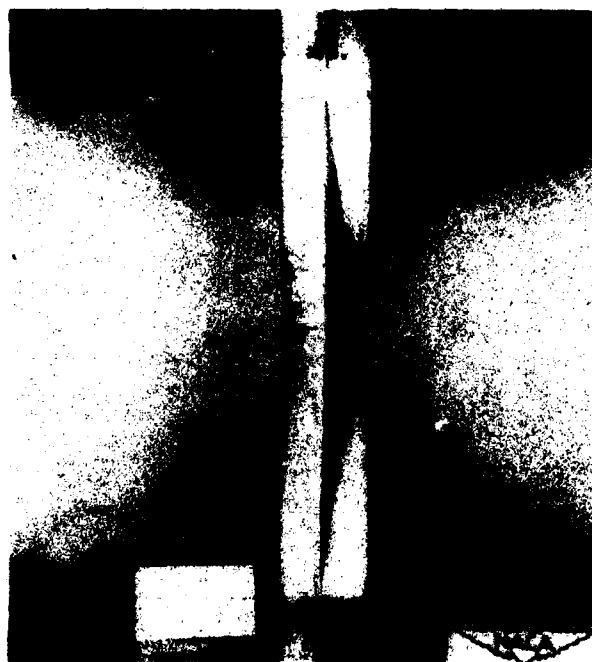
L-34925.1

Figure 6.- Cruciform-section column in testing machine.
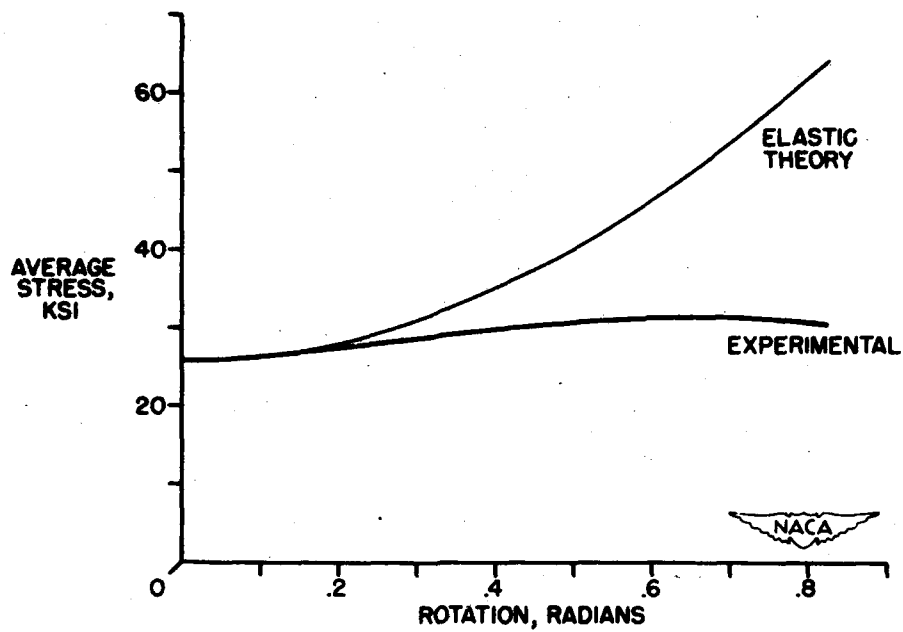
Figure 7.- Comparison of observed load on flange with that
calculated on the basis of elastic theory.
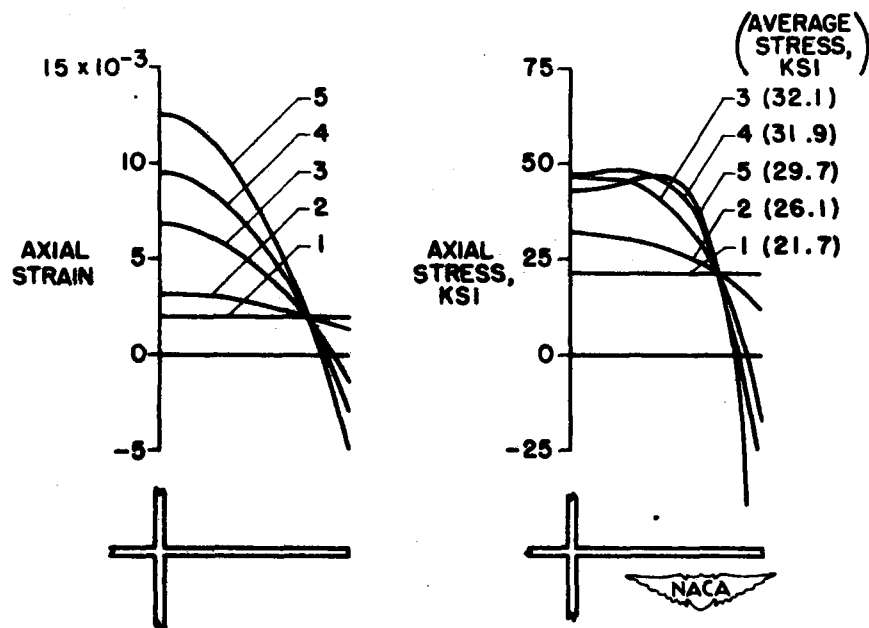
Figure 8.- Stress and strain distribution across a flange beyond
the buckling load.
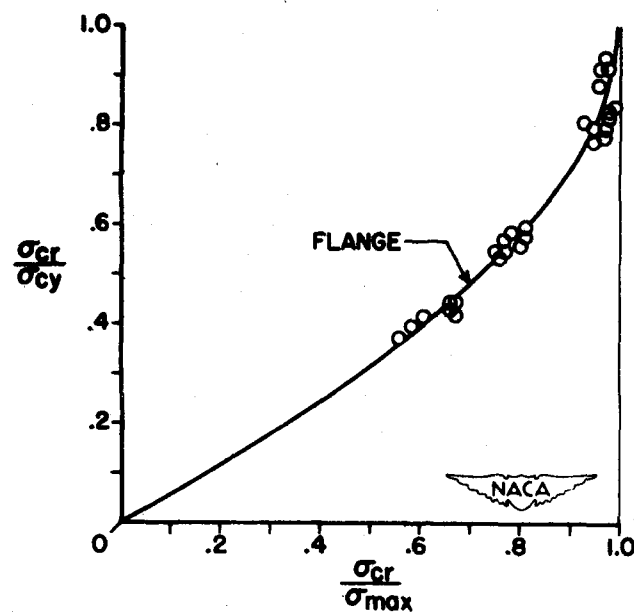
Figure 9.- Relation of maximum stress for flange to critical stress.
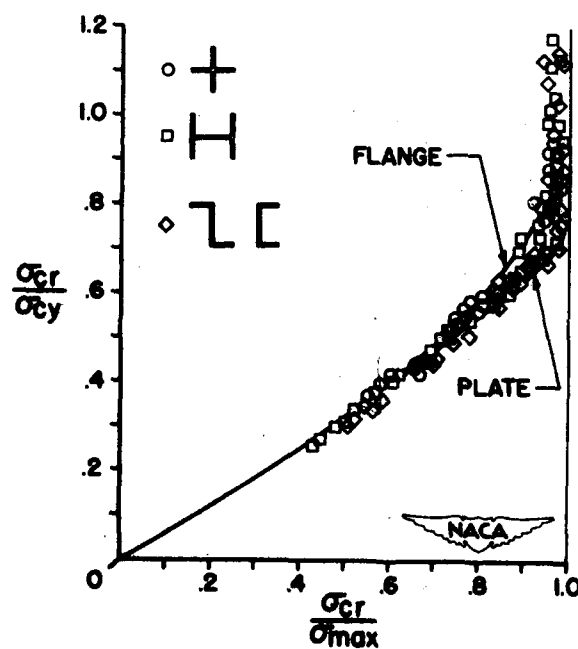
Figure 10.- Relation of maximum stress for both plate and flange to critical stress compared with room temperature experiments.
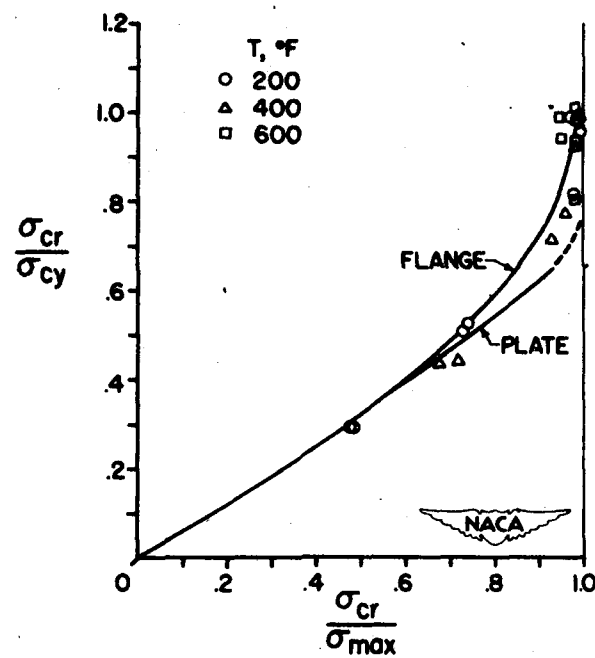
Figure 11.- Relation of maximum stress for both plate and flange
to critical stress compared with elevated temperature experiments.
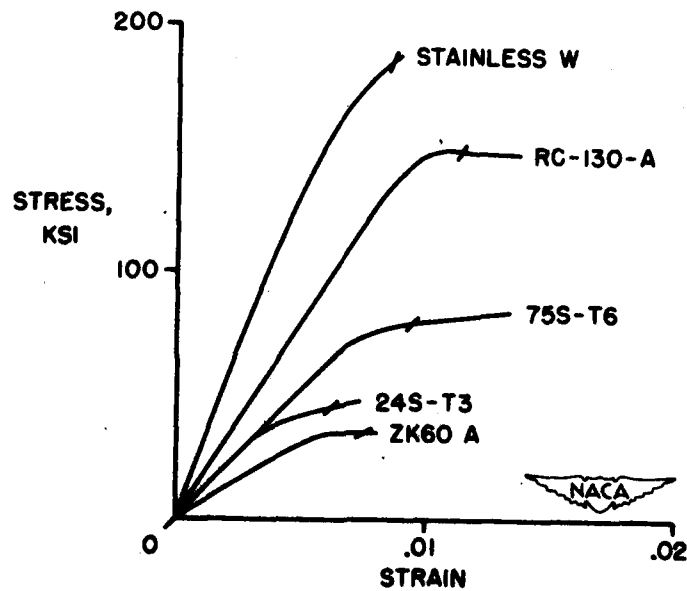
Figure 12.- Compressive stress-strain curves for several materials.
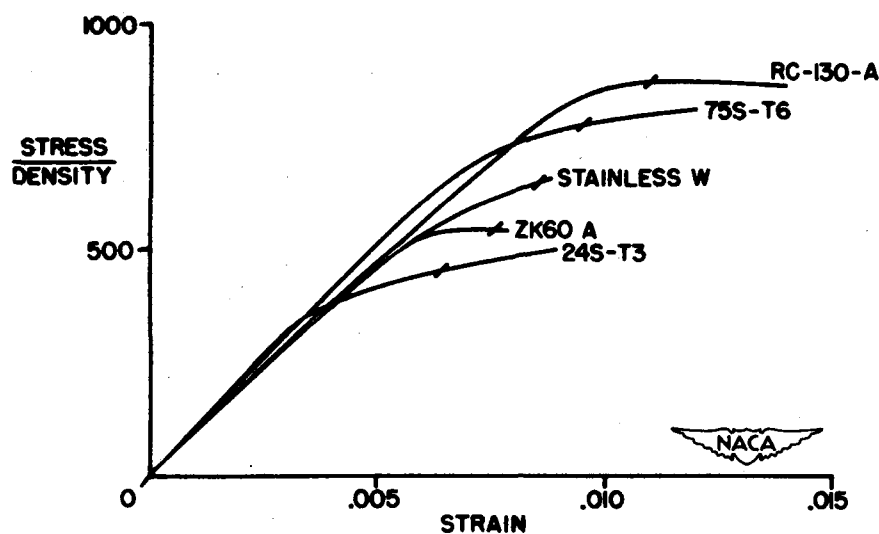
Figure 13.- Compressive stress-density ratios plotted against strain for the same materials in figure 12.
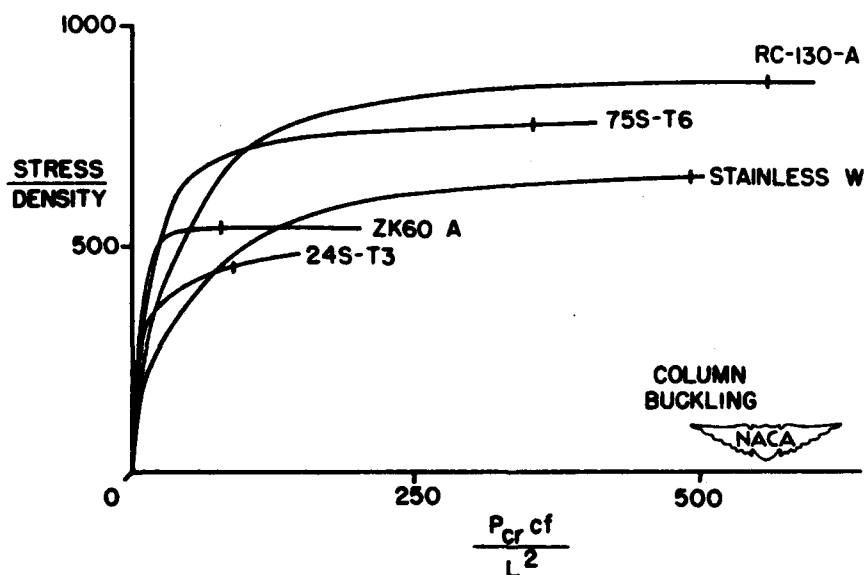
Figure 14.- Structural efficiencies of various materials for column buckling at room temperature.

16
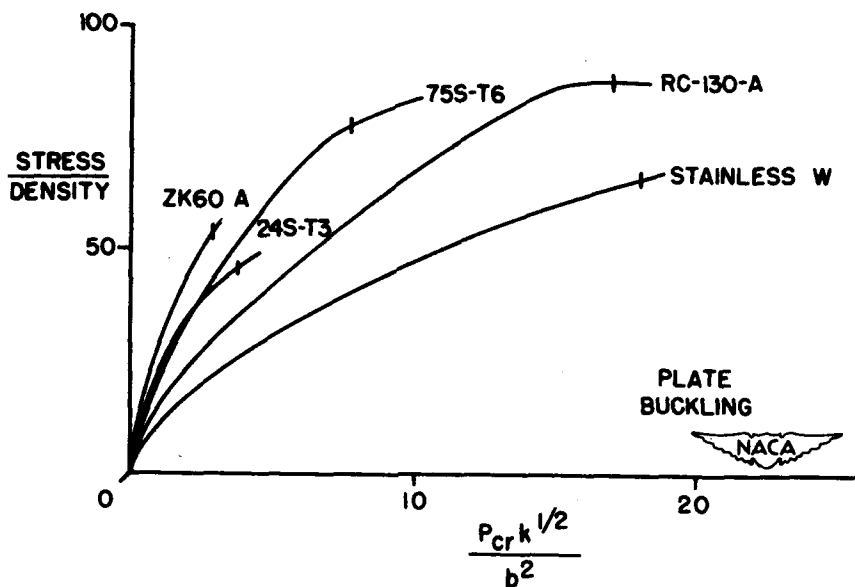
Figure 15.- Structural efficiencies of various materials for plate buckling at room temperature.
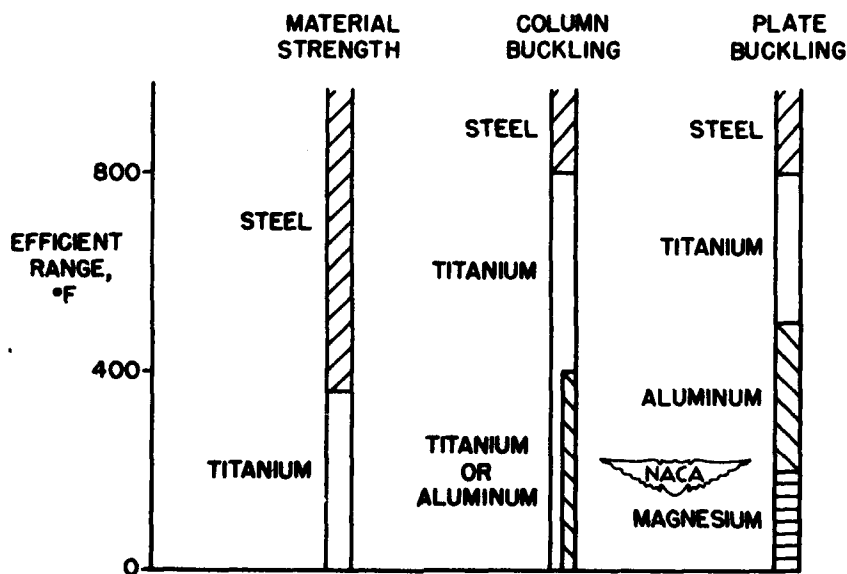
Figure 16.- Comparison of structurally efficient materials at elevated temperatures for three types of service.

STRUCTURAL PROBLEMS ASSOCIATED
WITH AERODYNAMIC HEATING

FACTORS GOVERNING AERODYNAMIC HEATING

By William J. O'Sullivan, Jr.

Langley Aeronautical Laboratory

The first step in the solution of structural problems arising from aerodynamic heating is the determination of the aerodynamic and thermodynamic factors governing the exchange of heat between the structure and the air. The NACA is conducting research on these factors at supersonic Mach numbers and full-scale Reynolds numbers in free flight by means of a specially designed rocket-propelled test vehicle known as the RM-10. Already, experimental results in excellent agreement with theory have been obtained for both the steady-state case of thermal equilibrium and the transient case of aerodynamic heating and cooling within the regime of immediate importance where heat transfer by radiation may be neglected. These results are presented in detail in reference 1. Accordingly, this paper briefly outlines the aerodynamic and thermodynamic factors involved and indicates the method of applying the results.

From the laws of the conservation of energy and the conservation of mass it follows that when a particle of air is brought to rest without energy escaping from it, its temperature is increased because of the conversion of kinetic energy into heat energy. The temperature attained is called the stagnation temperature T_S and is given by the equation

$$T_S = T + T\left(\frac{\gamma - 1}{2}\right)M^2 \tag{1}$$

where T_S and T are absolute temperatures, T is the temperature of the air before being arrested, γ is the ratio of the specific heats of the air usually taken as 1.4, and M is the Mach number at which the air was moving before being arrested. The second term on the right-hand side of this equation is the stagnation-temperature rise. In figure 1 is plotted the stagnation temperature in $^{\circ}F$ against Mach number for sea-level conditions and for the isothermal stratosphere extending from about 35,000 feet to 105,000 feet altitude in the NACA Standard Atmosphere (reference 2) and the NACA Tentative Tables for the Properties of the Upper Atmosphere (reference 3). To the right of this graph are marked significant temperatures for the purpose of orientation. They are the approximate temperatures at which aluminum and magnesium alloys lose 90 percent of their room temperature strength, their melting temperatures, and the temperatures at which a grey body exhibits incipient, dull-red, and bright-red glows. It is evident that aerodynamic heating is structurally important at Mach numbers currently contemplated for airplanes and already achieved by guided missiles. This

paper, however, is confined to the lower supersonic Mach numbers, which are of immediate importance where heat transfer by radiation may be neglected.

An airplane or guided missile experiences aerodynamic heating because the air in contact with the surface is brought to rest by the action of the viscosity of the air. This phenomenon is illustrated in figure 2. In this figure, there is shown on the left a typical variation of air velocity with distance from the skin surface through the entire thickness of the boundary layer. As the surface is approached the velocity decreases from the local velocity V_L just outside the boundary layer to zero at the surface. Accordingly, the air temperature increases as the surface is approached, as shown by the temperature profile on the right. It is interesting to note that the most rapid decrease in velocity and increase of temperature occurs close to the surface.

Consider first the steady-state case where the aircraft skin and the boundary layer have reached thermal equilibrium; that is, no net flow of heat occurs from the boundary layer to the skin nor from the skin to the boundary layer. The skin and the air in contact with it are not at the stagnation temperature but at some lower temperature called the adiabatic wall temperature T_{AW} because the temperature gradient from the surface outward into the stream is causing an outward flow of heat within the boundary layer. The fraction of the local stagnation-temperature rise that actually occurs under this equilibrium condition is called the boundary-layer recovery factor β and is defined by the equation

$$\beta = \frac{T_{AW} - T_L}{T_S - T_L} \tag{2}$$

The numerator $T_{AW} - T_L$ is the actual temperature rise across the boundary layer. The denominator $T_S - T_L$ is the local stagnation-temperature rise or the maximum possible rise that could occur.

In figure 3 is shown in outline the aforementioned RM-10 research vehicle. The value of the recovery factor β has been measured experimentally in free flight at supersonic speeds and full-scale Reynolds numbers in axially symmetric flow on the parabolic body of revolution of the RM-10. In the graph of figure 3 are shown time histories of the Mach number M, stagnation temperature T_S, and skin temperature at a station near the nose T_1 and near the tail T_2 during a typical flight. The model is propelled from rest to its maximum Mach number in about 3.3 seconds by an internal rocket motor and thereafter coasts

down through the speed range. At the instant of maximum skin temper-
ature at any point on the skin there is no net heat flow between that
point of the skin and the boundary layer as evidenced by zero value of
the rate of change of temperature of the skin. At this instant, the
conditions are the same as in the steady-state case and provide a means
of determining the recovery factor β. Since there is no net heat flow
at this instant it must be that the air in contact with the skin is at
the same temperature as the skin. Thus, the adiabatic wall temperature
T_{AW} is known. The stagnation temperature is known from the measured
flight conditions, and the temperature just outside the boundary layer
can be found either by calculating the flow about the body by theory
alone or by theory with the aid of experimental pressure distributions.
This method of determining the recovery factor assumes that the longi-
tudinal flow of heat through the skin is negligible, which point was
investigated and found to be the case in these tests.

The experimental values of recovery factor so obtained are
presented in figure 4. The recovery factor β is plotted against
distance from the nose of the model. Comparison is made with the theo-
retical values (references 4 and 5) based on conditions just outside
the boundary layer. The results are in excellent agreement with theory.

For structural purposes, the equilibrium or steady-state temper-
ature ultimately attained in steady flight can readily be calculated
for airplanes and guided missiles having conventional structures con-
sisting of relatively thin reinforced skins that offer negligible paths
for the flow of heat through the structure. The equation defining the
recovery factor (equation (2)) need only be solved for the adiabatic wall
temperature T_{AW}, which is the equilibrium temperature. The theoretical
values of the recovery factor may confidently be employed on slender
bodies like that of the RM-10, and it is observed that, since the lami-
nar and turbulent values differ by less than 6 percent, there is evi-
dently little need in a practical problem for knowing precisely the
point of transition from laminar to turbulent boundary layer.

In figure 5 is considered the transient case where the aircraft
skin and the boundary layer are not in thermal equilibrium so that the
temperature of the skin is either increasing or decreasing. Shown in
this figure is an element of skin. This skin element is assumed to be
sufficiently distant from any stiffeners or bulkheads in contact with
the skin so that no flow of heat takes place between this skin element
and any stiffeners or bulkheads. Further, let it be assumed that the
temperature variation along the skin is small so that heat flow along
the skin is negligible. In short, any heat flowing into or out of this
element of skin is assumed to come from or return to the boundary layer
in contact with it. Under these conditions, the rate of heat flow $\frac{dQ}{dt}$
into or out of this element of skin is given by

$$\frac{dQ}{dt} = h_e \, A\left(T_{AW} - T_W\right) \tag{3}$$

where T_W is the temperature of the skin and T_{AW} is the adiabatic
wall temperature, so that the quantity $T_{AW} - T_W$ is the temperature
potential that is assumed to cause heat to flow between the boundary
layer and the skin. The rate of heat flow is proportional to this
temperature difference, to the area A of the element of skin in con-
tact with the boundary layer, and to a coefficient h_e called the
equivalent heat-transfer coefficient.

Another equation can also be written for the rate of heat flow
into or out of this element of skin, namely

$$\frac{dQ}{dt} = A\tau dc \, \frac{dT_W}{dt} \tag{4}$$

In this equation, A is the area, τ is the thickness, and d is the
mass density of the element, so that $A\tau d$ is the mass of the element.
This mass multiplied by the specific heat of the skin material c, and
by the rate of change of the skin temperature $\frac{dT_W}{dt}$ gives the rate of
heat accumulation or loss of the skin element.

Equating the rates of heat flow given by equations (3) and (4)
and solving for the rate of change of skin temperatures gives

$$\frac{dT_W}{dt} = \frac{h_e \left(T_{AW} - T_W\right)}{\tau dc} \tag{5}$$

Integrating this differential equation gives the equation for the skin
temperature

$$T_W = T_0 + \frac{1}{\tau d} \int_0^t \frac{h_e \left(T_{AW} - T_W\right)}{c} \, dt \tag{6}$$

where T_0 is the initial temperature of the skin before the start of
flight. The specific heat of the skin material c has not been taken
outside of the integral because its value may change somewhat with
temperature. From this equation it is evident that if the time history
of the trajectory of the airplane or guided missile is available, the
time history of the temperature of the element of skin can be readily
determined by performing a step-by-step integration, provided that the
value of the equivalent heat-transfer coefficient h_e is known.

The NACA has experimentally determined the value of the equivalent heat-transfer coefficient h_e in free flight at full-scale Reynolds numbers and supersonic Mach numbers on the slender pointed body of revolution of the RM-10 research vehicle in axially symmetric flow. These values were obtained by use of equation (5) wherein all quantities except the equivalent heat-transfer coefficient were known during those portions of the flight in which the skin temperature was changing. The adiabatic wall temperature T_{AW} was found by use of the experimentally determined recovery factors already discussed, which were assumed to apply in the transient condition.

The correlated heat-transfer coefficient results are presented in figure 6. It may readily be shown by dimensional analysis or other theoretical means that the dimensionless parameters governing the value of the equivalent heat-transfer coefficient in aerodynamic heating in the case of a flat plate alined with the wind are the Nusselt number Nu, the Prandtl number Pr, and the Reynolds number Re. For a flat plate at subsonic speeds with turbulent boundary layer it is found from the research of Colburn (references 6 and 7) that these parameters are related by the equation

$$\mathrm{Nu\ Pr}^{-\frac{1}{3}} = 0.0296\ \mathrm{Re}^{0.8} \tag{7}$$

It was conjectured that on a slender pointed body of revolution in axially symmetric flow like that of the RM-10, and which is representative of many missiles and parts of airplanes, this flat-plate formula would closely apply. Accordingly, the Nusselt, Prandtl, and Reynolds numbers, the formulas for which are shown in figure 6, were determined by taking the value of the length l as the axial distance from the nose to the element of skin under consideration and basing the remaining quantities on the conditions existing just outside the boundary layer at the element of skin considered. These remaining quantities are the coefficient of thermal conductivity of the air k, the specific heat of the air at constant pressure c_p, the absolute viscosity of the air μ, the mass density of the air ρ, and the air velocity V. The results are shown in figure 6 where $\mathrm{Nu\ Pr}^{-\frac{1}{3}}$ is plotted against Re for nine stations along the body ranging from 8.9 inches to 123.5 inches from the nose, obtained from the flights of two models. For comparison, Colburn's flat-plate equation is also plotted on the graph and is the straight line shown.

The excellent correlation evidenced by the experimental values forming a systematic variation demonstrates that the Nusselt, Prandtl, and Reynolds numbers are indeed the factors governing the value of the equivalent heat-transfer coefficient within the range investigated.

The close agreement between the Colburn equation for a flat plate with
turbulent boundary layer and the experimental values for the slender
body of the RM-10, which was 1 foot in maximum diameter and 12.2 feet
in length, demonstrates that for practical design purposes the equiva-
lent heat-transfer coefficient can be computed from the Colburn equa-
tion for slender bodies like the RM-10 in axially symmetric flow at
supersonic Mach numbers and full-scale Reynolds numbers.

The fact that Colburn's flat-plate formula is in such close agree-
ment with the experimental values obtained in three-dimensional, axi-
ally symmetric flow on the slender RM-10 body is strong evidence for
believing that, in two-dimensional flow about thin, smooth airfoils at
low lift coefficients, particularly those with sharp leading edges, the
same correlation would probably hold. This supposition is yet to be
verified experimentally. On actual wings in three-dimensional flow the
possibility of important shock - boundary-layer interaction is present,
the effects of which are also yet to be investigated. Even on a body
of revolution such as that of the RM-10, angle of attack is known to
influence markedly the boundary layer and, presumably, also the aero-
dynamic heating. Even the internal structure conceivably can play a
part since the bulkheads or other members that attach to the skin may
act as heat sinks during heating and as heat sources during cooling so
that the boundary layer might be altered.

Despite these foreseen problems that are yet to be investigated,
the results that have been presented herein are directly applicable to
many practical cases such as the more critically heated sections of the
skin of ballistic-type trajectory missiles. Further, it is observed
that in the Nusselt, Prandtl, and Reynolds numbers the only unknown
quantity is the proper value of the length l to employ in treating a
body of arbitrary shape at any given value of angle of attack. If this
theoretical viewpoint is experimentally proven correct, it may be pos-
sible by experimentally determining the equivalent-flat-plate lengths
corresponding to various points on any given body to be able to calcu-
late the aerodynamic heating and cooling of the body under transient
conditions for any given trajectory.

If figure 3 is again examined, it is observed that when the flight
is such that the missile is propelled up to the maximum Mach number in
a short time and thereafter coasts, as might be the case with air-to-
air or ground-to-air type guided missiles, the maximum skin temper-
atures actually attained under such transient conditions are far less
than the peak stagnation temperature. These lower temperatures, to-
gether with the failure of some metals to lose their structural strength
properties until they have been at an elevated temperature for an appre-
ciable time, give promise of affording the structural designer oppor-
tunities for effecting significant weight reduction with accompanying

increase in performance and the possibility of employing materials that would be ruled out on the basis of a nontransient analysis of the aerodynamic heating.

REFERENCES

1. Chauvin, Leo T., and deMoraes, Carlos A.: Correlation of Supersonic Convective Heat-Transfer Coefficients from Measurements of the Skin Temperature of a Parabolic Body of Revolution (NACA RM-10). NACA RM L51A18, 1951.

2. Diehl, Walter S.: Standard Atmosphere - Tables and Data. NACA Rep. 218, 1925. (Reprint 1940.)

3. Warfield, Calvin N.: Tentative Tables for the Properties of the Upper Atmosphere. NACA TN 1200, 1947.

4. Wimbrow, William R.: Experimental Investigation of Temperature Recovery Factors on Bodies of Revolution at Supersonic Speeds. NACA TN 1975, 1949.

5. Squire, H. B.: Heat Transfer Calculation for Aerofoils. R. & M. No. 1986, British A.R.C., 1946.

6. Colburn, Allan P.: A Method of Correlating Forced Convection Heat Transfer Data and a Comparison with Fluid Friction. Trans. Am. Inst. Chem. Eng., vol. XXIX, 1933, pp. 174-210.

7. Anon.: A Design Manual for Determining the Thermal Characteristics of High Speed Aircraft. (Reprint). AAF TR No. 5632, Air Materiel Command, U. S. Air Force, Sept. 10, 1947.
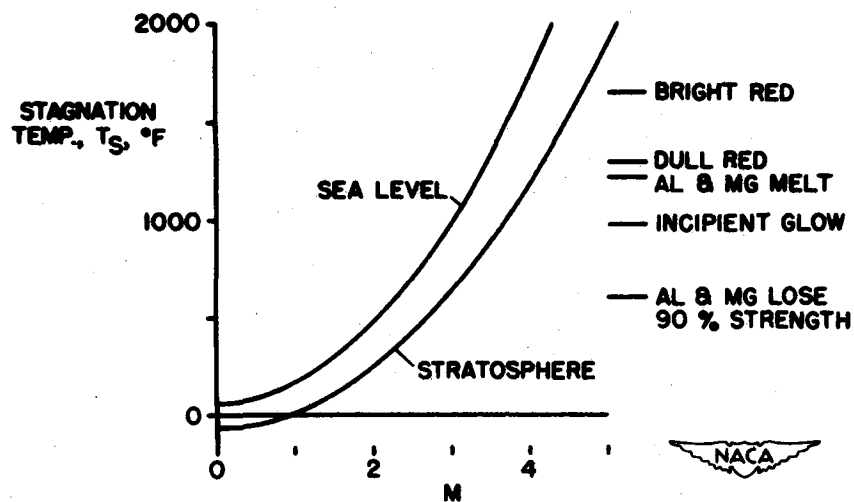
Figure 1.- Variation of stagnation temperature with Mach number.

$$\beta = \frac{T_{AW} - T_L}{T_S - T_L}$$
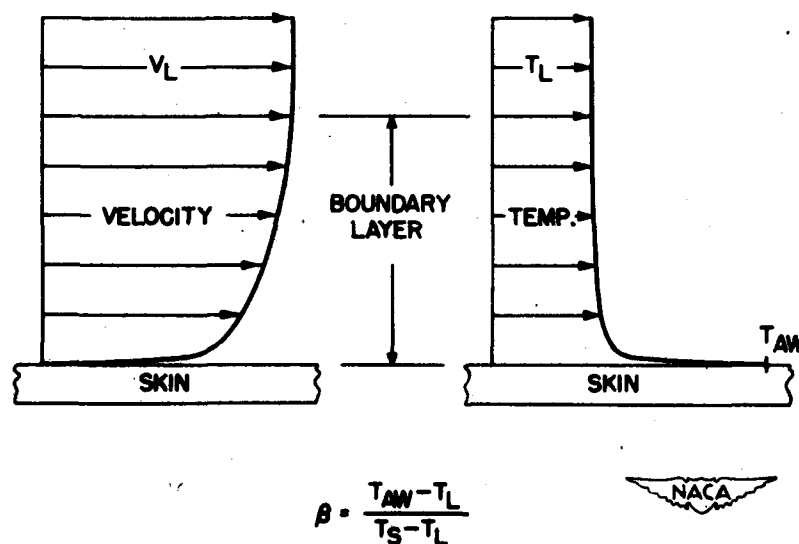
Figure 2.- Illustrative velocity and temperature profiles of
a turbulent boundary layer.
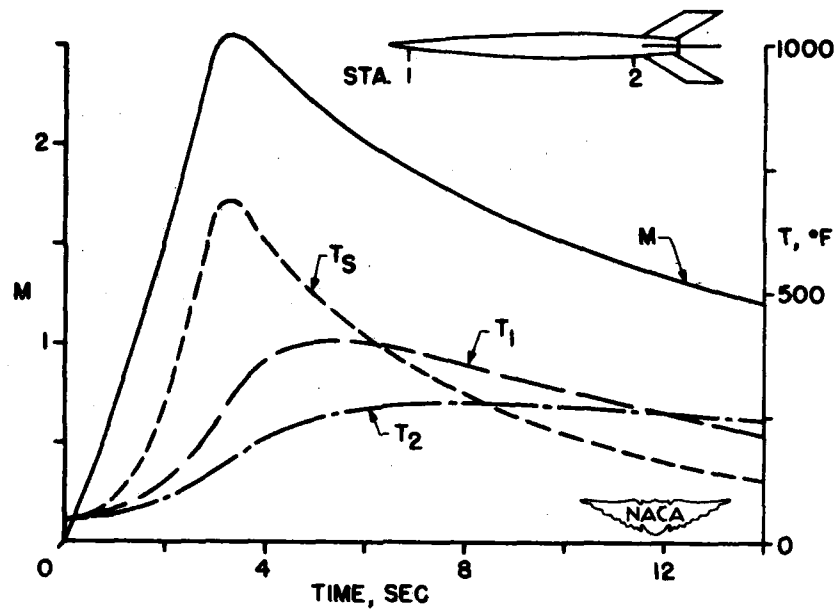
Figure 3.- Time histories of Mach number, stagnation temperature, and skin temperature at two stations during a flight of the NACA RM-10 research vehicle.
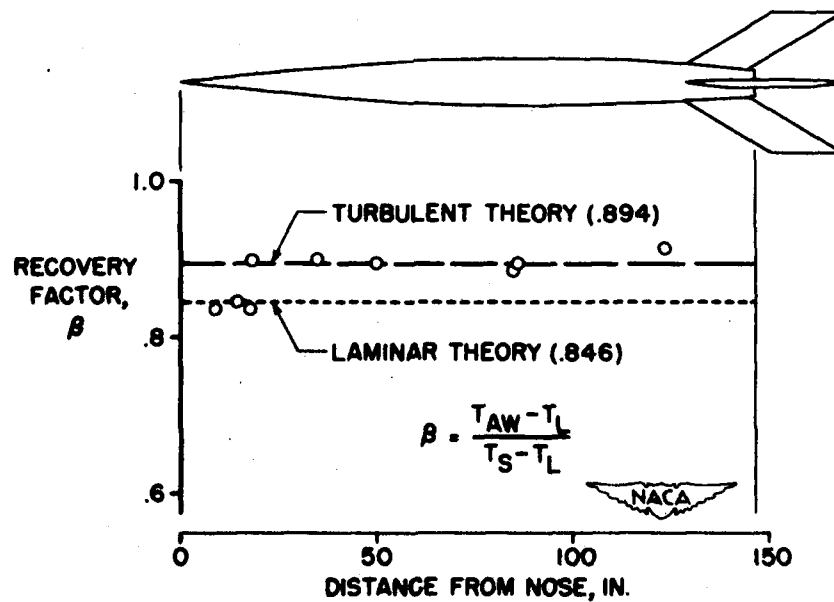
Figure 4.- Experimental values of recovery factor on NACA RM-10 research vehicle.

$$\frac{dQ}{dt} = h_e A(T_{AW} - T_W) \qquad \frac{dT_W}{dt} = \frac{h_e(T_{AW} - T_W)}{\tau d c}$$

$$\frac{dQ}{dt} = A\tau dc \frac{dT_W}{dt} \qquad T_W = T_0 + \frac{1}{\tau d}\int_0^t \frac{h_e(T_{AW} - T_W)}{c} dt$$

Figure 5.- Illustration of physical concepts involved in equations governing heat transfer in aerodynamic heating.

$$Nu\,Pr^{-\frac{1}{3}} = 0.0296\,Re^{0.8}$$

$$Nu = \frac{h_e l}{k}$$

$$Pr = \frac{c\rho\mu}{k}$$

$$Re = \frac{Vl\rho}{\mu}$$
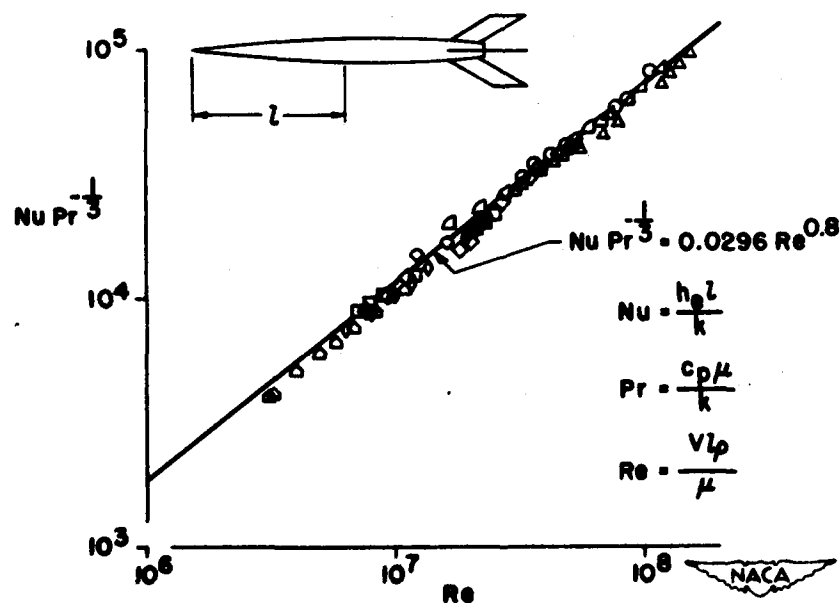
Figure 6.- Correlation of parameters governing equivalent heat-transfer coefficient.

THEORETICAL AND EXPERIMENTAL DETERMINATION OF THERMAL STRESSES

By Richard R. Heldenfels and William M. Roberts

Langley Aeronautical Laboratory

Designing an aircraft structure which will withstand the temperatures resulting from aerodynamic heating presents many problems, one of which is the determination of the thermal stresses induced in a structure by a given temperature distribution. The purpose of this paper is to describe some of the theoretical and experimental thermal-stress problems studied by the Langley Structures Research Division.

To begin with, what are thermal stresses? Thermal stresses are those stresses which are induced in a structure as a result of unequal thermal expansion of its parts. This unequal expansion may result from materials with different coefficients of thermal expansion or from a temperature distribution that is not uniform. Unequal expansion alone, however, is not sufficient since a linear distribution across the structure may result in thermal deformation without thermal stresses; however, such simple results are rare in practice. In any case, the thermal stresses depend only upon the temperature distribution and the characteristics of the structure and are independent of any applied loads.

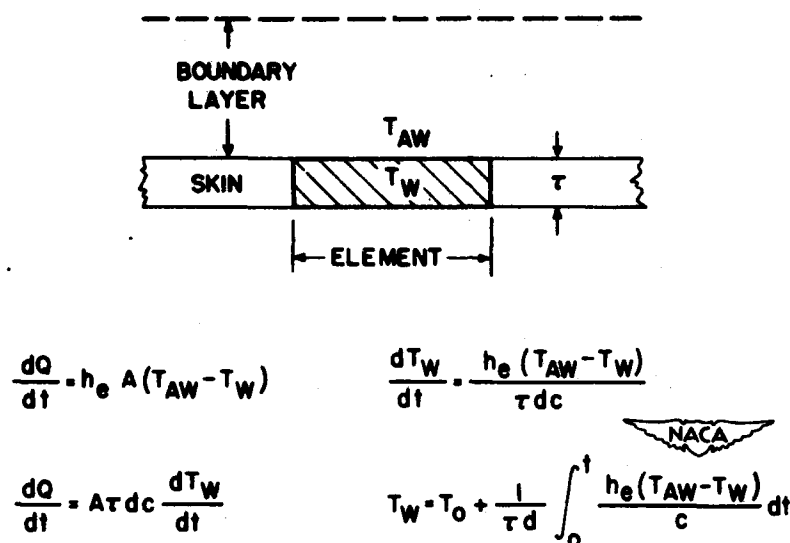Under what conditions, then, will aerodynamic heating induce thermal stresses in an aircraft structure? If the structure is made of dissimilar materials, any temperature change, and thus any aerodynamic heating, may induce thermal stresses. If the structure is of but one material, then temperature differences or nonuniform distributions are necessary to produce thermal stresses. Aerodynamic heating produces nonuniform temperature distributions as a result of transient conditions; thus, thermal-stress problems may arise from accelerating and decelerating supersonic flight. Although the temperature problem is a transient one, the stress distribution at any instant of time can be treated as a steady-state problem because stress changes are propagated much faster than temperature changes.

Now that the conditions under which thermal stresses are likely to occur are known, the next question is, what can be done about calculating them? The answer is that for a given temperature distribution thermal stresses can, in principle, be determined by application of the theory of elasticity, provided the material properties are known for the temperature conditions encountered. However, the problem is complicated by material properties which vary with temperature with the result that exact analytical solutions usually cannot be obtained and approximate numerical solutions are very tedious. A number of stress-analysis procedures, ranging from the very general to the very simple

and involving various assumptions and approximations, have been established and this material is available in two recently published papers, references 1 and 2.

Even if there are theoretical methods for determining thermal stresses, there is a need for experimental methods to establish the accuracy of approximate theories and to analyze those structures for which theoretical analyses are impractical. Thermal stresses have been measured and correlated with theory, and, since this work has not yet been published, it will be described in detail.

How does one measure thermal stresses? To answer this question, commercially available wire strain gages were studied and their characteristics under various temperature conditions between 80° F and 300° F were determined. It was found that the biggest problem was to devise a satisfactory means of differentiating between strain readings due to thermal expansion and those due to stresses. Two methods were available. One was to provide individual dummy gages with individual temperature control; however, this method required an impractical amount of apparatus and did not insure a high order of accuracy because of differences in individual gage installations. The other method was to calibrate the gages under all combinations of stress and temperature anticipated. The important results of this calibration project are given in figure 1 which shows the effects of stress and temperature on the indicated strain of a typical wire strain gage mounted on a 75S-T6 aluminum-alloy specimen.

Two quantities are needed to describe these calibration curves; the slope of each line which is actually the modulus of elasticity of the specimen and the horizontal intercept, or zero shift, which is a measure of the thermal expansion of the specimen, the strain gage, and the bonding material. The calibration tests revealed that the strain gages yielded accurate values for the slopes over the temperature range considered and that there was negligible variation between individual gage installations on the same material. This was not true with regard to the zero shift which showed considerable variation between individual gage installations. Therefore, the only calibration required for the thermal-stress investigation was the determination of the zero shift; however, the zero shift had to be determined for each individual strain-gage installation in order to get accurate test results. This was done by placing the entire test specimen, with gages installed, in a furnace, cycling the temperature to stabilize the gages, and then measuring the zero shift for the various temperatures anticipated. This zero-shift calibration of each strain-gage installation is a distinct disadvantage in practical applications, but it was found necessary for accurate results. If errors of 1000 pounds per square inch are permissible, however, an average value of the zero shift can be used.

18

Knowing how to interpret the gage readings for a simple state of temperature and stress, the next step was to see how satisfactory this method of calibration was for measuring thermal stresses. Figure 2 shows the specimen used for such a thermal stress test. It was a $\frac{1}{4}$-inch 75S-T6 alluminum-alloy plate measuring 24 by 36 inches that was arranged to provide a simple two-dimensional distribution of thermal stress under steady-state conditions. It was heated along the longitudinal center line by an electrical heating element and cooled along the longitudinal edges by water flowing through plastic tubes. The sides and edges of the panel were insulated to minimize heat loss through these surfaces and to insure that the strain gages were at the same temperature as the panel. Strain-gage rosettes and thermocouples were mounted on one quadrant of the panel and the flow of cooling water was controlled so that the temperature distribution was symmetrical in both transverse and longitudinal directions. Since the thermal stresses tended to buckle the center of the plate, it was mounted on a wooden jig to restrain this buckling. In addition the strain gages were mounted on both sides of the plate and their readings averaged so that the test results would approximate a state of plane stress. (The next paper by Myron L. Gossard and William M. Roberts will describe an analysis of this plate when buckling is allowed.)

Figure 3 illustrates the temperature increase of the plate over room temperature, that is, the temperature at which the gages were zeroed. The line shown is the temperature distribution assumed for the theoretical calculations of the thermal stresses and corresponds to simple conduction between a concentrated heat source along the longitudinal center line and a concentrated heat sink along each edge. The temperature difference between the center line and the edges is 150° F. The actual distribution, shown by the test points, was slightly different because of the finite area of the source and sink and because of heat loss through the sides and ends of the plate, but it agrees within a few degrees at the measured points. The temperature was essentially constant in the longitudinal direction.

Figure 4 illustrates the longitudinal direct stress induced in the plate by the temperature distribution. The squares and circles represent test data and the lines represent theoretical results. The stresses are shown at the two stations where the maximum measured values were obtained and the complete distribution is symmetrical in both the transverse and longitudinal directions. The results show that the hot parts of the plate are in compression and the cold parts are in tension as would be expected since the cold parts restrain the greater expansion of the hot parts. The stresses at the transverse center line approximate those given by an elementary analysis of a very long plate; however, this particular specimen was so short that there is a very pronounced secondary effect throughout the rest of the plate because the

stresses must go to zero at the unrestrained ends. The theoretical
results shown were obtained from an approximate solution based on the
principle of minimum complementary energy. Although this is an approxi-
mate solution, it agrees well with the test points.

Figure 5 illustrates the induced shear stresses. The shear
stresses are associated with the effect of the stress-free end and
depend upon the rate of change of the stresses shown in figure 4; how-
ever, the agreement between theory and experiment is still good. These
stresses are antisymmetrical about the two center lines and are thus
zero along these center lines as well as along the unrestrained edges.

Figure 6 shows the transverse direct stress induced in the plate.
These stresses also arise because of the stress-free end and are
symmetrical about the two center lines.

In conclusion, fairly accurate measurements of thermal stresses
have been obtained by use of wire strain gages and a special cali-
bration technique. However, the calibration technique has the dis-
advantage that it requires a special test run to establish a zero shift
for each gage; thus there is a need for a reliable, self-compensating
strain gage for the measurement of thermal stresses. Additional tests
are planned to check the accuracy of approximate methods for the stress
analysis of built-up structures.

REFERENCES

1. Heldenfels, Richard R.: The Effect of Nonuniform Temperature Dis-
      tributions on the Stresses and Distortions of Stiffened-Shell
      Structures. NACA TN 2240, 1950.

2. Heldenfels, Richard R.: A Numerical Method for the Stress Analysis
      of Stiffened-Shell Structures under Nonuniform Temperature Dis-
      tributions. NACA TN 2241, 1950.

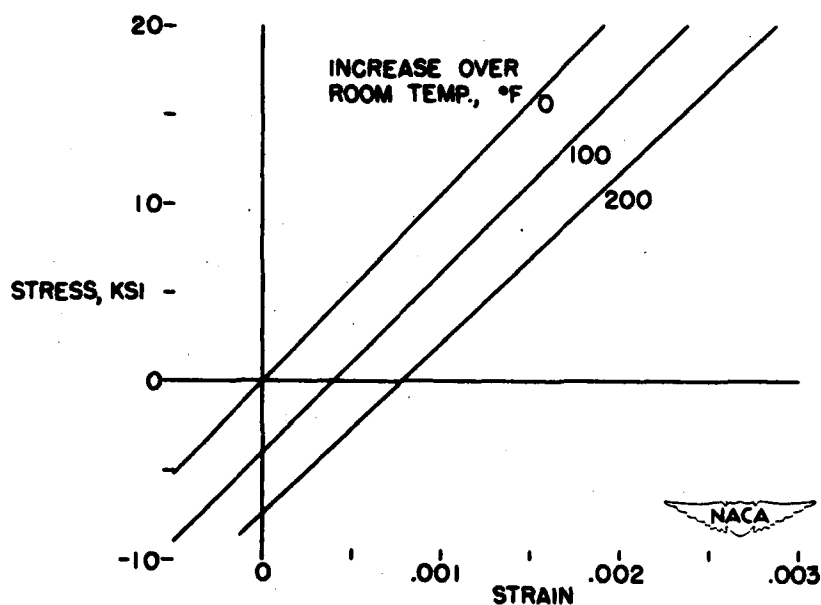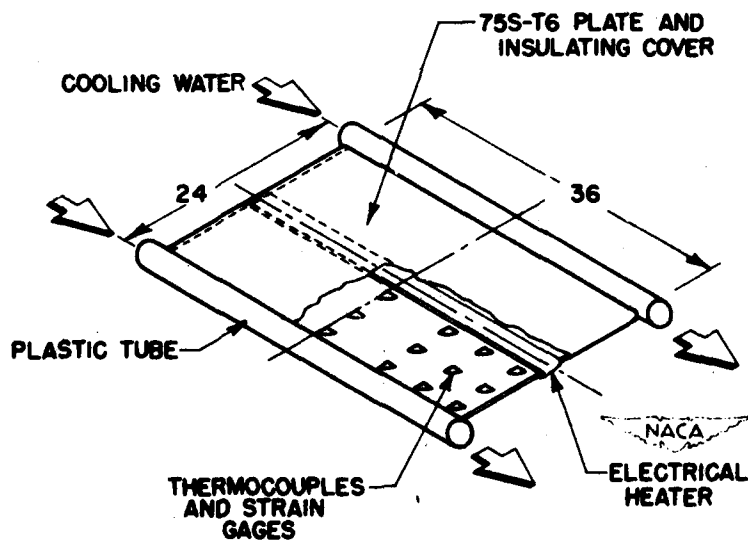Figure 1.- Typical calibration curves for wire strain gages mounted on 75S-T6 aluminum alloy.

Figure 2.- Plate used for thermal-stress tests.
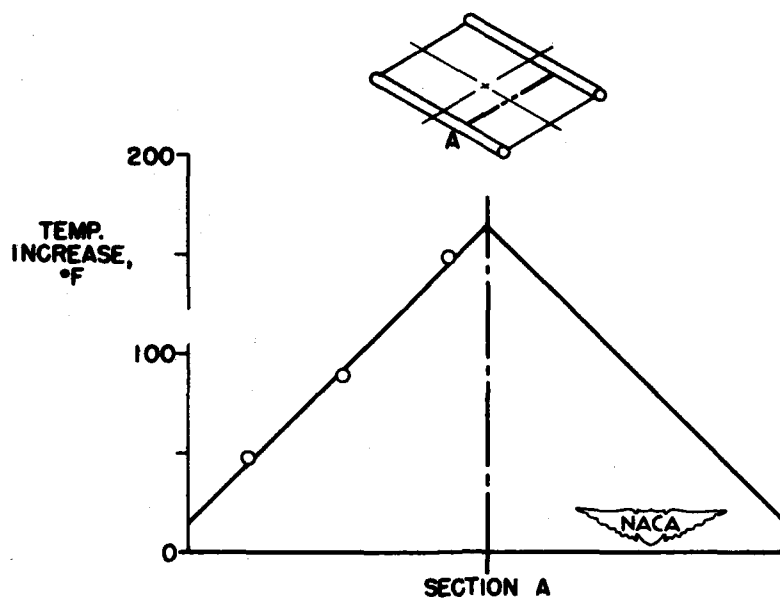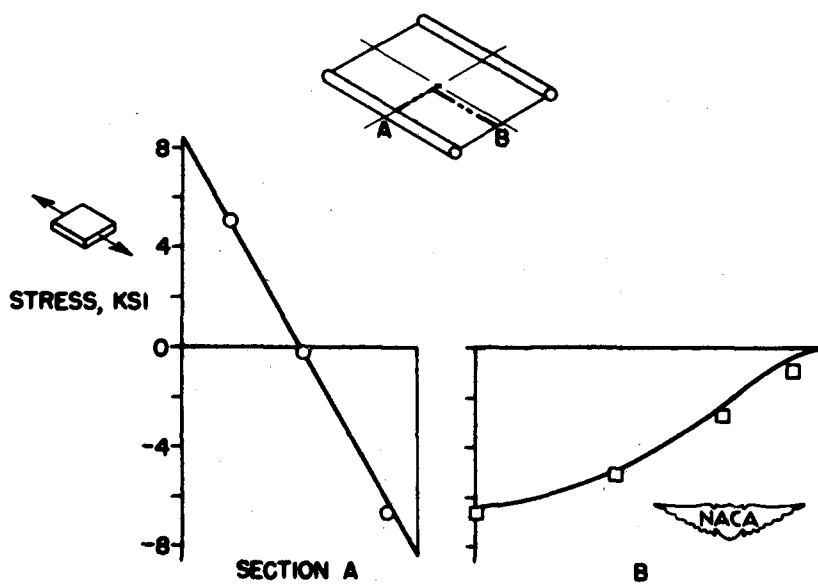
Figure 3.- Distribution of temperature increase.

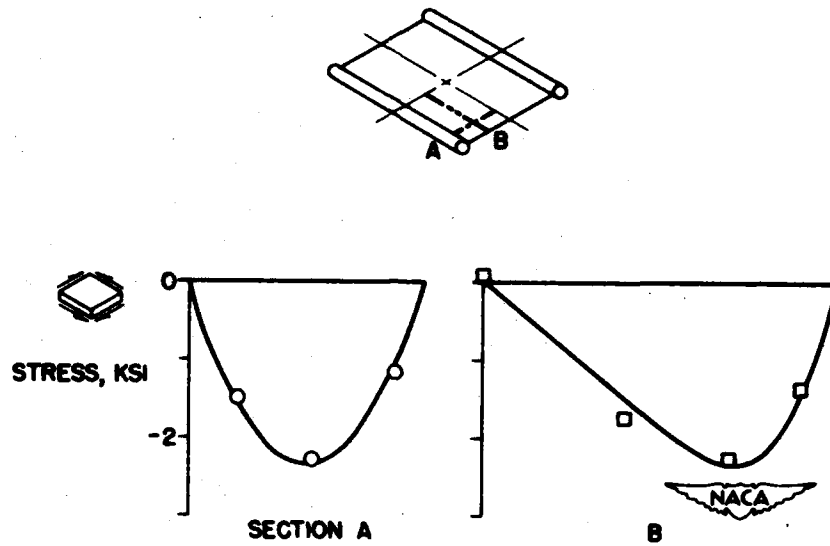Figure 4.- Longitudinal direct stresses induced by the
temperature distribution.

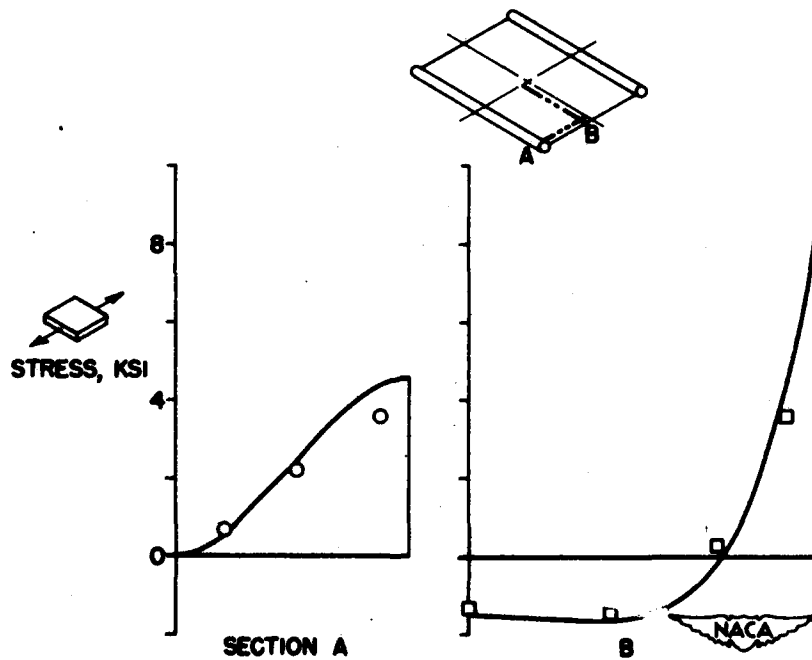Figure 5.- Shear stresses induced by the temperature distribution.

Figure 6.- Transverse direct stresses induced by the temperature distribution.

THERMAL BUCKLING OF FLAT PLATES

By Myron L. Gossard and William M. Roberts

Langley Aeronautical Laboratory

The nonuniform heating of supersonic aircraft may cause parts of the structure to buckle. Since buckling of the aerodynamic surfaces may have an adverse effect on the performance of the aircraft, the designer should know under what temperature distributions buckling will occur. In some cases it may not be feasible to design a structure which will not buckle, and the designer should know the depth of the buckles in order to estimate their effect on the performance of the aircraft.

Figure 1 shows two types of thermal bulging of plate panels that may arise from nonuniform temperatures. The first type of bulging is caused by nonuniformity of temperature through the thickness of the plate. If the temperature varies linearly through the thickness and is constant over the two surfaces, an unrestrained plate assumes a spherical shape as illustrated in figure 1(b) and the deformation takes place without the appearance of thermal stresses. This type of bulging has the same structural significance as the usual initial out-of-flatness that occurs in sheet-metal structures. If, however, the edges of such a plate are restrained, stresses will be induced in the plate.

The second type of bulging develops when the temperature is non-uniform over the middle surface of the plate. If this temperature variation is nonlinear, for example, as indicated in figure 1(c), thermal stresses will be induced in the plate regardless of the manner of edge restraint, and the plate will buckle somewhat as shown in fig- ure 1(d) in a manner analogous to that which occurs under externally applied forces. Combinations of these two types of bulging will gen- erally occur in aircraft structures subjected to heating.

The temperature distributions and buckle patterns in various types of stiffened panels, under thermal conditions designed to simulate the initial period of flight, have been experimentally investigated by the Lockheed Aircraft Corporation and reported in Air Force Technical Report 5774. NACA in this research has been concerned thus far with a theoretical as well as an experimental study of buckling of a flat plate subjected to a simple type of nonlinear temperature distri- bution over the surfaces, with constant temperature through the thickness.

In approaching the thermal buckling problem theoretically, the established methods of the theory of elastic stability can be applied,

provided suitable modifications are made to account for thermal expansion. The thermal conditions under which buckling could begin for a flat plate can be determined by small-deflection buckling analysis; the calculation of buckle depth requires a large-deflection analysis, however. The difference between these two analyses is illustrated by the following two equations:

$$\nabla^4 F = -E\alpha\nabla^2 T + E\left[\left(\frac{\partial^2 w}{\partial x \partial y}\right)^2 - \frac{\partial^2 w}{\partial x^2}\frac{\partial^2 w}{\partial y^2}\right]$$

$$\nabla^4 w = \frac{q}{D} + \frac{h}{D}\left(\frac{\partial^2 F}{\partial y^2}\frac{\partial^2 w}{\partial x^2} + \frac{\partial^2 F}{\partial x^2}\frac{\partial^2 w}{\partial y^2} - 2\frac{\partial^2 F}{\partial x \partial y}\frac{\partial^2 w}{\partial x \partial y}\right)$$

The large-deflection equations, first derived by Von Kármán except for the temperature term, are the full set of equations as given. The small-deflection equations are these two equations if in the first equation the terms involving deflection w are removed. These terms account for the stretching of the midplane, which becomes appreciable when deflections are greater than about one-third the plate thickness. Although the terms involving w in the first equation are not needed in determining the critical buckling temperature and initial buckle shape, they must be retained even for small deflections if the magnitude of the buckle is to be determined.

Exact solutions of these equations are, in general, difficult to obtain, but approximate solutions can be made by several methods.

In the studies of thermal buckling the energy method has been used to analyze a simply supported flat plate of the dimensions shown in figure 2. The temperature was constant through the plate thickness and distributed nonlinearly over the surfaces in the tentlike fashion shown in figure 2. This is the same panel as that just discussed by Richard R. Heldenfels and William M. Roberts. The critical buckling temperature and buckling problem were determined by introducing the calculated thermal stresses and a deflection pattern with several undetermined parameters into the energy expression of classical theory and by minimizing the total energy with respect to the parameters. Deflections for temperatures above the critical (in the large-deflection range) were determined by assuming that the shape of the buckle pattern

remained the same as at the critical temperature but increased in magnitude according to a law which, on a weighted average over the plate, satisfies equilibrium.

The results of this study are shown in figure 3 where the maximum buckle depth is plotted against the temperature difference between the center line and the edges. The two solid-line curves are theoretical results, with deflection starting at the critical temperature given by small-deflection theory. The upper solid curve would apply if during buckling the edges of the plate were required to remain straight but were otherwise free to move in the plane of the plate; whereas the lower solid curve applies to a plate which is stress free at the edges. Test data shown by the circular symbols were obtained from a panel mounted so as to provide simple-support and stress-free conditions at the edges; therefore the lower solid curve should be compared with the test data. However, the test data indicate an initial out-of-flatness of the plate and, therefore, the theoretical result should be adjusted to account for the effect of this out-of-flatness. When this is done in a manner suggested by P. P. Bijlaard for an initial out-of-flatness at the plate center of $13\frac{1}{2}$ percent of the plate thickness, the dashed-line theoretical curve is obtained and the agreement of experiment and theory is seen to be fairly good.

In conclusion, thermal buckling in supersonic aircraft may be analyzed quite accurately if the temperature distribution is known. The shape and magnitude of the buckle for any temperature may then be determined. This determination required only simple modifications of established methods but the calculation procedures required are apt to be complicated and tedious.
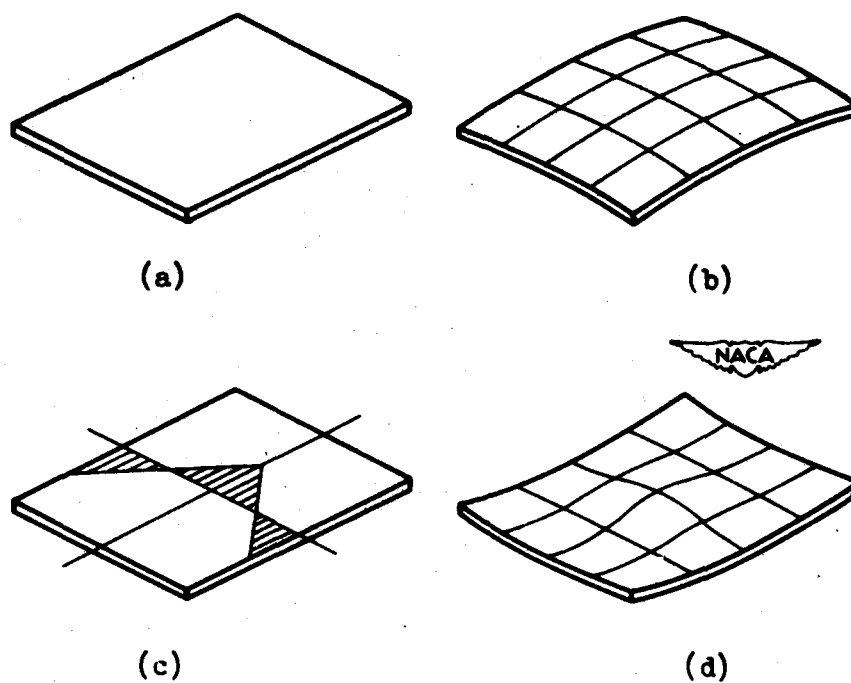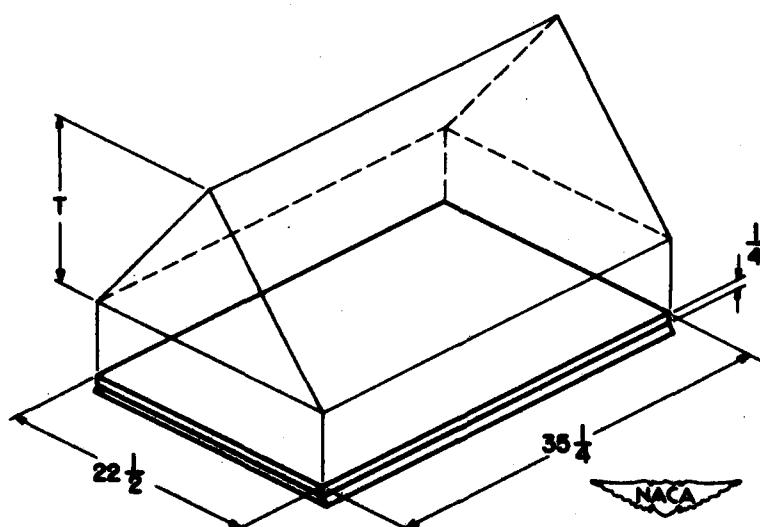
Figure 1.- Types of thermal bulging.

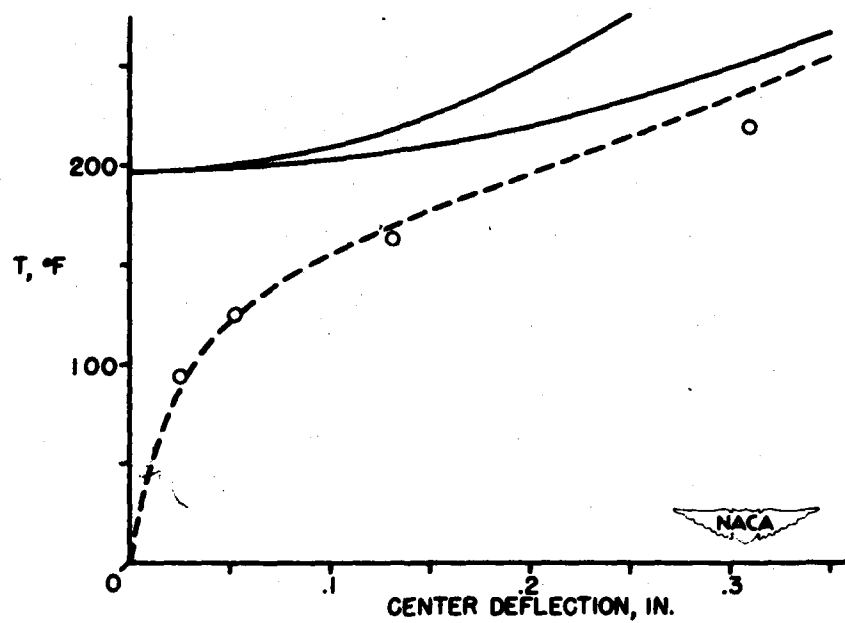Figure 2.- Plate dimensions and temperature distribution.

Figure 3.- Variation of buckle depth with temperature.

SOME AIRCRAFT STRUCTURAL PROBLEMS RESULTING FROM CREEP

By Charles Libove and George J. Heimerl

Langley Aeronautical Laboratory

At temperatures to be encountered in supersonic flight, time becomes an influential factor in determining the strength, stresses, and deformations of the aircraft structure. This occurs through the mechanism of creep, which is a phenomenon that is highly accentuated by increased temperature. Creep is manifested by a change in strain with time even when the load and temperature are kept constant.

The creep characteristics of a metal are usually described by a set of creep curves of the kind shown in figure 1. These are obtained by tests on tension specimens which show the change of strain with time for various values of constant tensile load. The particular curves in figure 1 are for 75S-T6 alluminum alloy at 600° F and are based on an empirical formula suggested in reference 1. The material was stabilized at 600° F for 100 hours prior to test. The extreme sensitivity of creep to stress should be noted. Similar sensitivity exists with regard to temperature.

One obvious effect of creep is a constant change in geometry as time progresses. In an aircraft this would mean, for example, a continual increase in dihedral of wings caused by compressive creep in the upper surface and tensile creep in the lower surface. Another consequence of creep is stress relaxation, which is manifested by a gradual reduction in stress when the strain remains constant. Stress relaxation could be beneficial in the aircraft structure by relieving high stress peaks resulting from thermal expansion. It is harmful, however, in that it can cause loosening of rivets and other connections that are supposed to remain tight. Creep further complicates the aircraft design picture by virtue of the fact that its strains are cumulative and generally result in fracture in some finite time.

It is clear, then, that in designing the aircraft structure for high temperatures, consideration will have to be given to the factors of permissible deformation and desired service lifetime. In these respects the design of aircraft to prevent creep involves the same problems as the design of any other high-temperature equipment. For aircraft, however, one additional factor will have to be considered, namely, the effect of creep on the maximum load-carrying capacity of members subject to instability, such as columns and flat and curved plates. At room temperatures, many tests and theory have indicated a correlation between buckling strength and the stress-strain curve. (For example, see references 2 and 3.) The same sort of correlation has been shown to exist at high temperatures provided there is no

appreciable creep, or, in other words, provided the load is brought up to its buckling value in a fairly short time (reference 4). If, however, the load is brought up to a value below the buckling strength of the structural element and kept there for some time, as it always would be, and if the stress is high enough, creep will occur, and there arises the possibility that the element will eventually fail even though the load is below the short-time buckling strength.

Initial eccentricities will play an important part in problems of this kind. Consider, for example, a slightly crooked column carrying a load below its short-time buckling load. Because of the crookedness, one side of the column will be stressed more highly than the other side. Because of the higher stress, creep will occur more rapidly on one side than on the other side. This will increase the crookedness, which in turn will increase the stress difference, and so forth. Instead of resulting in a final equilibrium position, this process may diverge and cause collapse of the column.

In problems of this kind, the internal stress in the structural element will change continually with time. It is clear that for the analysis of such problems the conventional creep curves which are obtained at constant stress are insufficient. Needed are tests or theory to describe what happens when the stress changes with time. Shanley has proposed such a theory which is admittedly approximate but offers hope for engineering applications (reference 5).

Shanley's theory for uniaxial tension or compression at constant temperature is illustrated in figure 2. If the material is at some condition of stress and strain represented by the point labeled (σ, ϵ) and the stress is instantaneously changed by an amount $d\sigma$, then the strain is assumed to change elastically by an amount $d\epsilon$ according to the elastic modulus for the particular temperature T of the material; the strain change can therefore be written $d\epsilon = \dfrac{1}{E(T)} d\sigma$ and it is represented by the arrow that is parallel to the elastic line. On the other hand, if the stress is kept constant for a short interval of time dt, a small strain change $d\epsilon$ occurs due to creep and is represented by the horizontal arrow. The rate at which this strain occurs is assumed to be a function only of the instantaneous values of the stress, the strain, and the temperature and not of how these conditions were attained. For constant stress, therefore, one can write $d\epsilon = f(\sigma, \epsilon, T)dt$, where dt is a small time interval and $f(\sigma, \epsilon, T)$ is a known fuction.

Shanley's formulation of a creep theory would be very desirable from an engineering viewpoint if it proves to be sufficiently accurate because any loading history can be approximated by a series of steps, as

shown in figure 3. Each step consists of an instantaneous stress change by an amount $d\sigma$ followed by a constant-stress period of length dt. The strain changes occurring during each of the two parts of the step may be added together to obtain the total strain change

$$d\epsilon = \frac{1}{E(T)} d\sigma + f(\sigma, \epsilon, T) dt$$

Dividing through by dt gives a differential equation for the strain rate, which applies in the limit as the steps become infinitesimally small. If the temperature as well as the stress were changing, another term could be added to the equation to express the strain change due to thermal expansion.

Application of the theory just described to a given structure of a given material at a given temperature requires a knowledge of the values of the creep function $f(\sigma, \epsilon, T)$ for many combinations of σ and ϵ; these values may be obtained from conventional creep curves. For example, the equation for the creep curves of figure 1 is given in reference 1 as

$$\epsilon = \frac{\sigma}{E} + Ae^{B\sigma} t^K \tag{1}$$

where

$$A = 2.64 \times 10^{-7}$$

$$B = 1.92 \times 10^{-3}$$

$$E = 5.2 \times 10^{6}$$

$$K = 0.66$$

By differentiating ϵ with respect to t, regarding σ as constant, and then eliminating t in terms of σ and ϵ, the following

expression for $f(\sigma,\epsilon,T)$ for 75S-T6 aluminum alloy at 600° F is obtained:

$$f(\sigma,\epsilon,T) = \frac{\partial \epsilon}{\partial t}\bigg]_{\sigma,T=\text{Constant}}$$

$$= \frac{K\left(Ae^{B\sigma}\right)^{\frac{1}{K}}}{\left(\epsilon - \frac{\sigma}{E}\right)^{\frac{1}{K}-1}} \tag{2}$$

In order to illustrate the type of behavior that might be expected of structural elements subject to instability when creep enters the picture, an analysis has been made of a simple pin-ended column of 75S-T6 aluminum alloy at 600° F by using Shanley's creep theory in conjunction with equation (2). The problem is that of an H-section column with a web of negligible area and with an initial crookedness in the shape of a half sine wave. (See fig. 4.) A load below the buckling load is instantaneously applied and produces an average stress $\bar{\sigma}$. The load is kept constant and because of creep the column continues to deflect laterally. The shape is assumed to remain a half sine wave and plane sections are assumed to remain plane. The problem was solved by determining the time history of the flange stresses and strains at the center of the column such that the following conditions are satisfied at all times: stresses in equilibrium with external loading; strains compatible with the assumption that plane sections remain plane and that the shape remains a half sine wave; stresses and strains must satisfy the strain-rate equation of figure 3. (In the analysis it was necessary to substitute a numerical value only for the constant K. The results of the analysis therefore apply to other materials whose creep curves have the form implied by equation (1) with $K = 0.66$.)

The growth of lateral deflections is illustrated in figure 5, where a lateral-deflection parameter Δ is plotted against a time parameter τ for several values of a straightness parameter S. The main thing to notice about this figure is that each curve has a vertical asymptote indicating that the lateral deflections approach infinity (resulting in collapse of the column) in some finite time. The asymptotic value of τ will be referred to as τ_{cr}.

The straightness parameter S is defined in terms of the flange stresses at the middle of the column immediately after the load is instantaneously applied and before any creep has occurred; that is,

20

$$S = e^{-\frac{B}{K}(\sigma_1 - \sigma_0)}$$

where σ_1 is the stress on the inside or concave side of the column and σ_0 is the stress on the outside or convex side of the column. These stresses are obtainable by means of an elastic calculation. If the column is perfectly straight, then σ_1 and σ_0 are equal. The straightness parameter S then reduces to unity and, as the graph shows, there are no lateral deflections with time for S = 1. All degrees of initial crookedness or straightness are included within the range S = 0 to S = 1.

The time parameter τ is proportional to the time in hours but also involves other quantities:

$$\tau = t\left(e^{\frac{B}{K}\sigma_1}\right)\left(\frac{ABE}{2K}\frac{\bar{\sigma}}{\sigma_e - \bar{\sigma}}\right)^{\frac{1}{K}}$$

The parameter is extremely sensitive to σ_1, which appears in the exponent of e, and therefore to the initial eccentricity and the closeness of the applied stress to the Euler stress. The difference between the applied stress $\bar{\sigma}$ and the Euler stress σ_e also appears explicitly in the denominator.

The ratio of the lateral deflection d to the width b between flange center lines is expressed as the sum of two terms: $\left(\frac{d}{b}\right)_{t=0}$, or the value existing immediately after the load is applied and obtainable by an elastic calculation, and $\left(\frac{d}{b}\right)_{CREEP}$, which is the time-dependent part. It is this latter term that is given by the parameter Δ through the equation $\left(\frac{d}{b}\right)_{CREEP} = \frac{K}{2B\bar{\sigma}}\Delta$.

If the lateral deflections themselves are not of interest, but only the service lifetime of the column is important, this information can be given in another plot that gives τ_{cr}, the lifetime parameter, in terms

of S, the straightness parameter. This curve is shown in figure 6.
The curve goes up to infinity asymptotically as the column approaches
straight.

The H-section column in itself is not of too great interest.
Nevertheless, analyses of the type described may be qualitatively
important in indicating the significant parameters that enter into a
problem. With the significant parameters known, the number of tests
required to obtain design information for structures not easily analyzed
can be greatly reduced. The results of a limited number of tests on
solid rectangular-section columns have been published in reference 1.
If, for the solid rectangular-section column, the flange stresses σ_i
and σ_0 are reinterpreted to be extreme fiber stresses, then the
results of reference 1 can be plotted in terms of the parameters τ_{cr}
and S, which were found to be significant for the H-section column.
The results are shown in figure 7. Some correlation is indicated, but
the number of tests is too few to conclude that these parameters are
indeed significant for the solid column. The dashed curve is taken
from the previous figure and replotted to the present scale. The trend
of four of the tests agrees with that of the dashed curve. (The solid
bar through one of the test points indicates permissible leeway in
plotting this point because of an uncertainty in the initial crookedness
of the column.) The test points for the solid column fall above the
theoretical curve for the H-section column, as is to be expected. The
two test points on the left-hand side of the graph which definitely do
not follow the trend of the other test points represent tests in which
the applied load was very close to the Euler buckling load. The
applied stress in these two cases was the same and was 96 percent of the
Euler buckling stress as contrasted with a maximum of 84 percent for the
other tests. Since the behavior of the column is very sensitive to the
closeness of the applied load to the Euler buckling load, a small error
in the calculated Euler buckling load could cause considerable scatter.
Furthermore, the extreme-fiber stress σ_i on the concave side of the
column, as computed by an elastic analysis, turned out to be above the
proportional limit for these two cases. The finite length of time it
takes to load the column would then be significant, and the present
analysis which assumes elastic behavior during instantaneous loading
would not apply. Some indication of the large experimental scatter to
be expected in creep-buckling tests is afforded by the fact that these
two test columns were identical except that one was more crooked than
the other, yet the more crooked column lasted longer than the straighter
one.

The column problem just described is one of the simplest problems
one can formulate involving buckling and creep. Further experimental
and theoretical work is needed; tests of plates as well as additional
tests of columns are contemplated.

REFERENCES

1. Jackson, L. R., Schwope, A. D., and Shober, F. R.: Summary Report on Information on the Plastic Properties of Aircraft Materials and Plastic Stability of Aircraft Structures at High Temperatures to the RAND Corporation. Battelle Memorial Inst., Dec. 15, 1949.

2. Heimerl, George J.: Determination of Plate Compressive Strengths. NACA TN 1480, 1947.

3. Stowell, Elbridge Z.: A Unified Theory of Plastic Buckling of Columns and Plates. NACA Rep. 898, 1948. (Formerly NACA TN 1556.)

4. Heimerl, George J., and Roberts, William M.: Determination of Plate Compressive Strengths at Elevated Temperatures. NACA Rep. 960, 1950. (Formerly NACA TN 1806.)

5. Shanley, F. R.: Analysis of Stress-Strain-Time Relations from the Engineering Viewpoint. Rep. No. P-68, The RAND Corp., March 4, 1949.
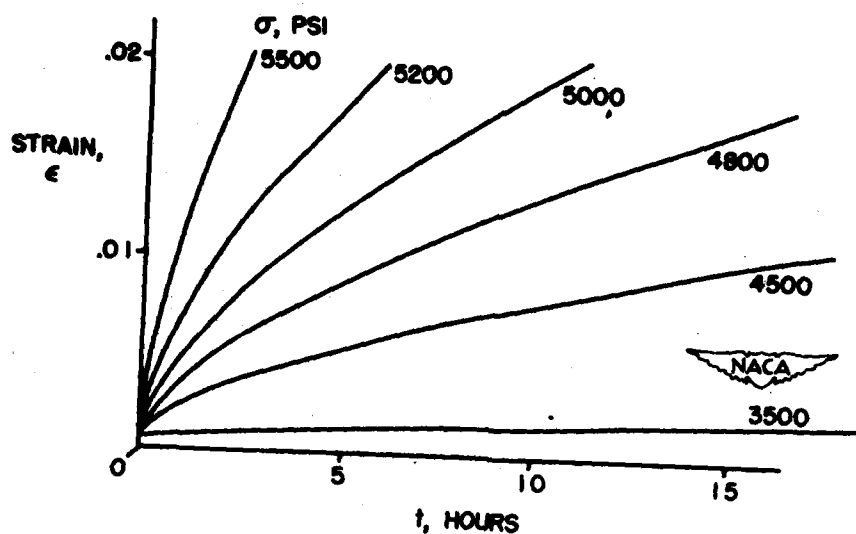
Figure 1.- Creep curves for 75S-T6 aluminum alloy at 600° F, based on an empirical formula suggested in reference 1. (Material stabilized at 600° F for 100 hours prior to test.)
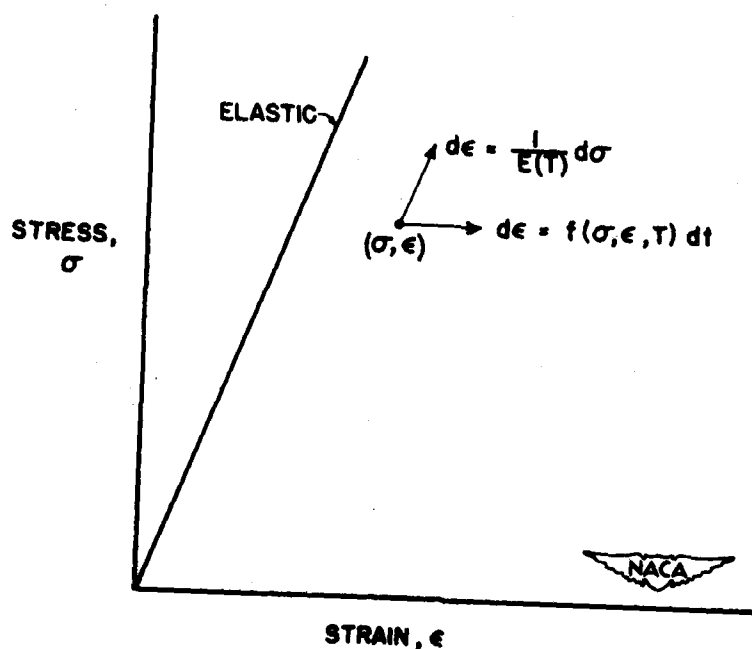
Figure 2.- Sketch illustrating basic assumptions of Shanley's creep theory for uniaxial stress at constant temperature. Inclined arrow represents an instantaneous stress change; horizontal arrow represents creep at constant stress.

$$d\epsilon = \frac{1}{E(T)} d\sigma + f(\sigma, \epsilon, T) dt$$

$$\frac{d\epsilon}{dt} = \frac{1}{E(T)} \frac{d\sigma}{dt} + f(\sigma, \epsilon, T)$$
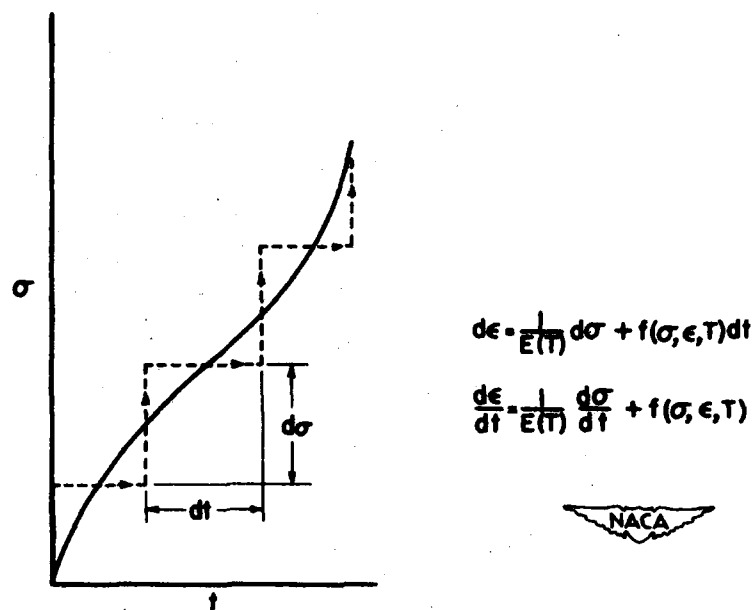
Figure 3.- Approximation of a smooth-curve loading history by step-type loading history.
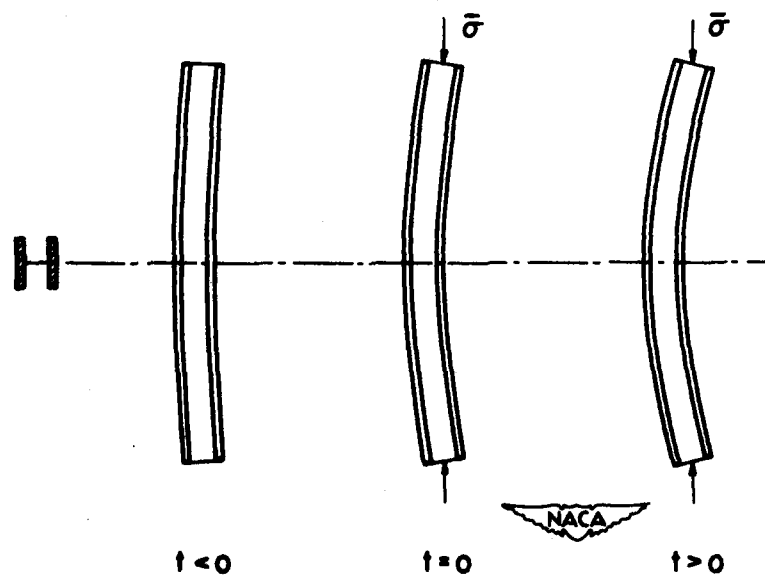
Figure 4.- Initially crooked column under constant load.

STRAIGHTNESS PARAMETER:

$$S = e^{-\frac{B}{K}(\sigma_i - \sigma_0)}$$

K = 0.66

TIME PARAMETER:

$$\tau = t\left(e^{\frac{B}{K}\sigma_i}\right)\left(\frac{ABE}{2K}\frac{\overline{\sigma}}{\sigma_e - \overline{\sigma}}\right)^{\frac{1}{K}}$$

LATERAL DEFLECTION:

$$\frac{d}{b} = \left(\frac{d}{b}\right)_{t=0} + \left(\frac{d}{b}\right)_{CREEP}$$

WHERE

$$\left(\frac{d}{b}\right)_{CREEP} = \frac{K}{2B\overline{\sigma}}\Delta$$

Figure 5.- Growth of lateral deflection of initially crooked
column under constant load.

Figure 6.- Chart showing variation of lifetime parameter τ_{cr} with
straightness parameter S for initially crooked column under
constant load.

Figure 7.- Comparison of H-section theory with solid-rectangular-section tests.

FATIGUE

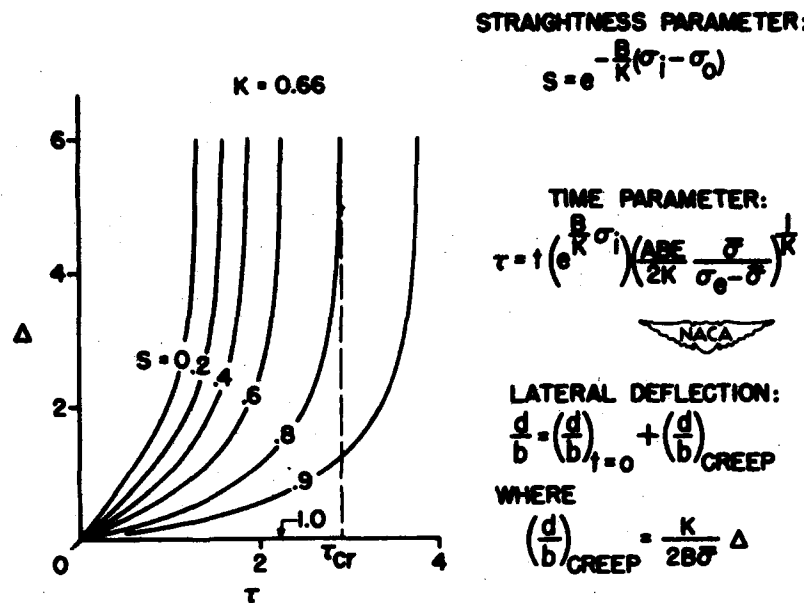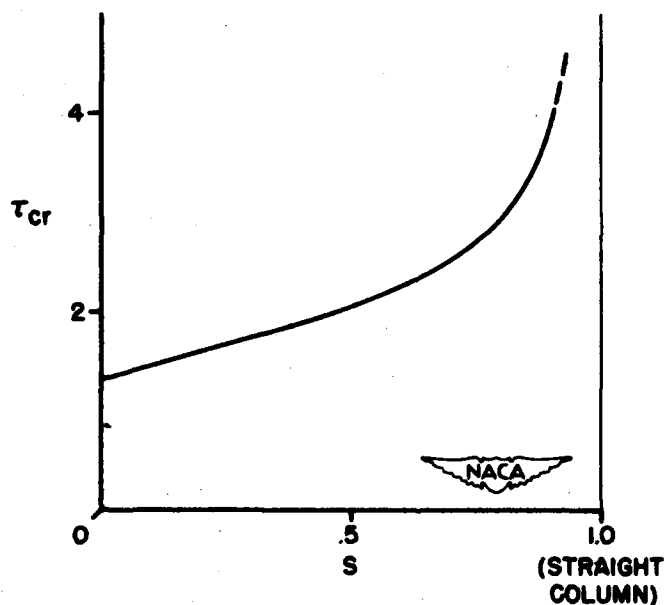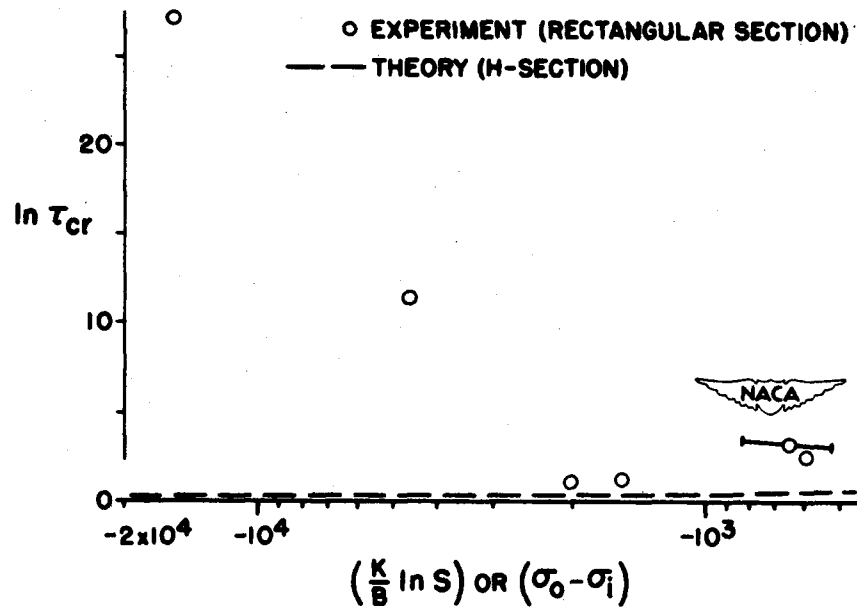## SIZE EFFECT IN NOTCH FATIGUE

By Paul Kuhn and Herbert F. Hardrath

Langley Aeronautical Laboratory

The present state of knowledge on fatigue is characterized by a practically complete lack of quantitative laws or rules; no one quantity can be calculated from any other quantity with reasonable accuracy. Reliable allowable stresses can therefore be established only by means of rather specific tests in which all the pertinent variables are varied over the desired range. Together with the scatter found in fatigue tests, this consideration requires such a vast amount of testing that it is impossible to fulfill all the demands for information. In this situation, any reasonably reliable rule that permits the elimination of one parameter from the test schedules will effect a large improvement.

One of the main parameters involved is the factor of stress concentration. For the sake of brevity, the word "factors" is used throughout rather than the words "stress concentration." For a given stress raiser, such as a notch, a theoretical factor can be obtained by the theory of elasticity or by photoelastic methods. Comparative fatigue tests on smooth and notched specimens give the actual or fatigue factor, which depends on the stress level or on the number of cycles to failure; in the special case when the specimen fails in one-quarter of a cycle - the ordinary tensile test, it is called the static factor. This paper is concerned with only the opposite limiting case, where many millions of cycles are required to produce failure, which implies that no plasticity effects are involved.

The analysis of many fatigue tests has shown that the fatigue factor lies somewhere between the static value and the theoretical one. Tests on geometrically similar specimens of differing sizes have shown that the fatigue factor increases with size, and it is more or less generally believed that it approaches the theoretical value as an upper limit. This effect of size might be called the geometric size effect, because it depends more on geometry than on the material. It should not be confused with what might be called the material size effect, the difference in properties, say, between a sheet 1/16 of an inch thick and a plate 4 inches thick, arising from the fact that the hot and cold work necessary to convert a 4-inch plate into a $\frac{1}{16}$-inch sheet improves the properties of the material (at least the static properties). This material-size effect can be eliminated from the fatigue tests.

The existence of the geometric size effect has been definitely recognized for about 20 years. The most plausible explanation afforded

is that the theory of elasticity breaks down when applied to small regions of certain materials such as structural metals. The theory is based on two assumptions: (a) the material is elastic and (b) it is homogeneous. Now, metals have a granular structure. Different grains may have different properties, and in an individual grain, the properties may be directional. The properties of large pieces of the material are determined by the statistical average of the individual properties. However, when the piece under consideration includes only a few grains, it is necessary to consider the individual properties. At this level, the assumption that the material is homogeneous is no longer tenable, and the usual theory of elasticity is no longer applicable.

A theoretical solution which takes into account simultaneously over-all geometry as well as the individual properties of the grains seems rather hopeless, and if it existed, it would undoubtedly be too complex for practical use. An interesting suggestion for a practical approximation, however, has been made by Neuber, who has done a large amount of work on the mathematical theory of notches. Neuber assumed (reference 1) that the specimen acts as though the material were made up of blocks, or, say, building bricks, which have the property that no stress gradient can develop across a face of the block. By applying this concept to the critical region at the bottom of a notch, Neuber arrived at the general formula for correcting the stress concentration given by the classical theory for size effect

$$K_N = 1 + \frac{K_T - 1}{1 + \frac{\pi - \omega}{\pi}\sqrt{\frac{R'}{R}}}$$

In this formula, K_N (with the subscript N for Neuber) denotes the corrected factor; K_T, the theoretical factor; ω, the flank angle of the notch; R, the radius of the notch; and R', the dimension of the Neuber "building block," which is dependent to some extent on the material. If R' approaches zero, the Neuber factor becomes equal to the theoretical factor. If R' becomes very large, the Neuber factor becomes equal to unity; that is, the notch has no stress-concentration effect. In terms of the widely used concept of "notch sensitivity," a small value of R' denotes large notch sensitivity and a large value of R' denotes small notch sensitivity. However, the formula brings out the fact that notch sensitivity is not a pure material property, but depends on size.

In order to assess the applicability of the Neuber formula to the fatigue problem, a collection was started of all notch-fatigue tests

that could be found in the literature; particular attention was paid to tests in which some size factor was varied systematically. The collection to date includes references 2 to 15. As a first approximation, R' was assumed to have the constant value 0.02 inch, which was calculated by Neuber from two sets of static strain measurements on steel specimens. The use of a constant value of R' is obviously only a crude first approximation; nevertheless the results were encouraging. For the majority of the tests, the use of the Neuber correction improved the prediction of the fatigue factor.

A study of the data obtained with the first approximation suggested that, for steel specimens, the value of R' might be taken to be a function of the tensile strength of the material. The tentative curve is shown in figure 1. As the strength of the steel increases, R' decreases - that is, the notch sensitivity increases. Judging by the data available now, this tentative curve appears to be reasonably reliable for ultimate strengths above 100 ksi; for lower strengths, it appears to be less reliable.

The next two figures show some sample comparisons, chosen at random, between calculated Neuber factors and experimental fatigue factors for sets of tests where some systematic variation of size was made. Figure 2 shows tests on rotating beams with semicircular grooves. The materials were S.A.E. 2345 and S.A.E. 1020 steel as noted. In the two sets of tests shown at the top, the ratio of notch radius to specimen diameter was constant; the theoretical factor, shown by the solid line, is therefore constant. The Neuber factor is shown as a dashed line. The difference between the solid-line curve and the dashed curve constitutes the predicted size effect. The circles denote experimental fatigue factors, obtained in the usual manner from the S-N curves for smooth and notched specimens. In the two tests shown at the bottom, the notch radius was constant; the theoretical factor therefore varied. The agreement between predicted and observed size effect is very good for all cases.

Figure 3 shows tests on filleted shafts. The agreement is very good for one set of tests on mild carbon steel (lower right) and for the nickel-molybdenum steel. For the other tests on mild carbon steel (upper left), the agreement is not so good. However, the largest discrepancy is about $12\frac{1}{2}$ percent, which is of the same order as the uncertainty of the experimental fatigue factor caused by uncertainty of the S-N curves on which the experimental factor is based.

From calculations and test data such as shown in figures 2 and 3, and from other notch-fatigue tests where no size variations were made, three summary plots have been prepared. Figure 4 summarizes all tests

available on rotating beams with grooves and V-notches. The ratio of
Neuber factor to fatigue factor is plotted against notch radius.
Because the number of points is rather large, some groups have been
averaged. The average is shown by a circle, the number above the circle
is the number of points averaged, and tick marks indicate the highest
and the lowest points in the group.

The plot shows that the Neuber factor agrees with the fatigue
factor to an accuracy of ±10 percent for the large majority of the
tests. Outside of one wild point, serious discrepancies appear only
for radii less than 0.01 inch. All the low points at this radius are
tests run by one investigator in one investigation, which leaves room
for the suspicion that there was some systematic flaw in the test
technique.

Figure 5 is the same type of summary plot for filleted shafts.
Again, most of the points fall within the ±10-percent band. There are
no low, or unconservative, points on this plot.

Figure 6 is the summary of the axial-load tests. The three types
of specimens shown at the top are the ones tested at the Battelle
Memorial Institute for the NACA; their material is S.A.E. 4130 steel.
The radii on these specimens are varied to obtain different theoretical
factors. The points fall within a ±5-percent band. The lower specimen
is cylindrical with a V-notch. The tests of these cylindrical specimens
(reference 5) were run on a number of alloy steels with various heat
treatments. Half of the tests were run at room temperature and half,
at -78° F; but there was no significant difference due to temperature.
The width of the scatter band for these tests is considerably larger
than for the other tests, but this is again a case of a notch radius
less than 0.01 inch, for which the scatter was larger on the rotating
beam tests, also.

Figures 4, 5, and 6 may be summarized as follows: The Neuber for-
mula, used in conjunction with the tentative curve of R' plotted
against tensile strength, predicts the fatigue factor from the theo-
retical factor to an accuracy of ±10 percent for 91 percent of the tests
if test specimens with radii less than 0.01 inch are excluded and for
66 percent if no test specimens are excluded. The tests include a large
variety of steels, with tensile strengths varying from 60 to 225 ksi,
very different configurations, and bending tests as well as axial loading
tests.

An extreme form of a notch is a crack. For this discussion, a
crack may be defined as a notch of known depth and very small but
unknown width. From this definition, it follows that a stress-
concentration factor cannot be calculated by the theory of elasticity,
because this theory requires that the geometry of the notch be com-
pletely defined. With the Neuber concept, on the other hand, the crack

is the limiting case of a notch, and the factor can be calculated readily from the depth of the crack alone.

Five sets of tests on specimens with artificial cracks were available. R. E. Peterson produced cracks of two different depths by machining a narrow groove and then compressing the specimens until the gap was closed (reference 13). In German tests (reference 16), specimens made of three nitrided steels were stretched until they cracked. As might be expected for this type of specimens, the agreement between calculated and experimental fatigue factors is not so good as for the other tests shown. The discrepancies were of the order of ±25 percent, with a maximum discrepancy of 50 percent. For the German tests, a photomicrograph made it possible to estimate the width of the crack; with this information, the theory of elasticity can be used to make an order-of-magnitude estimate of the theoretical factor. The error was over 1000 percent; the Neuber factor was therefore definitely a better approximation.

The Neuber block concept is a mathematical device for expressing the physical idea that nature imposes limitations on stress gradients, at least in materials with a granular structure. Now, stress gradients exist not only around notches; a beam also has a gradient across its depth. This suggests that the Neuber concept might be applied in some way to estimate the size effect on smooth rotating beams.

It has long been known that the fatigue strength decreases as the diameter of the rotating beam increases. H. F. Moore, for instance, ran a series of tests on six steels, with specimen diameter varied from 1/8 inch to about 2 inches, and found that the smallest specimens were up to 30 percent stronger than the largest ones (reference 8). The lower limit of strength, which might be called the true strength of the material, in a way, would be shown by specimens with infinite diameter or zero gradient. It is not possible to test a rotating beam of infinite diameter, but it is relatively easy to do the equivalent - to test specimens under axial loading. This was done in some recent German tests (reference 17) on two kinds of steel; the rotating beam specimens in these tests were very small in order to give large gradients. They varied from about 0.3 inch down to 0.040 inch in diameter. The smallest beam specimens had 36 percent and 65 percent more strength than the axially loaded specimens.

The theoretical method of applying the Neuber concept to tests of this type is not clear at the moment. Empirically, it was found that the strength of the rotating beams could be estimated quite well by multiplying the axial strength by the factor

$$1 + \sqrt{\frac{R'}{R}}$$

where R is now the radius of the specimen. The strengths predicted
in this manner agreed with the observed ones with a maximum error of
about 6 or 7 percent for all the tests mentioned except one of Moore's
tests, which showed a 20-percent discrepancy. (For the tests made by
Moore, the strength under axial loading was estimated by applying the
formula to the rotating-beam strengths obtained for specimens of varying
diameters. In effect, then, the formula checked the effect of varying
the diameter in the test range, but not the relation of rotating-beam
strength to axial strength.)

For steel, then, there seems to be good hope that the geometrical
size effect may be fairly well predictable. Additional work remains to
be done, of course, to clear up the existing discrepancies if possible,
to extend the method to other cases, and to define its limitations.

On aluminum alloys, little can be said at present. There are very
few systematic investigations of size effect, and the results from other
tests are very conflicting. A first approximation using R' equal to
0.02 inch as for steel gives good agreement for sets of tests of some
alloys, but even this first approximation does not look as promising
generally as it did for steel, and attempts at a second approximation
have been unsuccessful so far. It is suspected that the trouble is
caused by machining effects. This suspicion, voiced by various inves-
tigators, is supported by British X-ray measurements (reference 18) of
surface stresses caused by machining of cast aluminum alloys, which
suggest that the form tools used to produce V-notches may produce very
high residual stresses.

REFERENCES

1. Neuber, H.: Kerbspannungslehre. Grundlagen für genaue Spannung-srechnung. J. W. Edwards (Ann Arbor, Mich.), 1944. (Also available as translation "Theory of Notch Stresses. Principles for Exact Stress Calculation" from J. W. Edwards (Ann Arbor, Mich.), 1946.)

2. Dolan, T. J., and Hanley, B. C.: The Effect of Size and Notch Sensitivity on Fatigue Characteristics of Two Metallic Materials. Part II - S.A.E. 4340 Steel. Tech. Rep. No. 5726, ATI No. 5726, Air Materiel Command, U. S. Air Force, Oct. 5, 1948.

3. Dolan, T. J., and Yen, C. S.: Some Aspects of the Effect of Metallurgical Structure on Fatigue Strength and Notch-Sensitivity of Steel. Fifth Progress Rep., Univ. Ill. (Office Naval Res. Contract N6-ori-71), March 1948.

4. Grover, H. J., Bishop, S. M., and Jackson, L. R.: The Fatigue Strengths of Aircraft Materials. III. Axial-Load Fatigue Tests on Sheet Specimens (of 24S-T, of 75S-T, and of SAE 4130), with Notches Having K_t = 5.0. Battelle Memorial Inst. Rep. to NACA, Nov. 30, 1950.

5. Hempel, M.: Low Temperature Fatigue Test on Steel. Translation No. F-TS-1855-RE, ATI No. 18475, Air Materiel Command, U. S. Air Force, July 1948.

6. Jackson, L. R., Grover, H. J., and Leeser, D. O.: Special Investigation of the Fatigue Properties of Aircraft Materials. No. 4. Notch Fatigue Tests at Stress-Concentration Factor of 2.00. Battelle Memorial Inst. Rep. to NACA, June 1, 1949.

7. Jackson, L. R., Grover, H. J., and Leeser, D. O.: Special Investigation of the Fatigue Properties of Aircraft Materials. No. 5. Notch Fatigue Tests at Stress-Concentration Factor of 4.00. Battelle Memorial Inst. Rep. to NACA, Feb. 5, 1950.

8. Moore, H. F.: A Study of Size Effect and Notch Sensitivity in Fatigue Tests of Steel. Proc. A.S.T.M., vol. 45, 1945, pp. 507-531.

9. Moore, H. F.: The Effect of Size and Notch Sensitivity on Fatigue Characteristics of Two Metallic Materials. Part I - Aluminum Alloy 75S-T. Tech. Rep. No. 5726, ATI No. 5726, Air Materiel Command, U. S. Air Force, Oct. 5, 1948.

10. Moore, H. F., and Jordan, R. L.: Stress Concentration in Steel Shafts with Semicircular Notches. Proc. Fifth Int. Cong. Appl. Mech. (Cambridge, Mass., 1938), John Wiley & Sons, Inc., 1939, pp. 188-192.

11. Moore, H. F., and Morkovin, D.: Second Progress Report on the Effect of Size of Specimen on Fatigue Strength of Three Types of Steel. Proc. A.S.T.M., vol. 43, 1943, pp. 109-124.

12. Morkovin, D., and Moore, H. F.: Third Progress Report on the Effect of Size of Specimen on Fatigue Strength of Three Types of Steel. Proc. A.S.T.M., vol. 44, 1944, pp. 137-158.

13. Peterson, R. E.: Model Testing As Applied to Strength of Materials. Jour. Appl. Mech., vol. 1, no. 2, April - June 1933, pp. 79-85.

14. Peterson, R. E.: Stress-Concentration Phenomena in Fatigue of Metals. Jour. Appl. Mech., vol. 1, no. 4, Oct. - Dec. 1933, pp. 157-171.

15. Peterson, R. E., and Wahl, A. M.: Two- and Three-Dimensional Cases of Stress Concentration, and Comparison with Fatigue Tests. Jour. Appl. Mech., vol. 3, no. 1, March 1936, pp. A-15 - A-22.

16. Mailänder, R.: Ergebnisse von Dauerversuchen an Stählen. Bericht 116 der Lilienthal-Gesellschaft für Luftfahrtforschung, June 1939, pp. 18-24.

17. Siebel, Erich, and Pfender, Max: Weiterentwicklung der Festigkeitsrechnung bei Wechselbeanspruchung. Stahl und Eise, Sept. 11, 1947, pp. 318-321.

18. Frommer, Leopold, and Lloyd, E. H.: The Measurement of Residual Stresses in Metals by the X-Ray Back-Reflection Method, with Special Reference to Industrial Components in Aluminium Alloys. Jour. Inst. Metals, vol. LXX, 1944, pp. 91-124.
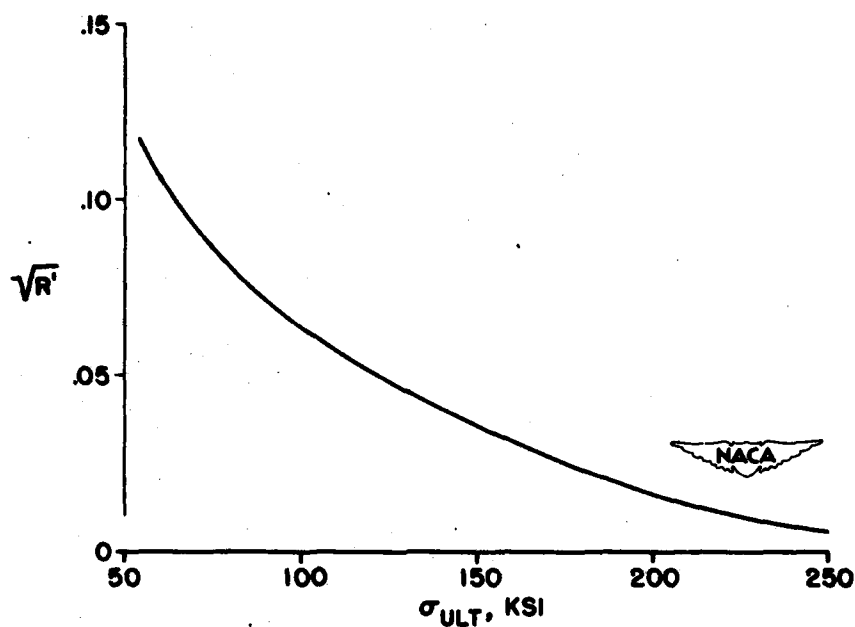
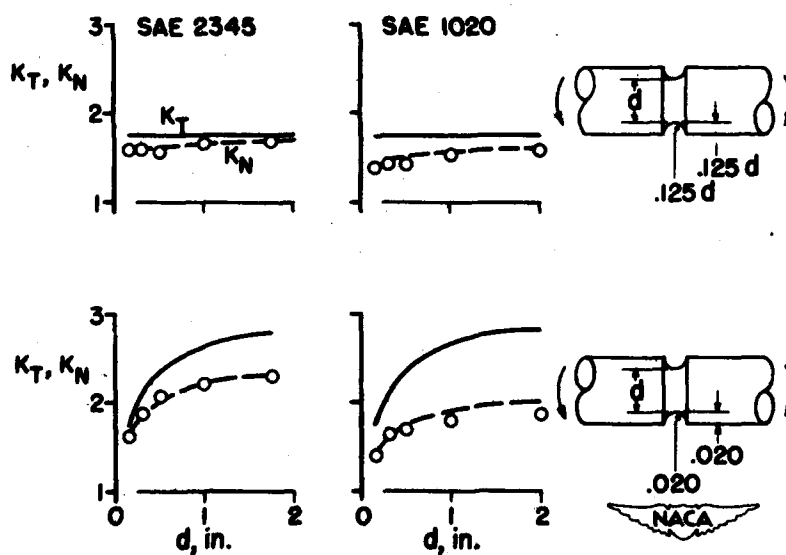Figure 1.- Relation between Neuber constant R' and tensile strength for steel specimens.

Figure 2.- Comparisons between calculated and experimental fatigue factors for rotating beams with grooves.
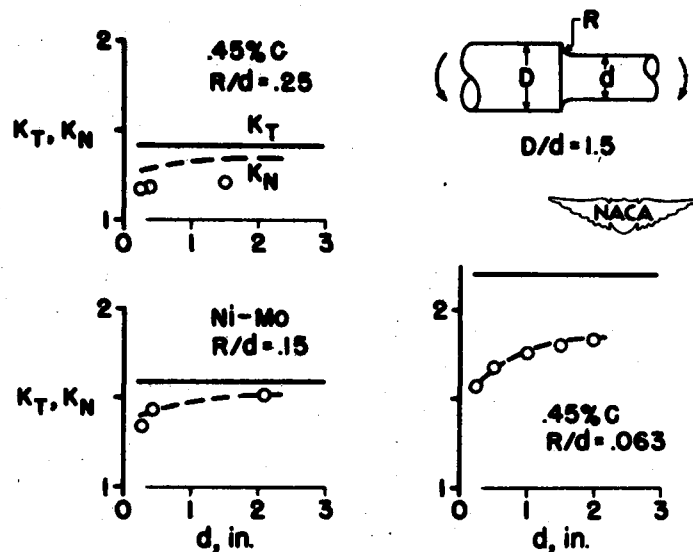
Figure 3.- Comparison between calculated and experimental
fatigue factors for filleted shafts (rotating beam tests).
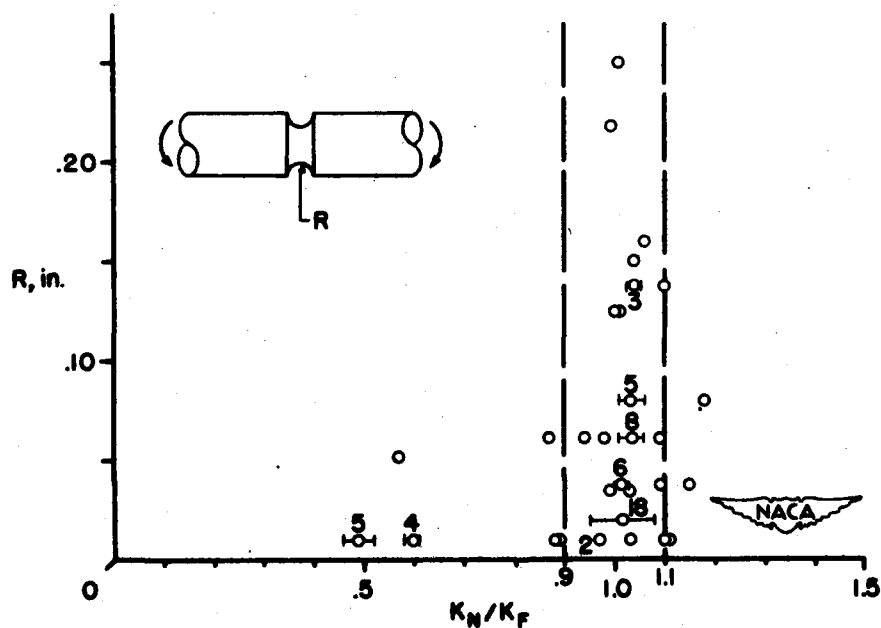

Figure 4.- Correlation between calculated and experimental
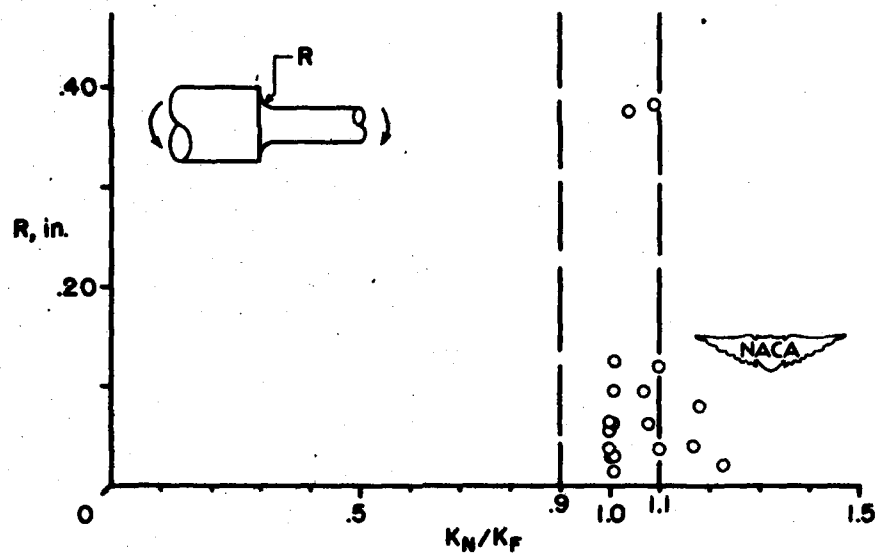fatigue factors for rotating beams with grooves and
V-notches.

Figure 5.- Correlation between calculated and experimental
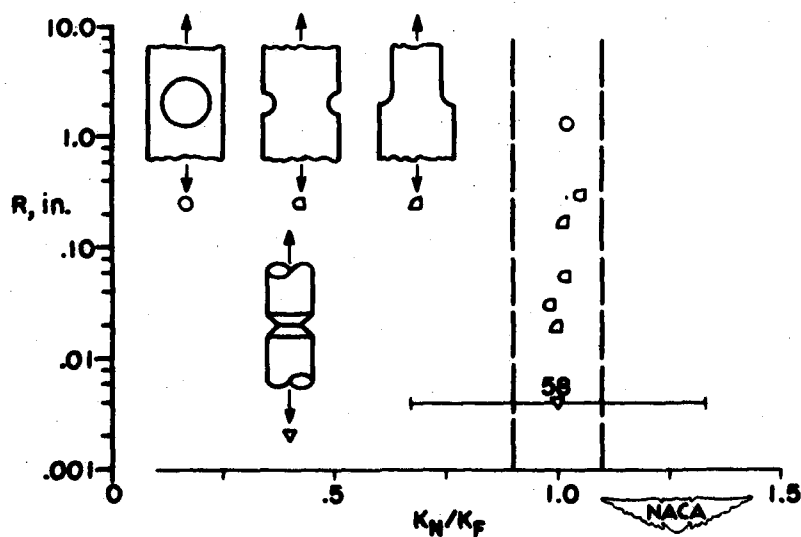fatigue factors for filleted shafts.

Figure 6.- Correlation between calculated and experimental
fatigue factors for axially loaded specimens.

INVESTIGATION OF FATIGUE STRENGTH OF A

FULL-SCALE AIRPLANE

By Dwight O. Fearnow

Langley Aeronautical Laboratory

Recent trends in airplane design, construction, and use have placed increasing emphasis upon the problem of fatigue in airplane structures. Unfortunately, an exact theoretical method of computing fatigue life is not available. Moreover, most fatigue tests to date have been conducted on small polished specimens under closely controlled laboratory conditions, but, although such basic tests are essential to the solution of the problem, they do not reproduce all the practical problems of a complex wing structure.

When it became apparent that war surplus airplanes could be made available for research on full-scale test specimens, the NACA Special Committee on Surplus Aircraft Research endorsed the proposal that an investigation of static and fatigue strength of new airplane wing structures, as well as those exposed to long war service, be carried out through the testing of surplus aircraft. The scope of the program was originally quite large. It covered the testing of some 600 airplanes of 15 different types and was to be carried out through the coordinated efforts of the Air Forces, Navy, aircraft industry, and NACA. It soon became apparent, however, that funds and personnel would not be available for such an ambitious program. The steering committee then recommended that the NACA carry out the initial phase of the program on one type of transport airplane. The NACA proceeded to secure 23 of the most suitable planes available from the War Assets Administration.

The original objectives of the program had to be modified to be consistent with the drastic reduction in the number of airplanes to be tested. Perhaps the most important objective of the modified program would be the determination of some correlation between the results of laboratory tests on small specimens and their application to the full-scale wing structure. Other objectives would be the determination of the spread in fatigue life in wing structures which are as nearly identical as assembly-line production methods will allow, the reduction in static strength after fatigue failure, the effect of fatigue damage on such parameters as natural frequency and damping characteristics, and, if possible, the loss in fatigue life associated with the number of hours a transport airplane has flown.

The results to be presented here are the first available from this investigation and deal entirely with tests of the constant-level type.

Subsequent tests should yield information from additional constant-level
tests as well as tests in which the stress level is varied in a random
step fashion.

The present investigation is being conducted on the wing structure
of the Curtiss-Wright C-46D transport airplane. The two test specimens
from which data have been obtained were subjected to about 600 hours of
flight and several years storage in an open depot. A test specimen
consists of a left- and a right-wing outer panel and a center section.
The outer panels are of the two-spar type of construction while the
center section has three spars. The spars are made of 24S-T aluminum
alloy but all skin and stiffeners are made from Alclad 24S-T.

Certain modifications are made to each airplane to prepare it for
testing. The fuselage is cut in front of and behind the wing, and this
section is then inverted and supported between structural steel back-
stops. The upper portion of figure 1 shows a profile view of half the
test specimen in its inverted position. The complete fuselage and back-
stops are omitted for clarity. The test specimen is symmetrical about
the center line. The outer wing panels are cut off at a station
405 inches from the center line of the wing-fuselage combination. This
reduced the total span by about 35 percent. Concentrated masses are
attached to the wing at the point where it was cut off to reproduce
level-flight stresses at station 214. Station 214 was designated as
critical for the fatigue tests because previous tests, utilizing brittle
lacquer, indicated numerous points of local high-stress concentrations
at that station. Design margins of safety were also very low in that
region of the wing. (See reference 1.) Actually, design bending moments
were reproduced fairly closely over a considerable portion of the wing
as can also be seen in the lower portion of figure 1, where bending
moment is plotted against wing semispan station in inches from the center
line. The upper dashed curve shows that, if relieving loads, resulting
from nacelle inertia effects, were not introduced during the laboratory
tests, design bending moments (the solid line, as obtained from refer-
ence 2) would be reproduced within about 1 percent over a considerable
portion of the test specimen. Since it appeared desirable to force the
wing to fail, if possible, at station 214, nacelle inertia effects were
introduced by means of a spring system at the engine mount, and, as
shown by the lower dashed line, the bending moments were reduced by
about 10 percent at the center line.

All tests were conducted by the resonant-frequency method. The
concentrated masses attached to the test specimen provided the mean
stress condition about which the wing vibrated. The fatigue machine now
being used for the constant-level tests is relatively simple. Basically,
it is an adjustable eccentric which transmits vertical force through a
push rod and a spring to the wing. The spring is necessary to permit

the required phase shift between wing and forcing function so that the wing resonance characteristics can be utilized.

Figure 2 shows a plan view of a portion of the right semispan of the test specimen. In this figure the fatigue cracks are denoted by arrows drawn to the points where the cracks started. The cracks are omitted for reasons of clarity. The straight and wavy dashed lines indicate points where fatigue-crack-detector wires were installed, and the squares indicate the nominal locations of the strain gages.

Although this figure shows only the right semispan, the points of origin of all eleven fatigue cracks, from both the left and right semispans of the first two specimens, are included. For purposes of identification, the cracks are numbered consecutively in order of occurrence. The first five cracks occurred in the first test specimen, whereas the last six occurred in the second test specimen. The R and L beside each crack number indicates the semispan, right or left, on which the crack occurred. In three instances, involving seven of the eleven cracks, duplicate failures were obtained. Cracks 2R, 1L, and 11L occurred in riveted joints which were symmetrical about the center line. Cracks 6R and 7L originated at identical points on the right and left semispans at the outboard juncture of the wing and nacelle group, while cracks 8R and 9L originated at the corners of identical inspection cut-outs. Cracks 3R and 5L occurred at the corners of inspection cut-outs in the outer panels, whereas cracks 4L and 10L originated in the joggle in doubler plates located on the outboard and inboard sides of the wing attachment angle.

The strain gages, shown by the squares, were located so as to measure only nominal stress in the material in the vicinity of the points where fatigue cracks originated and were far enough away from the point of fatigue-crack origin so as to measure no stress concentrations. The fatigue-crack-detector wires, the straight and wavy dashed lines, were located at points where the brittle-lacquer tests indicated spots of local high stresses.

Although it was intended to vibrate the test specimens about the 1 g or level-flight condition at a constant amplitude equivalent to an increment of load factor Δn of slightly more than ±0.6g, this could be achieved only to a limited degree. In the starting and stopping of the machine, a few cycles of load were applied at higher values of Δn as well as at lower values, but calculations have indicated that the effect of these loads was negligible.

Since the tests were not exact constant-level tests according to standards set forth in fatigue tests of small specimens, for purposes of analysis the assumption was made that only those cycles of load

applied in the interval between $\Delta n = 0.6g$ and $\Delta n = 0.75g$ had any
effect upon the fatigue life of the specimen. It was further assumed
that those loads acted at the midpoint of that interval. The effec-
tive stress-concentration factor K_1 was then computed by simply
dividing the stress from the S-N curve of unnotched Alclad 24S-T
aluminum-alloy sheet, as found in reference 3, by the measured stress.
The measured stress, as mentioned previously, included none of the
stress concentrations. The values obtained for K_1 are shown in the
following table:

Crack	Cycles	K_1	Maximum stress (psi)
1	170,000	3.2	40,500
2	194,000	2.6	39,800
3	194,000	4.2	41,700
4	203,000	---	------
5	280,000	---	------
6	171,000	---	------
7	171,000	---	------
8	171,000	---	------
9	171,000	---	------
10	274,000	---	------
11	308,000	3.0	37,000

For cracks 1, 2, and 11, all of which originated in similar riveted
joints, K_1 varies from 2.6 to 3.2. The corner of an inspection cut-
out, where crack 3 originated, had an effective stress-concentration
factor of 4.2. The table also shows the number of cycles of load
required to cause failure, as well as the maximum effective stress.
Maximum effective stress is defined as measured mean stress plus half
of the alternating stress all multiplied by the effective stress-
concentration factor. Although it may be mere coincidence, it is inter-
esting to note the relatively small amount of spread in the number of
cycles required to cause failure for each of the eleven cracks, even
though all cracks did not originate in the same places on the two test
specimens. The maximum spread is in the order of a factor of 2; the
lowest number is 170,000 and the maximum, 308,000. This could lead to
some speculation on the possibility of determining airplane S-N curves,
and a word of caution should be injected here concerning such specu-
lation. The relatively small amount of data available to date should
not be overlooked and subsequent data may show considerably more scatter.

Figure 3, in which loss of tension material in percent is plotted
against cycles, shows graphically how cracks 3 and 4 grew after

inception. The abscissa is shown on rectangular coordinates rather than a logarithmic scale to emphasize the fact that quite a number of cycles are required to cause appreciable loss of tension material. It is interesting to note in this figure that the rate of crack growth was quite small until between 5 and 10 percent of the tension material failed. From that point the rate of growth, as shown by the steepness of the curves, was quite rapid. It was interesting to watch the growth of the crack during the test. In each case the crack in the skin would pass over a stringer and proceed to about halfway to the next stringer and then the first stringer would fail, and so on across the wing in almost a straight line.

Figure 4 shows the reduction in natural frequency of the wing as a function of loss of tension material for cracks 3 and 4. The natural frequency of the test specimen, before the test started, was about 106 cycles per minute. After about 55 percent of the tension material had failed, this value had only been reduced by about 2 percent or to about 103.5 cycles per minute. No change in natural frequency was apparent until after the fatigue cracks had originated.

Although no specific damping measurements were taken during the test, the very nature of the test procedure, that is, the resonant-frequency method, was such that any change in damping should have resulted in a change in amplitude of vibration. No such change in amplitude was apparent until after a fatigue crack had originated.

In conclusion, a fatigue-strength investigation is currently being conducted on full-scale airplane-wing structures by the resonant-frequency method, wherein concentrated masses are attached to the wing to reproduce level-flight stresses over approximately 45 percent of the span. The results presented include the data gathered thus far on the first two fatigue specimens. Although the results cover eleven fatigue cracks, there are not yet sufficient data on which to base definite conclusions. The data do indicate a surprisingly small amount of spread in fatigue life even though all fatigue cracks did not originate at the same points. Computed effective stress-concentration factors for similar riveted joints varied from 2.6 to 3.2, whereas the one value computed for the corner of an inspection cut-out was 4.2. Neither the natural frequency nor the damping of the two test specimens appeared to be affected by fatigue damage until after a fatigue crack had originated. The rate of fatigue-crack growth was quite small until approximately $7\frac{1}{2}$ percent of tension material was lost.

REFERENCES

1. Nilsen, R. T., and Bradley, R. T.: Wing Analysis (Section Properties
   and Stresses) Model 20-B (C-46). Volume I. Rep. No. 20-C10,
   Curtiss-Wright Corp., Airplane Div. (St. Louis), March 10, 1942.

2. Anon: General Analysis - Calculation of Applied External Wing Loads.
   Model 20-B (C-46). Rep. No. 20-A4, Curtiss-Wright Corp., Airplane
   Div. (St. Louis), March 6, 1942.

3. Russell, H. W., Jackson, L. R., Grover, H. J., and Beaver, W. W.:
   Fatigue Strength and Related Characteristics of Aircraft Joints.
   II - Fatigue Characteristics of Sheet and Riveted Joints of
   0.040-Inch 24S-T, 75S-T, and R303-T275 Aluminum Alloys. NACA
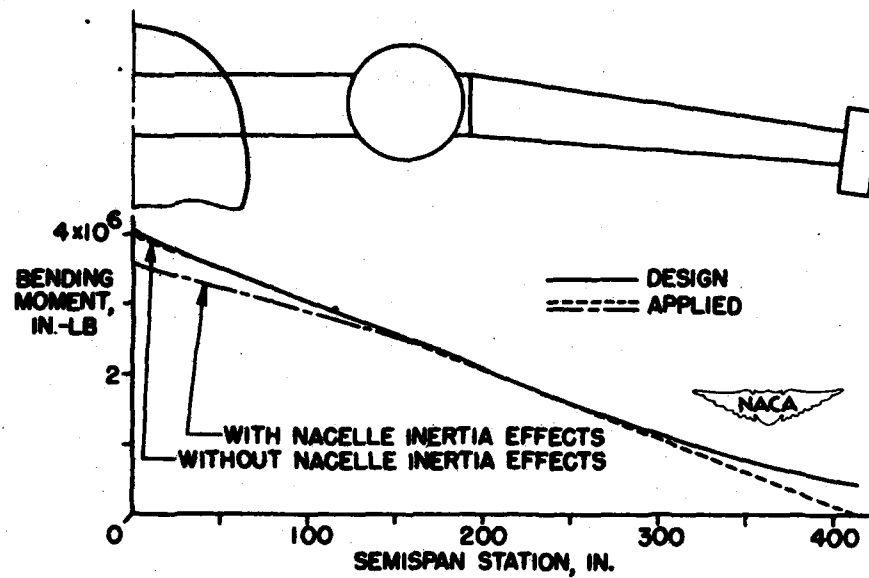   TN 1485, 1948.

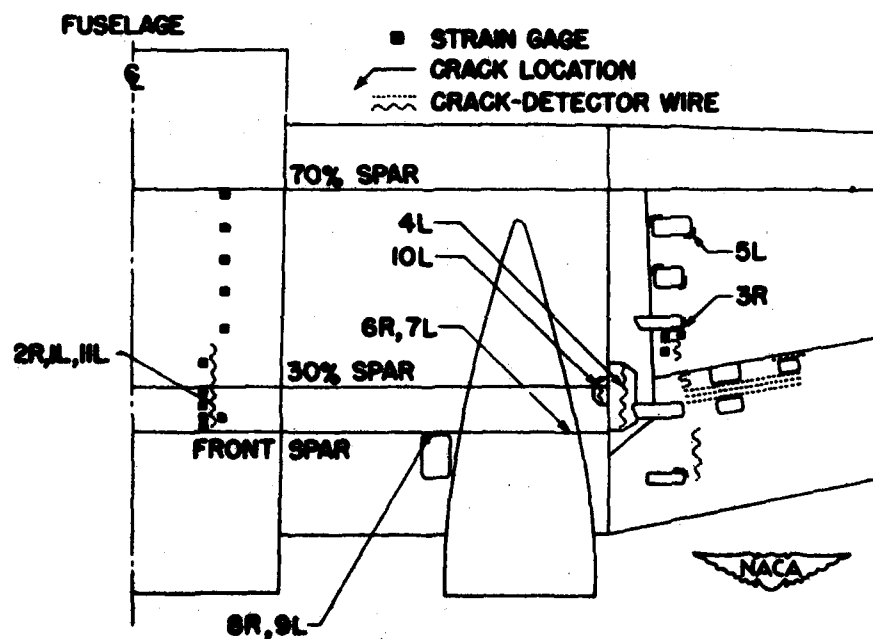Figure 1.- Comparison of design and test applied bending moments over span of test specimen.

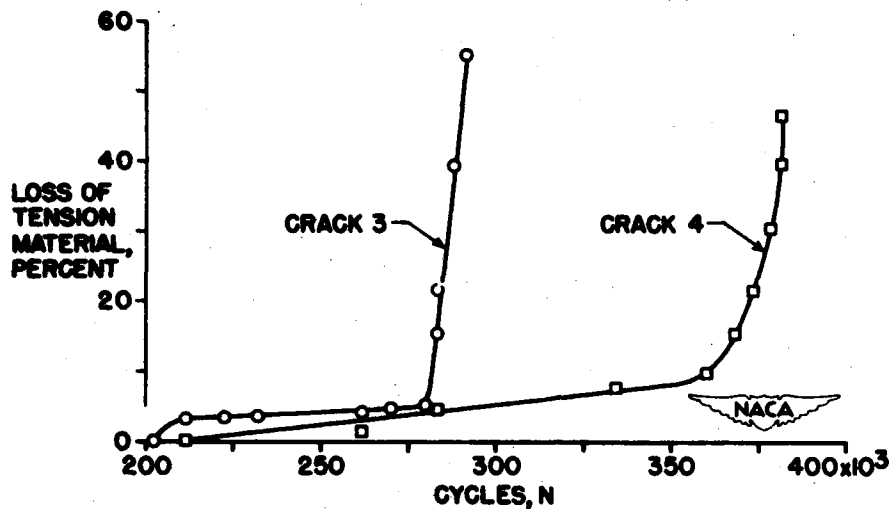Figure 2.- Nominal location of instrumentation and points of fatigue-crack origin.
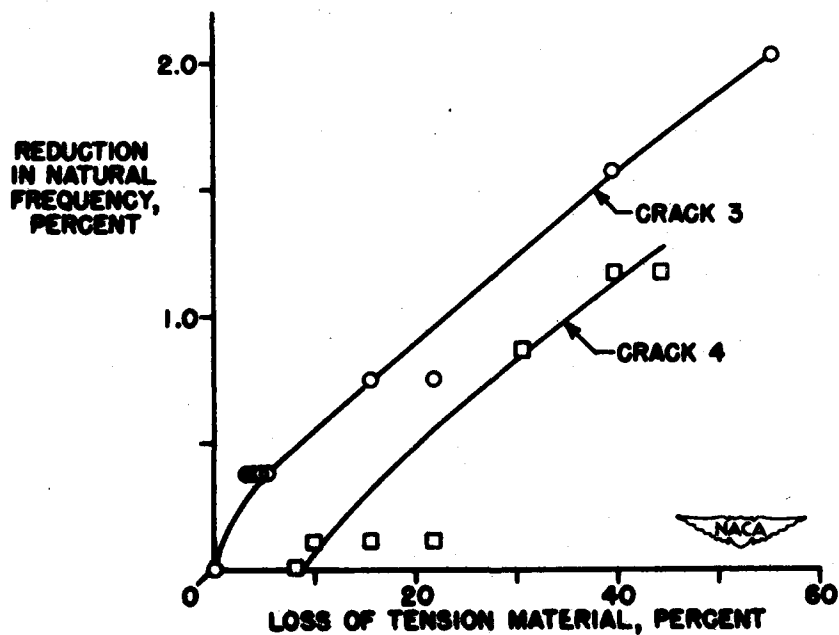
Figure 3.- Typical curves of fatigue-crack growth.

Figure 4.- Effect of fatigue-crack damage on natural frequency
of test specimens.